Faculty of Physics and Astronomy
University of Heidelberg

Effects on Strong Lensing in a TeVeS Universe

Diploma thesis
in Physics

Submitted by
Martin Feix
- born in Kirchheim, Germany -

2007

This diploma thesis has been carried out by
Martin Feix
at the
Institute of Theoretical Astrophysics
under the supervision of
Prof. Matthias Bartelmann

Effects on Strong Lensing in a TeVeS Universe

Abstract

Only recently, the Modified Newtonian Dynamics (MOND) paradigm has been provided with a fully relativistic framework, the so-called TeVeS theory (Bekenstein, 2004), which describes the effects of gravity without invoking any dark matter. In this work, we will study TeVeS gravity in the context of gravitational lensing (GL). Using the smooth free function proposed by Zhao et al. (2006), we derive analytical lens models and investigate the effect of moving lenses, which turns out to be same as in GR. After exploring the influence of the free function for spherical systems, we present a fast Fourier-based method allowing the treatment of nonspherical lenses in TeVeS. Applying this method to a set of matter density distributions including a toy model of the cluster merger $1E0657-558$, we show the failure of the thin lens approximation, conclude that the TeVeS convergence tracks the dominant baryonic components and confirm the basic result of Angus et al. (2007).

Erklärung:

Ich versichere, dass ich diese Arbeit selbständig verfasst und keine anderen als die angegebenen Quellen und Hilfsmittel benutzt habe.

Heidelberg, den _____ _____

Unterschrift

Contents

List of Figures

List of Tables

Introduction

As is known, both Newtonian gravity and General Relativity (GR) cannot explain the dynamics of our universe on a wide range of physical scales as the amount of visible mass clearly lies below what would be expected when measuring the corresponding gravitational field. Commonly, this is known as the *missing mass problem*. The usual way to overcome this crisis is actually very simple: One can postulate the existence of a form of matter which does not couple to light, therefore being referred to as dark matter. Over last years, this paradigm has been remarkably successful and research has flourished on many fields ranging from cosmology to theoretical particle physics. However, one can also take a different point of view. Instead of invoking any exotic form of matter, one may simply think of modifying the law of gravity itself. Although this may seem weird at first glance, the invocation of a mysterious matter particle is at least as unusual as a modification of gravity. It should be clear that any theory that has not been ruled out so far is worth investigating. As can be imagined, there is a huge variety of possible modifications to gravity. Here, we shall focus on Tensor-Vector-Scalar gravity (TeVeS) (Bekenstein, 2004), a fully relativistic theory of gravity, which recovers the properties of Modified Newtonian Dynamics (MOND) (Milgrom, 1983a,b,c). As dark matter has been introduced to resolve problems on larger scales which are usually related to the fields of cosmology and gravitational lensing, any proposed modified theory of gravity must be capable of giving a consistent explanation for the observed phenomena. Within this work, we shall study the effects of TeVeS in the framework of gravitational lensing (GL).

Starting with a brief introduction to MOND, we will establish the TeVeS theory in the first chapter where we will learn about its intrinsic properties, the role of the so-called free function and the MONDian limit, which is actually recovered in the quasistatic limit. Having acquired the necessary basics, we shall develop the lensing formalism in TeVeS. Using a certain form of the free function, which has been originally proposed by Zhao et al. (2006), we shall discuss analytical models of TeVeS lenses and investigate the behavior of lens systems with peculiar velocity $v \neq 0$, which is shown to be identical to the case of GR. After a detailed discussion of the free function at the beginning of chapter three, we will present a numerical tool that allows the treatment of nonspherical lenses in TeVeS. In contrast to already existent solvers like the ones of Ciotti et al. (2006) or Brada & Milgrom (1995, 1999), our method is fully numerical, fast and Fourier-based. After discussing some basic properties of this method, we shall apply it to a set of different baryonic matter distributions showing the failure of the thin lens approximation and concluding that the TeVeS convergence map shows a tracking of the dominant baryonic components. Finally, we will create a toy model of the cluster merger $1E0657-558$ and use our solver to obtain the corresponding lensing maps confirming the basic result found by Angus et al. (2007).

1 Bekenstein's TeVeS

This chapter will give an introduction to Bekenstein's Tensor-Vector-Scalar gravity (TeVeS) and its role as a generalized relativistic version of modified Newtonian dynamics (MOND). Beginning with a brief overview of MOND, we will turn to the TeVeS theory, which can be regarded as a modified version of General Relativity (GR), and derive the necessary equations. After a first approach to the so-called free functions we will move on to the nonrelativistic limit of TeVeS and its connection to classical MOND studying both the Newtonian and the MONDian regime. At the end of the chapter we shall give a detailed analysis of cosmology in the TeVeS framework, which is relevant when considering gravitational lensing.

1.1 Modified Newtonian Dynamics

Milgrom's modified Newtonian dynamics (MOND) paradigm (Milgrom, 1983a,b,c) has proven to be quite successful in describing much of extragalactic dynamics phenomenology without the need of dark matter (DM) although there have occurred some problems regarding the dynamics of galaxy clusters (Sanders, 1999). Compared to other suggested modifications of gravity, MONDian dynamics is characterized by an acceleration scale a_0, and its departure from classical Newtonian predictions depends on acceleration:

$$\tilde{\mu}\left(\frac{|\vec{a}|}{a_0}\right)\vec{a} = -\vec{\nabla}\Phi_N. \tag{1.1}$$

Here, Φ_N denotes the common Newtonian potential of the visible (baryonic) matter and the function $\tilde{\mu}$, controlling the modification of Newton's law, has the following asymptotic behavior:

$$\tilde{\mu}(x) \approx x \qquad x \ll 1, \tag{1.2}$$

$$\tilde{\mu}(x) \to 1 \qquad x \gg 1. \tag{1.3}$$

Analyzing observational data, Milgrom estimated $a_0 \approx 1 \times 10^{-8} cms^{-2}$. For example, using this value for a_0 and choosing

$$\tilde{\mu}(x) = \frac{x}{\sqrt{1+x^2}},$$

it is possible to fit the rotation curve of NGC 1560 as shown in Figure 1.1. Since accelerations in the solar system are strong compared to a_0, equation (1.1) will turn into the classical Newtonian law there.

1.1.1 The Tully-Fisher Law

Equation (1.1) has been constructed to agree with the fact that rotation curves of disk galaxies become flat outside their central parts. In such regions the Newtonian potential caused by a galaxy of mass M is approximately spherical and since $|\vec{\nabla}\Phi_N| \approx GMr^{-2} \ll a_0$, equation (1.2) is satisfied. If we introduce the centripetal acceleration v_c^2/r with a radius independent velocity v_c, we arrive at the expression

$$v_c = (GMa_0)^{\frac{1}{4}}. \tag{1.4}$$

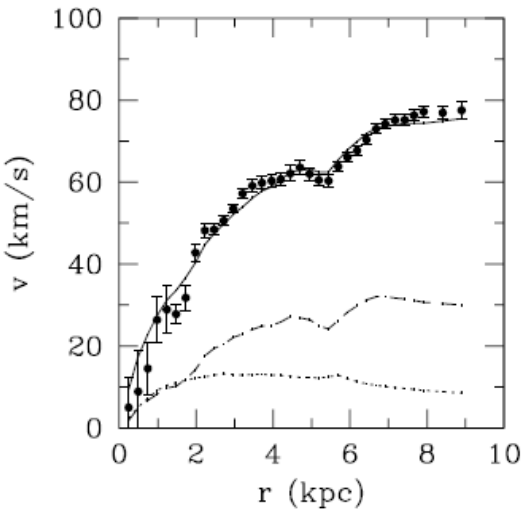

Figure 1.1: The points show the observed 21cm line rotation curves of a low surface brightness galaxy, NGC 1560 (Broeils, 1992). The dotted and dashed lines are the Newtonian rotation curves of the visible and gaseous components of the disk and the solid line is the MOND rotation curve with $a_0 = 1 \times 10^{-8} cms^{-2}$. The only free parameter is the mass-to-light ratio of the visible component.

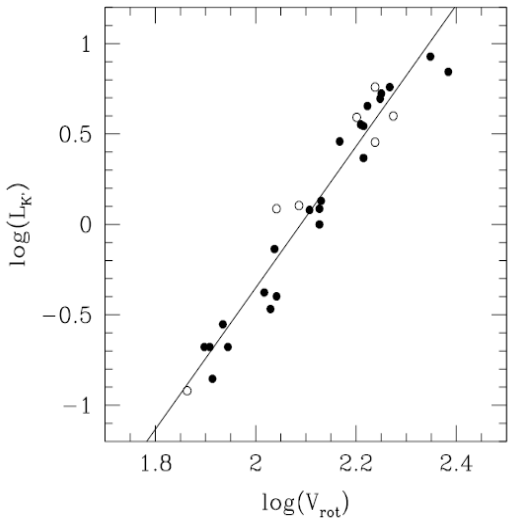

Figure 1.2: The near-infrared Tully-Fisher relation of Ursa Major spirals (Sanders & Verheijen, 1998). The rotation velocity is the asymptotically constant value in units of kms^{-1} and the luminosity is in $10^{10} L_{\odot}$. The unshaded points are galaxies with disturbed kinematics. The line is a least-square fit to the data and has a slope of 3.9 ± 0.2.

Assuming a constant mass to luminosity ratio in a specified spectral band, the luminosity in that band should scale as v_c^4. There is a law of just this form relating the near infrared (H-Band) luminosity L_H of a spiral disk galaxy to its rotation velocity

$$L_H \propto v_c^4 \tag{1.5}$$

with a constant proportionality factor within each galactic morphology class: the Tully-Fisher law (Tully & Fisher, 1977), which is shown for the Ursa Major spirals in Figure 1.2 (Sanders & Verheijen, 1998). In the view of MOND, this empirical law is a natural consequence as it is predicted by the dynamics in the low acceleration regime.

1.1.2 Problems

There is quite an amount of other MOND successes making equation (1.1) seem promising, but there is one crucial point which has been left out so far: it is not a theory. To be more specific, this kind of gravity modification violates the conservation of energy, momentum and angular momentum (Milgrom, 1983c). It is not a consistent scheme as it is unclear whether a gas particle of a star located in the outer part of a galaxy is subject to high or low acceleration. In addition to that, we are not able to develop a cosmological model and there is no way to specify gravitational light deflection using equation (1.1) alone. If we want to study gravitational lensing within a MONDian framework, we will need both a cosmological background and a theory of gravitational light deflection. Fortunately, we now have a full relativistic theory containing MONDian features: it is the Tensor-Vector-Scalar gravity (Bekenstein, 2004), which will be established in the following sections.

1.2 Fundamentals of TeVeS

In the following, we will introduce the main concepts of Bekenstein's TeVeS and its connection to the previously mentioned MOND paradigm. We will consistently use a metric signature of +2 and units with $c = 1$. If not specified in any other way, upper and lower indices as well as covariant derivatives refer to the Einstein metric $g_{\mu\nu}$. Greek indices run over four coordinates while Latin ones run over the spatial coordinates only.

1.2.1 Fields and Actions

In TeVeS, gravity is based on three dynamical fields: an Einstein metric $g_{\mu\nu}$ with a well defined inverse $g^{\mu\nu}$, a timelike 4-vector field U_μ such that

$$g^{\mu\nu}U_\mu U_\nu = -1 \tag{1.6}$$

and a scalar field ϕ; in addition, there is also a nondynamical scalar field σ. Another essential feature of TeVeS is the physical metric $\tilde{g}_{\mu\nu}$, which is needed for gravity-matter coupling only and obtained by stretching the Einstein metric in the spacetime directions orthogonal to $U^\mu = g^{\mu\nu}U_\nu$ by a factor of $e^{-2\phi}$ while shrinking it by the same size in the direction parallel to U^μ:

$$\tilde{g}_{\mu\nu} = e^{-2\phi}(g_{\mu\nu} + U_\mu U_\nu) - e^{2\phi}U_\mu U_\nu \tag{1.7}$$

$$= e^{-2\phi}g_{\mu\nu} - 2U_\mu U_\nu \sinh(2\phi). \tag{1.8}$$

Using $g^{\mu\nu}$ the inverse of the physical metric $\tilde{g}_{\mu\nu}$ is given by:

$$\tilde{g}^{\mu\nu} = e^{2\phi}g^{\mu\nu} + 2U^\mu U^\nu \sinh(2\phi). \tag{1.9}$$

The geometrical part of the action S_g is exactly the same as in GR:

$$S_g = \frac{1}{16\pi G}\int g^{\mu\nu}R_{\mu\nu}\sqrt{-g}d^4x, \tag{1.10}$$

where $R_{\mu\nu}$ is the Ricci tensor of $g_{\mu\nu}$ and g the determinant of metric $g_{\mu\nu}$. As we shall see, this chosen form of the action keeps TeVeS close to GR, i.e. TeVeS will recover well-known features of GR, albeit modified by the other fields.

The action S_s of the scalar fields σ and ϕ takes the form

$$S_s = -\frac{1}{2}\int\left[\sigma^2 h^{\mu\nu}\phi_{,\mu}\phi_{,\nu} + \frac{1}{2}Gl^{-2}\sigma^4 F(kG\sigma^2)\right]\sqrt{-g}d^4x, \tag{1.11}$$

where

$$h^{\mu\nu} = g^{\mu\nu} - U^\mu U^\nu \tag{1.12}$$

and F is a free dimensionless function. We also note that there are two constant positive parameters k and l. Because ϕ is dimensionless, σ^2 has the dimensions of G^{-1}. Therefore, k is a dimensionless constant while l is a constant length. Apparently, there is no kinetic term for the σ field. Thus, variation with respect to σ will lead to an algebraic expression between σ and the invariant $h^{\mu\nu}\phi_{,\mu}\phi_{,\nu}$ allowing σ to be substituted. The term $-\sigma^2 U^\mu U^\nu \phi_{,\mu}\phi_{,\nu}$ included in the scalar's action has been introduced by Bekenstein in order to eliminate superluminal propagation of the ϕ field. To get a better insight into the structure of (1.11), we introduce a new nondynamical field $\hat{\sigma} = \sqrt{8\pi G}\sigma$ and the quantity $V(\hat{\sigma}) = \hat{\sigma}^4 l^{-2}F(k\hat{\sigma}^2/8\pi)/16\pi$, which enables us to write the scalar action as

$$S_s = -\frac{1}{16\pi G}\int\left[\hat{\sigma}^2 h^{\mu\nu}\phi_{,\mu}\phi_{,\nu} + V(\hat{\sigma})\right]\sqrt{-g}d^4x.$$

Recalling that $\hat{\sigma}/\sqrt{8\pi G} = \sigma$ is actually related to $h^{\mu\nu}\phi_{,\mu}\phi_{,\nu}$, we can identify both a potential- and a kinetic-like term. From this point of view, the action's form now seems more familiar compared to other commonly used expressions like, for instance, that of an interacting scalar field whose Lagrangian is given by

$$\mathcal{L} = \frac{1}{2}g^{\mu\nu}\psi_{,\mu}\psi_{,\nu} + V(\psi).$$

Anyway, we shall keep to equation (1.11) for further investigation.

The action of the vector U_μ reads as follows:

$$\begin{aligned} S_v &= -\frac{K}{32\pi G}\int\left[g^{\alpha\beta}g^{\mu\nu}U_{[\alpha,\mu]}U_{[\beta,\nu]} - \frac{2\lambda}{K}(g^{\mu\nu}U_\mu U_\nu + 1)\right]\sqrt{-g}d^4x \\ &= -\frac{K}{32\pi G}\int\left[F^{\mu\nu}F_{\mu\nu} - \frac{2\lambda}{K}(g^{\mu\nu}U_\mu U_\nu + 1)\right]\sqrt{-g}d^4x, \end{aligned} \tag{1.13}$$

where $F_{\mu\nu} = U_{[\mu,\nu]}$. Here, indices surrounded by square brackets are antisymmetrized, e.g. $A_{[\mu}B_{\nu]} = A_\mu B_\nu - A_\nu B_\mu$, λ is a spacetime-dependent Lagrange multiplier enforcing the normalization of the vector field from equation (1.6) and since U_μ is dimensionless, K is a dimensionless constant. As we can clearly see, equation (1.13) looks similar to the classical Maxwell action. While the first term corresponds to $F^{\mu\nu}F_{\mu\nu}$ in electrodynamics, the second one stands for an effective mass of the field U_μ. In summary, TeVeS has two dimensionless constants k and K as well as two dimensional constants G and l.

According to the equivalence principle, we obtain the matter action by transcribing the flat spacetime Lagrangian $\mathcal{L}(\eta_{\mu\nu}, f^\alpha, f^\alpha_{|\mu}, \dots)$ for any field f^α as

$$S_m = \int \mathcal{L}(\tilde{g}_{\mu\nu}, f^\alpha, f^\alpha_{|\mu}, \dots)\sqrt{-\tilde{g}}d^4x, \tag{1.14}$$

where the covariant derivatives denoted by $|$ are taken with respect to $\tilde{g}_{\mu\nu}$. Matter fields are coupled to gravity by the physical metric $\tilde{g}_{\mu\nu}$, i.e. from the matter's point of view the universe has the metric $\tilde{g}_{\mu\nu}$. The relation between $\sqrt{-\tilde{g}}$ and $\sqrt{-g}$ is given by:

$$\sqrt{-\tilde{g}} = e^{-2\phi}\sqrt{-g}. \tag{1.15}$$

1.2.2 Basic Equations

As customary, we obtain the corresponding field equations by varying the total action $S = S_g + S_v + S_s + S_m$ with respect to the basic fields $g^{\mu\nu}, \phi, \sigma$ and U_μ. For this reason we need to know how $\tilde{g}_{\mu\nu}$, which appears in the matter's action, varies with the basic fields. Using equation (1.9) we get:

$$\begin{aligned} \delta\tilde{g}^{\alpha\beta} = {} & e^{2\phi}\delta g^{\alpha\beta} + 2\sinh(2\phi)U_\mu\delta g^{\mu(\alpha}U^{\beta)} \\ & + 2[e^{2\phi}g^{\alpha\beta} + 2U^\alpha U^\beta\cosh(2\phi)]\delta\phi \\ & + 2\sinh(2\phi)U^{(\alpha}g^{\beta)\mu}\delta U_\mu. \end{aligned} \tag{1.16}$$

Similar to equation (1.13), indices in parentheses are symmetrized, e.g. $A_{(\mu}B_{\nu)} = A_\mu B_\nu + A_\nu B_\mu$.

A. Equations for the metric

Let us begin with the metric field and vary S with respect to $g^{\alpha\beta}$. Since S_g is exactly the same as in GR, we find

$$\delta S_g = \frac{1}{16\pi G}G_{\alpha\beta}\sqrt{-g}\delta g^{\alpha\beta}, \tag{1.17}$$

where $G_{\alpha\beta} = R_{\alpha\beta} - \frac{1}{2}g_{\alpha\beta}R$ is the the Einstein tensor of $g_{\alpha\beta}$. The contribution of the matter's action can be written as

$$\delta S_m = -\frac{1}{2}\tilde{T}_{\alpha\beta}\sqrt{-\tilde{g}}\delta\tilde{g}^{\alpha\beta} + \dots \quad . \tag{1.18}$$

The ellipsis in equation (1.18) stands for possible variations of the f^α fields and $\tilde{T}_{\alpha\beta}$ represents the physical energy-momentum tensor defined with the metric $\tilde{g}_{\alpha\beta}$. Considering the remaining actions of U_μ and ϕ and putting things together, we end up with

$$G_{\alpha\beta} = 8\pi G[\tilde{T}_{\alpha\beta} + (1 - e^{-4\phi})U^\mu\tilde{T}_{\mu(\alpha}U_{\beta)} + \tau_{\alpha\beta}] + \Theta_{\alpha\beta}, \tag{1.19}$$

where

$$\tau_{\alpha\beta} = \sigma^2\left[\phi_{,\alpha}\phi_{,\beta} - \frac{1}{2}g^{\mu\nu}\phi_{,\mu}\phi_{,\nu}g_{\alpha\beta} - U^\mu\phi_{,\mu}(U_{(\alpha}\phi_{,\beta)} - \frac{1}{2}U^\nu\phi_{,\nu}g_{\alpha\beta})\right] - \frac{G\sigma^4}{4l^2}F(kG\sigma^2)g_{\alpha\beta} \tag{1.20}$$

and

$$\Theta_{\alpha\beta} = K\left(g^{\mu\nu}U_{[\mu,\alpha]}U_{[\nu,\beta]} - \frac{1}{4}g^{\sigma\tau}g^{\mu\nu}U_{[\sigma,\mu]}U_{[\tau,\nu]}g_{\alpha\beta}\right) - \lambda U_\alpha U_\beta. \tag{1.21}$$

Again, compared to classical electrodynamics, equation (1.21) corresponds to the energy-momentum tensor of an electromagnetic field, including an effective mass term $-\lambda U_\alpha U_\beta$.

B. Equation for the scalar field

Varying σ in S_s yields the previously mentioned relation between σ and $\phi_{,\mu}$:

$$-kG\sigma^2F - \frac{1}{2}(kG\sigma^2)^2F' = kl^2h^{\mu\nu}\phi_{,\mu}\phi_{,\nu}. \tag{1.22}$$

In equation (1.22), F' is the derivative of F with respect to its argument, i.e $F' := (dF(\mu)/d\mu)$. Equation (1.22) enables us to substitute the field σ in terms of $\phi_{,\mu}$ as will become clear below.

When we turn to the variation of ϕ, we have to keep in mind that this field enters S_m solely through $\tilde{g}^{\mu\nu}$, thus using equation (1.16) and (1.18) we obtain:

$$\left[\sigma^2h^{\mu\nu}\phi_{,\mu}\right]_{;\nu} = \left[g^{\mu\nu} + (1 + e^{-4\phi})U^\mu U^\nu\right]\tilde{T}_{\mu\nu}. \tag{1.23}$$

Compared to equation (1.22) this is an equation for ϕ only, with the physical energy-momentum tensor $\tilde{T}_{\mu\nu}$ as source. Let us define a function $\mu(y)$ by

$$-\mu F(\mu) - \frac{1}{2}\mu^2F'(\mu) = y, \tag{1.24}$$

so that

$$kG\sigma^2 = \mu(kl^2h^{\mu\nu}\phi_{,\mu}\phi_{,\nu}). \tag{1.25}$$

Now we can rewrite equation (1.23) as

$$\left[\mu(kl^2h^{\mu\nu}\phi_{,\mu}\phi_{,\nu})h^{\alpha\beta}\phi_{,\alpha}\right]_{;\beta} = kG\left[g^{\alpha\beta} + (1 + e^{-4\phi})U^\alpha U^\beta\right]\tilde{T}_{\alpha\beta}. \tag{1.26}$$

By eliminating σ with help of equation (1.22) and (1.24), we have obtained one single equation for the scalar field ϕ. Since $F(\mu)$ is a free function, also $\mu(y)$ will be free. From equation (1.26), we notice that the scalar field's coupling to matter depends on the constant k as well as on the field's kinetic energy since we have $\mu = \mu(kl^2h^{\mu\nu}\phi_{,\mu}\phi_{,\nu})$. In section 1.3.2, we will show that this kind of coupling enables us to have both a Newtonian and a MONDian behavior in TeVeS choosing an appropriate form of the function μ.

C. Equations for the vector field

Variation of S with respect to U_α and using equation (1.16) gives the vector equation

$$K\left[U^{[\alpha;\beta]}\right]_{;\beta} + \lambda U^\alpha + 8\pi G\sigma^2 U^\beta \phi_{,\beta} g^{\alpha\gamma}\phi_{,\gamma} = 8\pi G(1-e^{-4\phi}) g^{\alpha\mu}U^\beta \tilde{T}_{\mu\beta}. \tag{1.27}$$

Clearly, (1.27) corresponds to a set of Maxwell-type equations for a field with an effective mass depending on both the scalar field ϕ and the matter content. The Lagrange multiplier λ can be found by contracting equation (1.27) with U_α. Substituting it back leads to

$$\begin{aligned} &K\left(\left[U^{[\alpha;\beta]}\right]_{;\beta} + U^\alpha U_\gamma \left[U^{[\gamma;\beta]}\right]_{;\beta}\right) + 8\pi G\sigma^2\left[U^\beta\phi_{,\beta}g^{\alpha\gamma}\phi_{,\gamma} + U^\alpha\left(U^\beta\phi_{,\beta}\right)^2\right] \\ &= 8\pi G(1-e^{-4\phi})\left[g^{\alpha\mu}U^\beta\tilde{T}_{\mu\beta} + U^\alpha U^\beta U^\gamma \tilde{T}_{\gamma\beta}\right]. \end{aligned} \tag{1.28}$$

As both its sides are orthogonal to U^α, equation (1.28) has only three independent components, with the fourth being determined by the normalization equation (1.6). Similar to the gauge freedom in electrodynamics, however, equation (1.28) does not determine U_μ uniquely.

D. The physical energy-momentum tensor

Whenever needed, we will assume the matter to be an ideal fluid. Its energy-momentum tensor has the form

$$\tilde{T}_{\mu\nu} = \tilde{\rho}\tilde{u}_\mu\tilde{u}_\nu + \tilde{p}(\tilde{g}_{\mu\nu} + \tilde{u}_\mu\tilde{u}_\nu), \tag{1.29}$$

where $\tilde{\rho}$ is the energy density, $\tilde{p}$ the pressure and $\tilde{u}_\mu$ the 4-velocity, all of them expressed in the physical metric $\tilde{g}_{\mu\nu}$. If $\tilde{u}_\mu$ is collinear with U_μ, equation (1.26) can be simplified. We choose

$$\tilde{u}_\mu = e^\phi U_\mu \tag{1.30}$$

because the velocity has to be normalized with respect to $\tilde{g}_{\mu\nu}$ and find

$$\tilde{g}_{\mu\nu} + \tilde{u}_\mu\tilde{u}_\nu = e^{-2\phi}(g_{\mu\nu} + U_\mu U_\nu). \tag{1.31}$$

Inserting this for $\tilde{T}_{\mu\nu}$, we can recast equation (1.26):

$$\left[\mu(kl^2 h^{\mu\nu}\phi_{,\mu}\phi_{,\nu})h^{\alpha\beta}\phi_{,\alpha}\right]_{;\beta} = kG(\tilde{\rho} + 3\tilde{p})e^{-2\phi}. \tag{1.32}$$

E. Solutions for the vector field

As we have seen in the last section, we can benefit from any scenario that leads to a form of the vector field given by equation (1.30). Bekenstein has pointed out that in cosmological and quasistatic situations solutions for the vector field take the form $U^\mu = \delta^\mu_t$ and $U^\mu = N\delta^\mu_t$, respectively ($N = \sqrt{-g_{\mu\nu}\delta^\mu_t\delta^\nu_t}$, U^μ is properly normalized), which allows us to make use of equation (1.32) when considering these systems.

In cosmological situations, this is due to the fact that we require the fields ϕ, σ and U^μ to partake of the symmetries of the Friedmann-Robertson-Walker (FRW) spacetime. Therefore, we assume these fields to depend on t only. Since we demand spatial isotropy, U^μ must point in the cosmological time direction: $U^\mu = \delta^\mu_t$. We will stop at this point and come back to cosmology in detail later.

For quasistatic systems, we assume a time-independent metric of the form

$$g_{\mu\nu}dx^\mu dx^\nu = g_{tt}(x^k)dt^2 + g_{ij}(x^k)dx^i dx^j, \tag{1.33}$$

and no energy flow, i.e. $\tilde{T}_{jt} = 0$. Additionally, we require the fields to match the values of their analogous cosmological fields at spatial infinity:

$$\phi \to const. \quad , \qquad U^{\mu} \to \delta^{\mu}_{t}.$$

Now the given solution $U^{\mu} = N\delta^{\mu}_{t}$ can be verified by simply inserting it into the corresponding field equations.

F. GR Limit and Matter Coupling

Bekenstein has shown that for both cosmological and quasistatic systems the limit ($k \to 0$, $l \propto k^{-\frac{3}{2}}$, $K \propto k$) of TeVeS is GR. Moreover, he remarks that GR actually follows from TeVeS in a more generic limit ($K \to 0$, $l \to \infty$) with k arbitrary. Since the constants k and K describe the field-matter coupling of ϕ and U_{μ}, respectively, we may ask ourselves what kind of coupling we can choose in order to recover the successes of GR, i.e. the observed Newtonian behavior. As will become clear in section 1.3, the Newtonian limit in nonrelativistic situations would be violated if the matter coupling of these fields was strong. Therefore, we shall assume the constants k and K to be very small for any further analysis, i.e.

$$k \ll 1 \qquad , \qquad K \ll 1.$$

If this is the case, TeVeS can rightly be regarded as a modification of GR.

1.2.3 The Free Functions $y(\mu)$ and $F(\mu)$

As there is no theory for the functions $F(\mu)$ or $y(\mu)$, we have great freedom in choosing them. Let us begin, as a first example, with a function $y(\mu)$ of the form

$$y = \frac{b}{4}\frac{\mu^2(\mu-2)^2}{1-\mu}, \tag{1.34}$$

where b is a real constant. The function $y(\mu)$ is plotted in Figure 1.3 with the parameter $b = 3$.

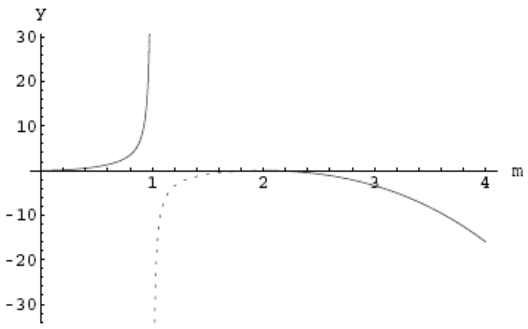

Figure 1.3: The free function $y(\mu)$ with parameter $b = 3$. Quasistationary systems are described where $0 < \mu < 1$ and cosmology where $2 < \mu < \infty$ (Bekenstein, 2004).

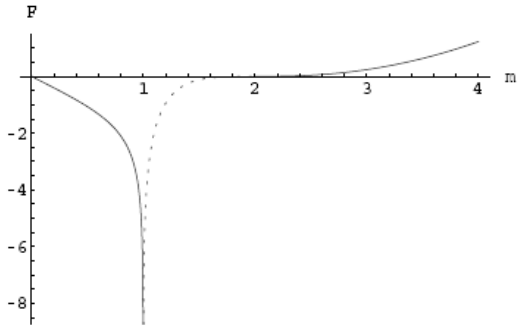

Figure 1.4: The free function $F(\mu)$ with parameter $b = 3$. Quasistationary systems are described where $0 < \mu < 1$ and cosmology where $2 < \mu < \infty$ (Bekenstein, 2004).

As y ranges from 0 to ∞, $\mu(y)$ increases monotonically from 0 to unity. For small y we have

$$\mu(y) \approx \sqrt{\frac{y}{b}}. \tag{1.35}$$

For negative y the function $\mu(y)$ is double-valued. While y decreases from 0, the far right branch increases monotonically from $\mu = 2$ and diverges as $y \to -\infty$. We take this branch to be the

physical one. What are the essential features of the free function $y(\mu)$ in order to describe the correct physics? First of all, the denominator in equation (1.34) ensures that $y(\mu) \to \infty$ when μ approaches unity, which, as we shall see in the next section, is responsible for TeVeS to have a Newtonian limit. Likewise, the behavior in equation (1.35) forces the MONDian limit to be contained in the theory. The factor $(\mu-2)^2$ ensures the existence of a monotonically decreasing branch of $\mu(y)$ covering the whole range $y \in [0, -\infty)$, which is relevant for cosmology (see section 1.4).

Integrating equation (1.34), we obtain

$$F(\mu) = \frac{b}{8}\frac{\mu(4+2\mu-4\mu^2+\mu^3)+2\log(1-\mu)^2}{\mu^2}, \tag{1.36}$$

which is shown in Figure 1.4, again with parameter b set to 3. Bekenstein points out that F contributes negative energy density in the energy-momentum tensor where $F < 0$ (see equation (1.20)), which, however, does not seem to violate the requirement of positive overall energy density.

For further analysis we shall additionally require the free functions to behave well in a physical sense, i.e to be smooth and monotonic in the corresponding regions. When dealing with gravitational lensing we shall return to the free functions and their properties concentrating on the range where $0 \leq y(\mu) < \infty$ (quasistatic systems).

1.3 Nonrelativistic Limit of TeVeS

1.3.1 Quasistatic Systems

In this section, we consider a quasistatic situation, i.e. a weak potential and slow motion situation, such as a galaxy or the solar system. In this case we can neglect time derivatives in comparison to spatial ones. In addition, we assume that the metric $g_{\mu\nu}$ is flat and that $|\phi| \ll 1$. Linearizing equation (1.19) in terms of the Newtonian potential V generated by the energy content on its r.h.s. yields

$$g_{tt} = -(1+2V) + \mathcal{O}(V^2). \tag{1.37}$$

Starting from equation (1.33) and using the corresponding solution for the vector field $U^\mu = N\delta^\mu_t$ (see section 1.2.2 E), we get

$$U_\mu = -(1+V) + \mathcal{O}(V^2). \tag{1.38}$$

Taking equation (1.7) into account, we finally end up with

$$\tilde{g}_{tt} = -(1+2V+2\phi) + \mathcal{O}(V^2) + \mathcal{O}(\phi^2). \tag{1.39}$$

Therefore, in TeVeS the total gravitational potential in the nonrelativistic approximation is given by

$$\Phi = V + \phi. \tag{1.40}$$

Bekenstein remarks that if $\phi \to \phi_c \neq 0$ at spatial infinity (ϕ_c is the cosmological scalar field), $\tilde{g}_{tt}$ does not correspond to a Minkowski metric there. This can be fixed by rescaling either the time or the spatial coordinates by factors e^{ϕ_c} or $e^{-\phi_c}$, respectively. With respect to the new coordinates, the metric is then asymptotically Minkowskian. Nevertheless, we shall assume $|\phi_c| \ll 1$ and therefore $e^{\pm\phi_c} \approx 1$, which, as Bekenstein showed, is consistent with cosmological evolution of ϕ.

To relate Φ to the Newtonian potential Φ_N generated by the energy density $\tilde{\rho}$ (according to

Poisson's equation with gravitational constant G), we first neglect temporal derivatives in equation (1.32) by replacing $h^{\mu\nu}\phi_{,\mu} \rightarrow g^{\mu\nu}\phi_{,\mu}$:

$$\left[\mu(kl^2 g^{\mu\nu}\phi_{,\mu}\phi_{,\nu})g^{\alpha\beta}\phi_{,\alpha}\right]_{;\beta} = kG(\tilde{\rho} + 3\tilde{p})e^{-2\phi}. \tag{1.41}$$

Applying the nonrelativistic approximation, we substitute $g^{\mu\nu} \rightarrow \eta^{\mu\nu}$ as well as $e^{-2\phi} \rightarrow 1$ and set the pressure $\tilde{p}$ to zero. Thus, equation (1.41) turns into

$$\vec{\nabla}\left[\mu\left(kl^2(\vec{\nabla}\phi)^2\right)\vec{\nabla}\phi\right] = kG\tilde{\rho}. \tag{1.42}$$

Comparing equation (1.42) with Poisson's equation, we immediately see that

$$\frac{1}{k}\mu|\vec{\nabla}\phi| = \mathcal{O}(|\vec{\nabla}\Phi_N|). \tag{1.43}$$

Let us assume that we can relate the potential V to Φ_N as follows:

$$V = C\Phi_N, \tag{1.44}$$

with C being a constant of proportionality. Applying the quasistatic assumptions to the field equations and using $\phi \approx \phi_c$ and equation (1.43), we finally obtain the following expression to first order:

$$V = (e^{-\phi_c} - \frac{KC}{2})\Phi_N. \tag{1.45}$$

Because C is a constant, combination of equation (1.44) and (1.45) leads to

$$C = \frac{e^{-2\phi_c}}{1 + \frac{K}{2}}. \tag{1.46}$$

If we consider $K \ll 1$ and $\phi_c \ll 1$, we can replace C by

$$\Xi = 1 - \frac{K}{2} - 2\phi_c \tag{1.47}$$

and the total gravitational potential Φ reads

$$\Phi = \Xi\Phi_N + \phi. \tag{1.48}$$

In summary, equation (1.48) quantifies the difference between TeVeS and GR at a nonrelativistic level. Since Ξ has a value close to unity, the total potential Φ can basically be calculated as the sum of the common Newtonian potential Φ_N and an additional field, the scalar potential ϕ.

1.3.2 Spherical Systems

Considering a spherically symmetric situation and applying Gauss's theorem, equation (1.43) can be transformed into

$$\vec{\nabla}\phi = \frac{k}{4\pi\mu}\vec{\nabla}\Phi_N. \tag{1.49}$$

Assuming we already know Φ_N, for example by solving Poisson's equation, the relation above can directly be used to calculate $\vec{\nabla}\phi$ for any given inverse free function $\mu(y)$. If μ or Φ_N cannot be obtained analytically, treatment with numerical methods, which can easily be applied in the spherically symmetric case, becomes necessary.

Because of their simplicity, spherically symmetric systems are particularly suitable for analyzing the asymptotic behavior in the nonrelativistic limit. In the following, we shall investigate the effects of the free function $y(\mu)$ and its features on the scalar field ϕ for $\mu \ll 1$ and $\mu \rightarrow 1$ respectively.

A. The MONDian Limit

Taking equation (1.48), we receive the expression

$$\tilde{\mu}\vec{\nabla}\Phi = \vec{\nabla}\Phi_N, \tag{1.50}$$

with

$$\tilde{\mu} = \left(\Xi + \frac{k}{4\pi\mu}\right)^{-1}. \tag{1.51}$$

Taking the free function $y(\mu)$ from section 1.2.3 in the case of $\mu \ll 1$, equation (1.35) implies

$$\mu\left[kl^2(|\vec{\nabla}\phi|)^2\right] \approx \sqrt{\frac{k}{b}}l|\vec{\nabla}\phi|. \tag{1.52}$$

If we eliminate $\vec{\nabla}\Phi_N$ between equations (1.49) and (1.50) and introduce the definition

$$a_0 = \frac{\sqrt{bk}}{4\pi\Xi l}, \tag{1.53}$$

we get a quadratic equation for μ with the positive root given as

$$\mu = \frac{k}{8\pi\Xi}\left(-1 + \sqrt{1 + \frac{4|\vec{\nabla}\Phi|}{a_0}}\right). \tag{1.54}$$

The equation above is only valid for $|\vec{\nabla}\Phi| \ll (4\pi/k)a_0$ because otherwise the condition $\mu \ll 1$ is not fulfilled. Inserting this expression for μ into equation (1.51), we derive the MOND function

$$\tilde{\mu} = \frac{1}{\Xi}\left(-1 + \sqrt{1 + \frac{4|\vec{\nabla}\Phi|}{a_0}}\right)\left(1 + \sqrt{1 + \frac{4|\vec{\nabla}\Phi|}{a_0}}\right)^{-1}. \tag{1.55}$$

Setting $\Xi = 1 - K/2 - 2\phi_c \approx 1$ and taking $|\vec{\nabla}\Phi| \ll a_0$, equation (1.55) yields

$$\tilde{\mu} \approx \frac{|\vec{\nabla}\Phi|}{a_0}. \tag{1.56}$$

If we identify a_0 with Milgrom's constant (see section 1.1), equation (1.50) with the $\tilde{\mu}$ above just reproduces the MOND formula (equation (1.1)) in the very low acceleration regime. If we vary $|\vec{\nabla}\Phi|$ within its range of validity, equation (1.55) describes part of the intermediate MOND regime not being further specified by Milgrom's formula. Obviously TeVeS is able to mimic the MOND paradigm for not too large values of $\vec{\nabla}\Phi/a_0$.

B. The Newtonian Limit

Starting again from equation (1.49), we now consider the limit $\mu \to 1$, which corresponds to $y \to \infty$ and $|\vec{\nabla}\phi| \to \infty$. Thus, equation (1.51) becomes

$$\tilde{\mu} = \left(\Xi + \frac{k}{4\pi}\right)^{-1}, \tag{1.57}$$

and because of equation (1.50), we find the following relation between $\vec{\nabla}\Phi$ and $\vec{\nabla}\Phi_N$:

$$\vec{\nabla}\Phi = \left(\Xi + \frac{k}{4\pi}\right)\vec{\nabla}\Phi_N. \tag{1.58}$$

In the nonrelativistic and arbitrarily large $|\vec{\nabla}\Phi|$ regime, TeVeS is equivalent to Newtonian gravity except for a rescaled Newtonian gravitational constant G_N given by

$$G_N = \left(\Xi + \frac{k}{4\pi}\right) G. \tag{1.59}$$

Since Ξ is very close to unity and $k \ll 1$, we have $(\Xi + k/4\pi) \approx 1$, and therefore it is adequate to say that

$$G_N \approx G. \tag{1.60}$$

Similarly to the previous section, we can investigate part of the intermediate regime by considering dynamics for large but finite $|\vec{\nabla}\Phi|/a_0$. Expanding the r.h.s. of equation (1.34) near $\mu = 1$ leads to

$$y = \frac{b}{4(1-\mu)} + \mathcal{O}(1-\mu). \tag{1.61}$$

Dropping higher order corrections in $(k/4\pi)$, equations (1.49) and (1.50) imply that

$$y = kl^2|\vec{\nabla}\phi|^2 \approx \frac{k^3 l^2}{16\pi^2}|\vec{\nabla}\Phi|^2. \tag{1.62}$$

After neglecting the $\mathcal{O}(1-\mu)$ term in $y(\mu)$ and assuming $\Xi \approx 1$, we get

$$\mu \approx 1 - \frac{64\pi^4}{k^4}\frac{a_0^2}{|\vec{\nabla}\Phi|^2}, \tag{1.63}$$

where $|\vec{\nabla}\Phi|/a_0 \gg 8\pi^2 k^{-2}$ to ensure that $\mu \approx 1$. Making use of equations (1.63) and (1.51) and again dropping higher order terms in k, we obtain an expression for $\tilde{\mu}$ close to the Newtonian limit ($G_N \approx G$):

$$\tilde{\mu} \approx \left(1 - \frac{16\pi^3}{k^3}\frac{a_0^2}{|\vec{\nabla}\Phi|^2}\right). \tag{1.64}$$

Bekenstein mentions that equation (1.64) hints at a non-Newtonian behaviour in the strong Newtonian regime like, for example, in the solar system. Although the deviation is rather small, it could be observable in some cases. However, we emphasize that this effect is very sensitive to the specific choice of the free function.

1.3.3 Nonspherical Systems

Considering arbitrary asymmetric systems, equation (1.49) has to be replaced by the general solution of equation (1.42) given by

$$\vec{\nabla}\phi = \frac{k}{4\pi\mu}(\vec{\nabla}\Phi_N + \vec{\nabla} \times \vec{h}), \tag{1.65}$$

where $\vec{h}$ is some regular vector field which is determined up to a gradient by the condition that the curl of the r.h.s. of equation (1.65) vanishes. Thus, any problem can basically be solved by figuring out a corresponding value for $\vec{h}$ and using equation (1.65) together with the Newtonian potential Φ_N to get $\vec{\nabla}\phi$.

However, instead of dealing with $\vec{h}$, we shall return to equation (1.42) in order to approach a more "direct" way of getting ϕ. Expansion of the l.h.s. yields

$$(\vec{\nabla}\mu)(\vec{\nabla}\phi) + \mu\Delta\phi = kG\tilde{\rho}. \tag{1.66}$$

Since $\mu = \mu(y)$ and $y = kl^2|\vec{\nabla}\phi|^2$, we find

$$\vec{\nabla}\mu = 2\frac{\partial\mu}{\partial y}kl^2|\vec{\nabla}\phi|\left(\vec{\nabla}|\vec{\nabla}\phi|\right), \tag{1.67}$$

with

$$\left(\vec{\nabla}|\vec{\nabla}\phi|\right)_i = \frac{1}{|\vec{\nabla}\phi|}(\partial_j\phi)(\partial_i\partial_j\phi). \tag{1.68}$$

Taking the results from above, equation (1.66) can now be expressed as

$$2\frac{\partial\mu}{\partial y}kl^2\left((\partial_i\phi)(\partial_j\phi)(\partial_i\partial_j\phi)\right) + \mu\Delta\phi = kG\tilde{\rho}. \tag{1.69}$$

Equation (1.69) is a nonlinear partial differential equation (PDE) which can be solved numerically. When dealing with gravitational lenses, we shall come back to equation (1.69), giving a detailed description of the numerical method we use to obtain a solution for the scalar field ϕ.

1.4 Cosmology in TeVeS

1.4.1 Basic Assumptions

Throughout this whole section, we shall require our considerations to satisfy the following two assumptions:

First of all, observational properties of the universe are isotropic if averaged over sufficiently large distances, i.e. regardless of which direction we choose, we will always make the same observations.
Secondly, no position in the universe is preferred to any other one. These assumptions are commonly known as the *cosmological principle*.

If we combine these two assumptions, we can rephrase them as the requirement of a homogeneous and isotropic universe.

1.4.2 Brief Review of Cosmology in GR

A. Choice of the Metric

Since gravity is the only relevant force on cosmological scales, the first step is simply finding a metric that satisfies our assumptions. Because of isotropy, we shall require the spatial part of this metric to be spherically symmetric. A metric that already contains this feature is given by a FRW metric

$$ds^2 = -dt^2 + a^2(t)\left[d\chi^2 + f_K^2(\chi)d\omega^2\right], \tag{1.70}$$

where we have introduced a set of polar coordinates (χ, θ, φ) with

$$d\omega^2 = d\theta^2 + \sin^2\theta d\varphi^2 \tag{1.71}$$

and a radial function $f_K(\chi)$.

The choice of the function $f_K(\chi)$ is restricted by the requirement of homogeneity. It can be shown that $f_K(\chi)$ is linear, trigonometric or hyperbolic in χ, which corresponds to a flat, closed or open universe, respectively:

$$f_K(\chi) = \begin{cases} K^{-\frac{1}{2}}\sin(K^{\frac{1}{2}}\chi) & (K>0) \\ \chi & (K=0) \\ |K|^{-\frac{1}{2}}\sinh(|K|^{\frac{1}{2}}\chi) & (K<0) \end{cases}, \tag{1.72}$$

where K is a constant parameterizing the curvature of spatial hypersurfaces, $f_K(\chi)$ and $|K|^{-\frac{1}{2}}$ have the dimension of a length. Thus, equations (1.70) and (1.72) describe the metric for a homogeneous and isotropic universe.

B. Redshift

Due to the time evolution of the scale factor $a(t)$, spatial hypersurfaces can expand or shrink, which leads to a positive or negative frequency shift of photons propagating through space-time. If we consider light emitted from a comoving source at time t_e reaching a comoving observer at $\chi = 0$ at time t_0, we have

$$|dt| = a(t)d\chi \tag{1.73}$$

according to $ds = 0$ for light. The distance between source and observer can be calculated by integrating $d\chi$ over time, i.e.

$$\chi_{eo} = \int_{\chi(t_e)}^{\chi(t_0)} d\chi = \int_{t_e}^{t_0} \frac{dt}{a(t)} = const. \tag{1.74}$$

Because χ_{eo} is constant, its derivative with respect to the emission time t_e must vanish,

$$\frac{d\chi_{eo}}{dt_e} = \frac{1}{a_{t_0}} \frac{dt_0}{dt_e} - \frac{1}{a(t_e)} = 0, \tag{1.75}$$

and we obtain

$$\frac{dt_0}{dt_e} = \frac{a(t_0)}{a(t_e)}. \tag{1.76}$$

As the time difference dt is reciprocal to the frequency ω, we have

$$\frac{\omega_e}{\omega_0} = \frac{a(t_0)}{a(t_e)}. \tag{1.77}$$

Now we can define the redshift z by

$$z = \frac{a(t_0)}{a(t_e)} - 1, \tag{1.78}$$

Thus, for an expanding universe ($a(t_0) > a(t_e)$) we have $z > 0$ and the observed light is redshifted.

C. Friedmann's Equations

In GR, Einstein's field equations read as follows:

$$G_{\mu\nu} = 8\pi G T_{\mu\nu} + \Lambda g_{\mu\nu}. \tag{1.79}$$

Here, $G_{\mu\nu}$ is again the Einstein tensor, $T_{\mu\nu}$ the energy-momentum tensor of the cosmic fluid and Λ the cosmological constant. Like before, $T_{\mu\nu}$ has the form of an energy-momentum tensor of a perfect fluid and is characterized by the energy density ρ and the pressure p, both of them being dependent on time only because of homogeneity, i.e.

$$p = p(t), \quad \rho = \rho(t). \tag{1.80}$$

Inserting the metric (1.70) into equation (1.79), Einstein's equations reduce to the following two differential equations for the scale factor $a(t)$ which are known as Friedmann's equations:

$$\left(\frac{\dot{a}}{a}\right)^2 = \frac{8\pi G}{3}\rho - \frac{K}{a^2} + \frac{\Lambda}{3} \tag{1.81}$$

$$\frac{\ddot{a}}{a} = -\frac{4\pi G}{3}(\rho + 3p) + \frac{\Lambda}{3} \tag{1.82}$$

These equations determine the evolution of $a(t)$ once it is given for a certain time t_0, for example, we shall set $a(t_{today}) = 1$.

Combination of equations (1.81) and (1.82) yields the adiabatic equation:

$$\frac{d}{dt}(a^3\rho) + p\frac{d}{dt}a^3 = 0 \tag{1.83}$$

The first term obviously denotes the change in internal energy, the second one is the pressure work. Thus, equation (1.83) states the conservation of energy in the cosmological framework.

Making use of equation (1.83), we now derive expressions for $\rho(t)$ and $p(t)$, respectively. In case of relativistic particles (radiation), the pressure can be written as

$$p = \frac{\rho}{3} \tag{1.84}$$

and equation (1.83) reduces to

$$\frac{\dot{\rho_r}}{\rho_r} = -4\frac{\dot{a}}{a}, \tag{1.85}$$

and therefore

$$\rho_r(t) = \frac{\rho_{r0}}{a^4}, \tag{1.86}$$

where ρ_{r0} is the present density according to $a(t_{today}) = 1$. For non-relativistic matter (dust), we can assume $p \approx 0$ and equation (1.83) turns into

$$\frac{\dot{\rho_m}}{\rho_m} = -3\frac{\dot{a}}{a} \tag{1.87}$$

implying

$$\rho_m(t) = \frac{\rho_{m0}}{a^3}. \tag{1.88}$$

Substituting equations (1.86) and (1.88) by $\rho(t) = \rho_r(t) + \rho_m(t)$ into (1.81), we receive one single equation for the dynamics of the scale factor $a(t)$.

D. Parameterization

In order to achieve a better view on the equations above, it is convenient to introduce both dimensional and dimensionless parameters. First of all, we define the Hubble parameter as the relative expansion rate,

$$H(t) := \frac{\dot{a}}{a}, \quad H_0 := H(t_{today}), \tag{1.89}$$

where the Hubble constant H_0 is approximately given by

$$H_0 \approx 70\frac{km}{sMpc}. \tag{1.90}$$

Using the Hubble parameter, we can move on and define the critical density,

$$\rho_{cr}(t) := \frac{3H^2(t)}{8\pi G}, \quad \rho_{cr0} := \frac{3H_0^2}{8\pi G}, \tag{1.91}$$

and expressing densities in units of the critical density finally leads to the dimensionless density parameters:

$$\Omega(t) := \frac{\rho(t)}{\rho_{cr}(t)}, \quad \Omega_0 := \Omega(t_{today}) = \frac{\rho(t_{today})}{\rho_{cr0}}. \tag{1.92}$$

Additionally, we may introduce

$$\Omega_\Lambda(t) := \frac{\Lambda}{3H^2(t)}, \quad \Omega_{\Lambda 0} := \frac{\Lambda}{3H_0^2} \tag{1.93}$$

and

$$\Omega_K := -\frac{K}{H_0^2} = 1 - \Omega_{r0} - \Omega_{m0} - \Omega_{\Lambda 0}. \tag{1.94}$$

Resubstituting all of the above in it, we can recast equation (1.81) into

$$H^2(a) = H_0^2 \left[\frac{\Omega_{r0}}{a^4} + \frac{\Omega_{m0}}{a^3} + \Omega_{\Lambda 0} + \frac{\Omega_K}{a^2} \right] = H_0^2 E^2(a). \tag{1.95}$$

E. Comoving and Angular Diameter Distances

The comoving distance D_C is the distance on the spatial hypersurface at $t = const.$ between the world lines of a source and an observer comoving with the mean cosmic flow. Therefore, we have $dD_C = d\chi$, and because light rays propagate according to $ds = 0$, integration yields

$$D_C(a(z_1), a(z_2)) = \int_{a(z_2)}^{a(z_1)} \frac{da}{a\dot{a}} = \frac{1}{H_0} \int_{a(z_2)}^{a(z_1)} \frac{da}{a^2 E(a)}. \tag{1.96}$$

Using $a^2 dz = -da$, we can express equation (1.96) in terms of redshift z

$$D_C(z_1, z_2) = \frac{1}{H_0} \int_{z_1}^{z_2} \frac{dz'}{E(z')}, \tag{1.97}$$

where $E(z)$ is given by

$$E(z) = \left(\Omega_{r0}(1+z)^4 + \Omega_{m0}(1+z)^3 + \Omega_{\Lambda 0} + \Omega_K(1+z)^2 \right)^{\frac{1}{2}}. \tag{1.98}$$

The angular diameter distance is defined in accordance with the relation in Euclidean space $\delta\omega D_{A,E}^2 = \delta A$. As the solid angle at constant χ is scaled by $f_K(\chi)$ in the metric (1.70), we find

$$\frac{\delta A}{4\pi a^2(z_2) f_K^2(D_C(z_1, z_2))} = \frac{\delta\omega}{4\pi} \tag{1.99}$$

and get

$$D_A(z_1, z_2) = a(z_2) f_K(D_C(z_1, z_2)) = \frac{1}{1+z_2} f_K(D_C(z_1, z_2)). \tag{1.100}$$

1.4.3 The Modified Friedmann Equations

In the TeVeS context, we need to consider equation (1.19) and, of course, the physical picture with its quantities keeping the assumptions of section 1.4.1 and the FRW metric (1.70). Since we are referring to cosmology, we take $U^\mu = \delta_t^\mu$ and $\phi = \phi(t)$ (see section 1.2.2 E).

Now we can simplify some of the basic equations. First of all, we return to equation (1.26) which reduces to

$$\mu\ddot{\phi} + \left(3\mu\frac{\dot{a}}{a} + \dot{\mu} \right) \dot{\phi} + \frac{kG}{2}(\tilde{\rho} + 3\tilde{p})e^{-2\phi} = 0. \tag{1.101}$$

This is the equation of motion of the scalar field ϕ in a FRW background. Once the free function is specified, the full time evolution of ϕ is given by the equation above.

Secondly, the tt components of equations (1.20) and (1.21) now take the form

$$\tau_{tt} = 2\sigma^2\dot{\phi}^2 + \frac{G\sigma^4}{4l^2} F(\mu) \tag{1.102}$$

and

$$\Theta_{tt} = 8\pi G(2\tilde{\rho}\sinh(2\phi) - \sigma^2\dot{\phi}^2), \tag{1.103}$$

respectively.

Inserting the above expressions into the tt component of equation (1.19), we arrive at the following analog of equation (1.81):

$$\left(\frac{\dot{a}}{a}\right)^2 = \frac{8\pi G}{3}(\tilde{\rho}e^{-2\phi} + \rho_\phi) - \frac{K}{a^2} + \frac{\Lambda}{3}, \tag{1.104}$$

where ρ_ϕ is the energy density of the scalar field,

$$\rho_\phi = \frac{\mu\dot{\phi}^2}{kG} + \frac{\mu^2}{4k^2l^2G}F(\mu) = \frac{-2\mu y(\mu) + \mu^2 F(\mu)}{4k^2l^2G}. \tag{1.105}$$

With our choice (1.34) for $y(\mu)$ and the equations in section 1.2.2 B, we have $\mu > 0$, $y(\mu) < 0$ and $F(\mu) > 0$ in the cosmological domain. For this reason, the scalar field contributes positive energy density ensuring a positive overall energy density in equation (1.104) and thus a consistent cosmology.

Similarly, one can derive the corresponding equation for (1.82):

$$\frac{\ddot{a}}{a} = -\frac{4\pi G}{3}(\tilde{\rho}e^{-2\phi} + \rho_\phi + 3\tilde{p}e^{-2\phi} + 3p_\phi) + \frac{\Lambda}{3}, \tag{1.106}$$

with the pressure p_ϕ of the scalar field,

$$p_\phi = \frac{\mu\dot{\phi}^2}{kG} - \frac{\mu^2}{4k^2l^2G}F(\mu). \tag{1.107}$$

Since we are interested in the physical quantities, we actually have to switch over to the physical picture, i.e. we need to determine the physical metric of (1.70). Applying the transformation (1.7), we find

$$\tilde{g}_{\mu\nu}dx^\mu dx^\nu = -d\tilde{t}^2 + \tilde{a}(\tilde{t})^2[d\chi^2 + f(\chi)^2 d\omega^2], \tag{1.108}$$

with

$$d\tilde{t} = e^{\phi}dt, \quad \tilde{a} = e^{-\phi}a, \tag{1.109}$$

which implies the following relation:

$$\frac{d\tilde{a}}{d\tilde{t}} = e^{-2\phi}(\dot{a} - a\dot{\phi}). \tag{1.110}$$

Using this relation, we are able to obtain the "physical Friedmann equations" in terms of the physical scale factor $\tilde{a}(\tilde{t})$ and the physical time scale $\tilde{t}$:

$$\frac{1}{\tilde{a}}\frac{d\tilde{a}}{d\tilde{t}} = e^{-\phi}\left(\frac{\dot{a}}{a} - \dot{\phi}\right) \tag{1.111}$$

and

$$\frac{1}{\tilde{a}}\frac{d^2\tilde{a}}{d\tilde{t}^2} = e^{-2\phi}\left(\frac{\ddot{a}}{a} - 3\frac{\dot{a}}{a}\dot{\phi} + 2\dot{\phi}^2 - \ddot{\phi}\right). \tag{1.112}$$

In principle, one can now specify any suitable form of the free function $F(\mu)$ and the equation of state of the matter content, which eventually leads to a closed system of equations that needs to be solved. However, in section 1.4.6 we shall develop a simple cosmological model which will suffice for our purposes.

1.4.4 Physical Redshift and Physical Distances

In analogy to the GR case, we can introduce the physical redshift $\tilde{z}$ and the physical distances $\tilde{D}_i$. The way to do this is identical to sections 1.4.2 B,E except for the fact that we have to take the physical metric (1.108) instead of (1.70). According to $d\tilde{s} = 0$, equation (1.74) turns into

$$\int_{\tilde{t_e}}^{\tilde{t_0}} \frac{d\tilde{t}}{\tilde{a}(\tilde{t})} = \int_{t_e}^{t_0} e^{2\phi(t)} \frac{dt}{a(t)} \tag{1.113}$$

Thus, we obtain for the the physical redshift:

$$\tilde{z} = \frac{\tilde{a}(\tilde{t_0})}{\tilde{a}(\tilde{t_e})} - 1. \tag{1.114}$$

Likewise, equations (1.97) and (1.100) transform to

$$\tilde{D}_C = \int_{\tilde{z}_1}^{\tilde{z}_2} \frac{d\tilde{z}'}{\tilde{H}(\tilde{z}')} \tag{1.115}$$

and

$$\tilde{D}_A = \frac{1}{1+\tilde{z}_2} f_K(\tilde{D}_C(\tilde{z}_1, \tilde{z}_2)), \tag{1.116}$$

where we have used the definition of the physical Hubble parameter given by

$$\tilde{H} = \frac{\dot{\tilde{a}}}{\tilde{a}}. \tag{1.117}$$

Comparing GR and TeVeS, we notice that while the formal structure of the equations above stays the same, the time evolution of the physical scale factor now additionally involves the time evolution of the scalar field ϕ according to (1.104) and (1.109) – (1.112).

1.4.5 Simplistic Minimal-Matter Open Cosmology

A. The "Slow Roll" Approximation

Let us assume that the scalar field ϕ changes slowly in time. Then we may set its time derivatives to zero, i.e. $\dot{\phi} \sim \ddot{\phi} \sim 0$. Since we are in the cosmological regime ($2 < \mu < \infty$), it follows from equation (1.22) that $\mu = 2$, $y = 0$ and $F = 0$ referring to our choice of the free functions in section 1.2.3. Substituting this into equations (1.105) and (1.107), energy density and pressure of the scalar field reduce to

$$\rho_\phi = 0, \quad p_\phi = 0 \tag{1.118}$$

and we arrive at the following expressions:

$$\left(\frac{1}{\tilde{a}}\frac{d\tilde{a}}{d\tilde{t}}\right)^2 = e^{-2\phi}\left(\frac{8\pi G}{3}\tilde{\rho}e^{-2\phi} - \frac{K}{a^2} + \frac{\Lambda}{3}\right), \tag{1.119}$$

$$\frac{1}{\tilde{a}}\frac{d^2\tilde{a}}{d\tilde{t}^2} = e^{-2\phi}\left(-\frac{4\pi G}{3}(\tilde{\rho} + 3\tilde{p})e^{-2\phi} + \frac{\Lambda}{3}\right). \tag{1.120}$$

Remembering that in the cosmological domain it is consistent to take $0 \leq \phi \ll 1$ (section 1.3.1), we have $e^{-2\phi} \approx 1$ and get

$$\left(\frac{1}{\tilde{a}}\frac{d\tilde{a}}{d\tilde{t}}\right)^2 = \frac{8\pi G}{3}\tilde{\rho} - \frac{K}{a^2} + \frac{\Lambda}{3}, \tag{1.121}$$

$$\frac{1}{\tilde{a}}\frac{d^2\tilde{a}}{d\tilde{t}^2} = -\frac{4\pi G}{3}(\tilde{\rho} + 3\tilde{p}) + \frac{\Lambda}{3}. \tag{1.122}$$

If we refer to the physical observables, this result coincides with the one we have obtained from GR.

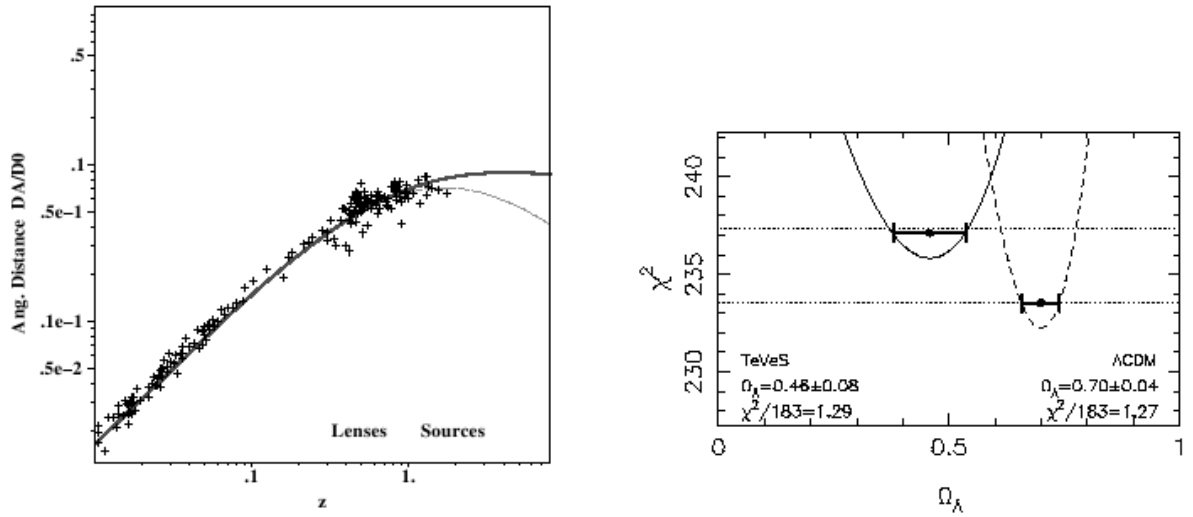

Figure 1.5: Left: Angular diameter distance D_A (in units of the critical distance $D_0 = a_0^{-1} \sim 6H_0^{-1}$) as a function of redshift z in two cosmologies: $(\Omega_{m0}, \Omega_{\Lambda 0}) = (0.04, 0.46)$ (minimal-matter cosmology, thick solid) and $(\Omega_{m0}, \Omega_{\Lambda 0}) = (0.25, 0.75)$ (ΛCDM, thin dashed). The data was converted from luminosity distances to angular diameter distances according to $D_A = (1+z)^{-2} D_L$ assuming $H_0 = 70 kms^{-1} Mpc^{-1}$. Right: The minimal-matter cosmology fit to high-z SNeIa luminosity distance modulus is slightly poorer than the ΛCDM flat cosmology fit, but only by $\Delta\chi^2 = 3.5$ or 1.9σ; error bars indicate the $\pm 1\sigma$ limit on the estimated Ω_Λ (Zhao et al., 2006).

B. A Simple Cosmological Model

As concluded by Bekenstein, the contribution of the scalar field to the Hubble expansion is of $\mathcal{O}(k)$, hence we shall neglect it for further analysis. Following Zhao et al. (2006), we make use of the "slow roll" approximation, which enables us to express the physical Hubble parameter as $(\tilde{a}(\tilde{t}) \approx a(t))$

$$\tilde{H}^2 \approx H^2 \approx H_0^2 \left(\Omega_{m0}(1+z)^3 + \Omega_{\Lambda 0} + \Omega_K (1+z)^2 \right), \tag{1.123}$$

where $\Omega_K \approx 1 - \Omega_{\Lambda 0} - \Omega_{m0}$ and $\Omega_{r0} \approx 0$.

Since there is no DM in TeVeS, we consider a minimal-matter cosmology that should be consistent with Supernovae (SNe Ia) data in order to obtain a reasonable cosmological model. For example, we actually find a good fit of the high-z SNe distance moduli data set by choosing an open cosmology with $\Omega_{\Lambda 0} \sim 0.46$, $\Omega_{m0} \sim 0.04$ and $H_0 \sim 70 km/s/Mpc$. Figure 1.5 shows the angular diameter distance as a function of redshift for both a minimal-matter cosmology and a standard ΛCDM model. Although the minimal-matter cosmology fit is slightly poorer, we see that the two models are in accordance with the data set. Zhao et al. also point out that when moving to very high redshifts, this open cosmology has problems, i.e. it underestimates the last scattering sound horizon, which is actually an artifact of our simplifications as recent work has shown (Zhao, 2006). Nevertheless, in the context of gravitational lensing this simple model is sufficient for assigning the distances of lenses and sources up to a redshift of $z \sim 3$.

2 Gravitational Lensing in TeVeS

Now that we have familiarized ourselves with TeVeS gravity, we shall apply our knowledge to the phenomenon of gravitational light deflection. After a brief introduction, we will have a look at gravitational lensing in GR and its analog in TeVeS, ending the chapter with an analysis of analytical lens models and their properties within the TeVeS universe.

2.1 Gravitational Light Deflection

2.1.1 Physical Geodesics

The propagation of light in curved spacetimes is in general a very complicated problem. According to $ds = 0$ (GR), light rays move along the null geodesics, and their 4-velocity $\dot{x}^\mu$ (the dot denotes the derivative with respect to some suitable affine parameter) must satisfy the following relation:

$$g_{\mu\nu}\dot{x}^\mu\dot{x}^\nu = 0. \tag{2.1}$$

Of course, if we consider TeVeS, we have to take into account that light follows the physical null geodesics, i.e. the null geodesics of the physical metric $\tilde{g}_{\mu\nu}$ ($d\tilde{s} = 0$), leading to

$$\tilde{g}_{\mu\nu}\dot{x}^\mu\dot{x}^\nu = 0. \tag{2.2}$$

Assuming an on average homogeneous and isotropic universe (see section 1.4.1) with local perturbations, light mostly travels through unperturbed spacetime and is only deflected close to inhomogeneities which act as gravitational lenses. If the nonrelativistic potential Φ and the peculiar velocity v of the lens are small, i.e.

$$\Phi \ll 1, \quad v \ll 1, \tag{2.3}$$

we can presume a locally flat spacetime which is disturbed by the potential Φ. Since these conditions are satisfied for almost all cases relevant for gravitational lensing, we will keep them for any further analysis.

2.1.2 Spherically Symmetric Systems

To get a first impression on how lensing works in TeVeS, we follow Bekenstein and consider a spherically symmetric and static metric of the form

$$ds^2 = -e^\nu dt^2 + e^\zeta \left[d\rho^2 + \rho^2(d\theta^2 + \sin^2\theta d\varphi^2)\right], \tag{2.4}$$

where

$$\nu = \nu(\rho) \ll 1, \quad \zeta = \zeta(\rho) \ll 1. \tag{2.5}$$

In this case, e^ν and e^ζ correspond to $1 + 2\Phi$ and $1 - 2\Phi$, respectively. The exponentials are only introduced to present the following calculations in a transparent way. Applying transformation (1.7), we obtain the physical metric by substituting $e^\nu \to e^{\nu+2\phi}$ and $e^\zeta \to e^{\zeta-2\phi}$, and equation (2.2) reduces to

$$-e^{\nu+2\phi}\dot{t}^2 + e^{\zeta-2\phi}(\dot{\rho}^2 + \rho^2\dot{\varphi}^2) = 0. \tag{2.6}$$

Because of stationarity and spherical symmetry, we have the conservation laws $e^{\nu+2\phi}\dot{t} = E$ and $e^{\zeta-2\phi}\rho^2\dot{\varphi} = L$, E and L being constant characteristics of the light ray. Introducing the impact parameter $b = L/E$, equation (2.6) yields

$$d\varphi = \left[e^{\zeta-\nu-4\phi}\left(\frac{\rho}{b}\right)^2 - 1\right]^{-\frac{1}{2}} \frac{d\rho}{\rho}, \tag{2.7}$$

and after some algebra we arrive at the following first-order expression of the deflection angle (primes denote derivatives with respect to ρ):

$$\Delta\varphi = \frac{b}{2}\int_{-\infty}^{\infty} \frac{\nu' - \zeta' + 4\phi'}{\rho} dx, \tag{2.8}$$

where $x = \pm(\rho^2 - b^2)^{1/2}$ is the usual Cartesian coordinate along the unperturbed light ray.

The difference between GR with DM and TeVeS is that in GR we would have $\phi = 0$ and compute ν and ζ from Einstein's equations including DM as a source, whereas in TeVeS we have to get ϕ from its field equation and compute ν and ζ also using Einstein's equations, but taking visible matter as the only source.

2.2 Basics of Gravitational Lensing

2.2.1 Lensing in GR

A. Deflection Angle

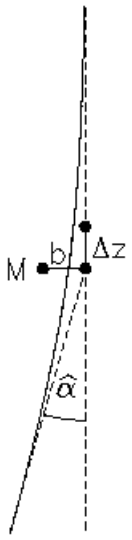

Figure 2.1: Light deflection by a point mass: The unperturbed ray passes the mass at impact parameter b, the perturbed one is deflected by the angle $\hat{\alpha}$.

If we preserve the conditions from section 2.1.1, according to Narayan & Bartelmann (1999), we can express the effect of spacetime curvature on light rays in terms of an effective index of refraction n in analogy to the deflection of light by a prism:

$$n = 1 - 2\Phi_N = 1 + 2|\Phi_N|. \tag{2.9}$$

The deflection angle of a light ray passing through a gravitational field is given by the integral along the light path of the gradient of n perpendicular to the light path, i.e.

$$\vec{\hat{\alpha}} = -\int \vec{\nabla}_\perp n dl = 2\int \vec{\nabla}_\perp \Phi_N dl. \tag{2.10}$$

Since in all cases of interest the deflection angle is small, we can simplify (2.10) by applying Born's approximation, i.e. integrating along the unperturbed light path instead of the deflected one. For example, if we consider unperturbed light rays propagating parallel to the z-axis, equation (2.10) can be written as

$$\vec{\hat{\alpha}} = 2\int_{-\infty}^{\infty} \vec{\nabla}_\perp \Phi_N dz. \tag{2.11}$$

B. Thin Lens Approximation

Figure 2.1 illustrates that most of the bending actually occurs within $\Delta z \sim \pm b$. Since Δz is much smaller than the distances between observer and lens and between lens and source, we may take the lens to be thin compared to the total extent of the light path. Therefore, the mass distribution of the lens can be projected along the line-of-sight and replaced by a mass sheet orthogonal to the line-of-sight which is characterized by its surface mass density

$$\Sigma(\vec{\xi}) = \int \rho(\vec{\xi}, z) dz, \tag{2.12}$$

where $\vec{\xi}$ is a two-dimensional vector in the lens plane. Thus, the total deflection angle caused by a mass sheet $\Sigma(\vec{\xi})$ at the position $\vec{\xi}$ is given by

$$\vec{\hat{\alpha}}(\vec{\xi}) = 4G \int \frac{(\vec{\xi} - \vec{\xi'})\Sigma(\vec{\xi'})}{|\vec{\xi} - \vec{\xi'}|} d^2\xi'. \tag{2.13}$$

In general, the deflection angle is a two-dimensional vector. For spherically symmetric systems, e.g. the point lens, the light deflection can be reduced to a one-dimensional problem.

C. Lens Equation

Figure 2.2 shows a typical gravitational lens system. According to Bartelmann & Schneider (2001), we can immediately read off Figure 2.2 that

$$\vec{\eta} = \frac{D_s}{D_d}\vec{\xi} - D_{ds}\vec{\hat{\alpha}}(\vec{\xi}), \tag{2.14}$$

where $\vec{\eta}$ denotes the two-dimensional position of the source, and the distances D_i correspond to angular diameter distances defined in section 1.4.2 E.

Introducing angular coordinates by $\vec{\eta} = D_s\vec{\beta}$ and $\vec{\xi} = D_d\theta$, equation (2.14) yields

$$\vec{\beta} = \vec{\theta} - \frac{D_{ds}}{D_s}\vec{\hat{\alpha}}(D_d\theta) = \vec{\theta} - \vec{\alpha}(\vec{\theta}), \tag{2.15}$$

where we have used the definition of the scaled deflection angle $\vec{\alpha}(\vec{\theta})$. Equation (2.15) is called the lens equation and determines the angular position $\vec{\theta}$ of the image for a given source position $\vec{\beta}$. If there is more than one solution for a fixed value of $\vec{\beta}$, the lens produces multiple images.

It is convenient to define the convergence $\kappa(\vec{\theta})$ as follows:

$$\kappa(\vec{\theta}) = \frac{\Sigma(D_d\vec{\theta})}{\Sigma_{cr}}, \tag{2.16}$$

where Σ_{cr} is the critical surface mass density given by

$$\Sigma_{cr} = \frac{1}{4\pi G}\frac{D_s}{D_d D_{ds}}. \tag{2.17}$$

Σ_{cr} is a characteristic value to distinguish between *strong* ($\kappa \geq 1$) and *weak* ($\kappa < 1$) lenses, $\kappa \geq 1$ being sufficient (but not necessary) for a lens to produce multiple images.

If we additionally introduce the deflection potential $\Psi(\vec{\theta})$,

$$\Psi(\vec{\theta}) = 2\frac{D_{ds}}{D_s D_s} \int \Phi_N(D_d\vec{\theta}, z) dz, \tag{2.18}$$

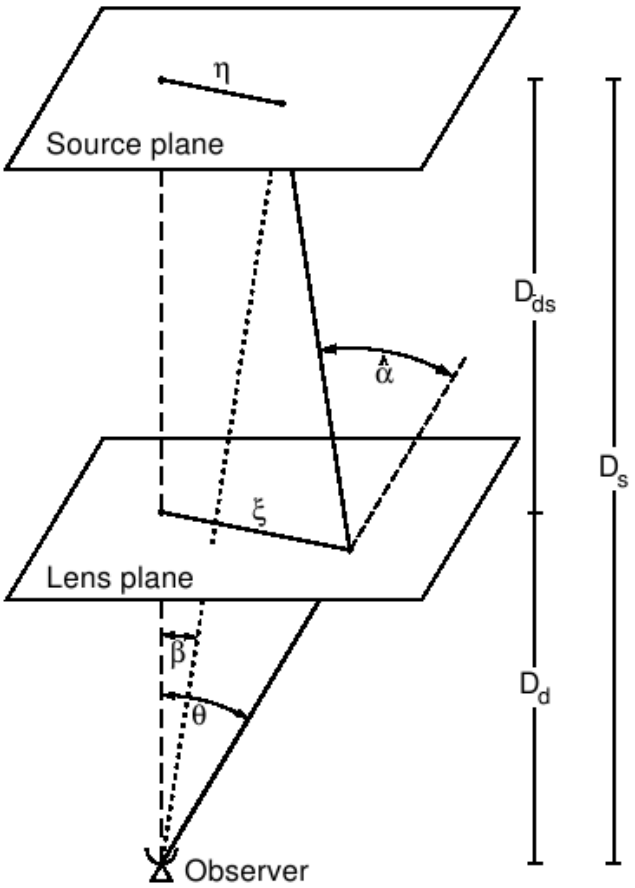

Figure 2.2: Illustration of a gravitational lens system. The distances between source and observer, lens and observer, and lens and source are D_s, D_d, and D_{ds}, respectively (Bartelmann & Schneider, 2001).

deflection angle and convergence can be written as

$$\vec{\alpha}(\vec{\theta}) = \vec{\nabla}_{\vec{\theta}}\Psi(\vec{\theta}) \tag{2.19}$$

and

$$\kappa(\vec{\theta}) = \frac{1}{2}\Delta_{\vec{\theta}}\Psi, \tag{2.20}$$

respectively.

D. Magnification and Distortion

Since light rays are deflected differentially, shapes of images and sources will differ from each other. If a source is much smaller than the angular scale on which the lens properties change, the lens mapping can locally be linearized. Thus, we can describe the distortion of the image by the Jacobian matrix

$$\mathcal{A}(\vec{\theta}) = \frac{\partial\vec{\beta}}{\partial\vec{\theta}} = \left(\delta_{ij} - \frac{\partial^2\Psi(\vec{\theta})}{\partial\theta_i\partial\theta_j}\right) = \begin{pmatrix} 1-\kappa-\gamma_1 & -\gamma_2 \\ -\gamma_2 & 1-\kappa+\gamma_1 \end{pmatrix}, \tag{2.21}$$

where κ is obtained from equation (2.20) and the shear components are given by

$$\gamma_1 = \frac{1}{2}(\Psi_{,11} - \Psi_{,22}), \quad \gamma_2 = \Psi_{,12}, \quad \gamma = |\gamma| = \sqrt{\gamma_1^2 + \gamma_2^2}. \tag{2.22}$$

As there is no absorption or emission of photons in gravitational lensing, Liouville's theorem implies that lensing conserves surface brightness, i.e. if $I^s(\vec{\beta})$ is the surface brightness distribution in the source plane, the observed surface brightness distribution in the lens plane is

$$I(\vec{\theta}) = I^s\left(\vec{\beta}(\vec{\theta})\right). \tag{2.23}$$

The fluxes observed from image and unlensed source can be calculated by integrating over the corresponding brightness distributions and their ratio is defined as the magnification μ. From elementary calculus, we know that μ is given by the inverse of the Jacobi determinant:

$$\mu = \frac{1}{det\mathcal{A}} = \frac{1}{(1-\kappa-\gamma)(1-\kappa+\gamma)}. \tag{2.24}$$

We see that images are distorted in shape and size. The convergence causes an isotropic focusing of light bundles, which leads to an isotropic magnification of the source, while the shear acting anisotropically within the lens mapping causes changes in both shape and size of the image.

E. Critical Curves and Caustics

Points in the lens plane where $det\mathcal{A} = 0$ form closed curves, the *critical curves*. Their image curves located in the source plane are called *caustics*. Because of equation (2.24), sources on caustics should be magnified by an infinitely large factor. However, since every astrophysical source is extended, its magnification remains finite. An infinitely large magnification simply does not occur in reality. However, images near critical curves can significantly be magnified and distorted, which, for instance, is indicated by the giant luminous arcs formed from source galaxies near caustics. Figure 2.3 demonstrates the mapping of an extended source by a non-

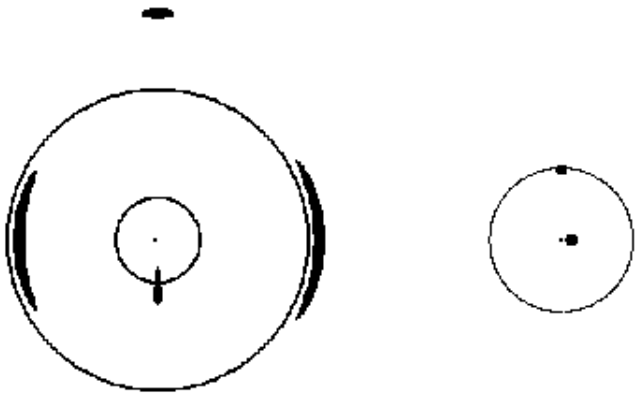

Figure 2.3: Imaging of an extended source by a non-singular circularly symmetric lens (Narayan & Bartelmann, 1999). Closed curves in the lens plane (left) are denoted *critical curves*, those in the source plane (right) *caustics*. Because of their image properties the outer and inner critical curves are called *tangential* and *radial*, respectively.

singular circularly symmetric lens. A source close to the point caustic at the lens center produces two tangentially oriented arcs close to the outer critical curve, and a faint image at the lens center. A source on the outer caustic produces a radially elongated image on the inner critical curve, and a tangentially oriented image outside the outer critical curve. Due to these image properties the outer and inner critical curve are denoted by *tangential* and *radial*, respectively. Since these curves have such interesting features, an analysis of their behavior in a TeVeS universe might be profitable.

F. The Isothermal Sphere

Let us consider a projected surface mass density profile of the following form:

$$\Sigma(\xi) \propto \frac{1}{\xi}. \tag{2.25}$$

This leads to a convergence $\kappa(\theta)$ given by

$$\kappa(\theta) \propto \frac{1}{\theta}. \tag{2.26}$$

Inserting this into equation (2.13), we obtain the deflection angle $\alpha = |\vec{\alpha}|$,

$$\alpha(\theta) = const. \tag{2.27}$$

and from equation (2.19), we find

$$\Psi(\theta) \propto \theta. \tag{2.28}$$

A surface density profile like (2.25) is used for the projected density of DM halos in GR and obtained by assuming that the velocity dispersion of the DM particles is spatially constant. Therefore, (2.25) is called an *isothermal* profile. If galactic disks are embedded in such halos, it is also possible to arrive at an admissible explanation for the observed flat rotation curves of spiral galaxies, accepting GR and the concept of DM.

2.2.2 Scalar Contribution

Now that we have gone through the principles of gravitational lensing, we shall adapt the results from GR to the TeVeS framework. From equation (1.48), we know the nonrelativistic total gravitational potential Φ. If we set $\Xi \approx 1$, we simply have

$$\Phi = \Phi_N + \phi. \tag{2.29}$$

As already indicated by equation (2.8), we replace $\Phi_N \to \Phi_N + \phi$ in equation (2.11) and get

$$\vec{\hat{\alpha}} = 2 \int_{-\infty}^{\infty} \vec{\nabla}_\perp (\Phi_N + \phi) dz. \tag{2.30}$$

This integral can be split into a Newtonian (GR) and a scalar contribution:

$$\vec{\hat{\alpha}} = \vec{\hat{\alpha}}_{gr} + 2 \int_{-\infty}^{\infty} \vec{\nabla}_\perp \phi dz = \vec{\hat{\alpha}}_{gr} + \vec{\hat{\alpha}}_s. \tag{2.31}$$

In addition to the deflection angle caused by the Newtonian potential Φ_N, there is a contribution to the deflection potential arising from the scalar field ϕ. Because ϕ is connected to the matter density corresponding to equation (1.69), it is not possible to relate the projected matter density to a two-dimensional scalar deflection potential just like in GR. Unfortunately, there is no way to avoid solving equation (1.69) for calculating the TeVeS deflection angle $\vec{\hat{\alpha}}_s$, which will actually turn out to be a very delicate issue.

2.2.3 Lensing Formalism in TeVeS

In analogy to the GR case, we can introduce dimensionless quantities such as a scaled deflection angle, deflection potential, convergence, etc. by the corresponding definitions from section 2.2.1. If we make use of such a formalism, we have to keep in mind that, for example, the TeVeS convergence κ is not a rescaled projected mass density anymore as it consists of contributions coming from the surface mass density κ_{gr} and the scalar field ϕ which is coupled to the three-dimensional matter density in a highly nonlinear way. Thus, from a GR point of view the lensing

formalism in TeVeS involves quantities that have to be reinterpreted due to the presence of the scalar field. In order to be formally correct, we should speak of pseudo-convergence or pseudo-deflection potential in the TeVeS context. Except for this little problem of interpretation, there are no risks in applying the formalism. Once a quantity like the 2-dimensional potential or the deflection angle has been specified, the formalism provides a closed system which is independent of the particular input, i.e. the lensing formalism just does not know whether we consider an additional scalar potential. If we calculate the deflection angle $\vec{\hat{\alpha}}$ given by equation (2.31), we can safely make use of the formalism and any result we obtain when applying it.

2.3 The Free Functions in Lensing

2.3.1 Reduction

In section 1.2.3, we have shown that for quasistatic systems $0 \leq y(\mu) < \infty$ and

$$\begin{aligned} y(\mu) &\to \infty, \quad \mu \to 1, \\ y(\mu) &\propto \mu^2, \quad \mu \ll 1. \end{aligned}$$

As we have mentioned before, $y(\mu)$ controls the transition from the MONDian to the Newtonian regime where $0 \leq \mu < 1$. Considering lensing in TeVeS, we shall use our simple cosmological model developed in section 1.4.5 B for determining the necessary angular-diameter distances. Since this model is independent of the form of the free function, we can neglect the cosmological branch and concentrate on the range $\mu \in [0, 1[$. Thus, in the nonrelativistic domain, we may focus on a smooth and monotonic free function

$$y(\mu) : I \to W,$$

where $I = [0, 1[$ and $W = [0, \infty[$.

2.3.2 Parameterization

In the last section, we have pointed out that it is appropriate to reduce $y(\mu)$ to a smooth and monotonic function recovering the features from section 1.2.3 with $\mu \in [0, 1[$. If we understand $y(\mu)$ as a complex-valued function

$$y : D \to \mathbb{C},$$

where we have $D \subset \mathbb{R}$, and additionally assume that $y(\mu)$ is analytic, we can introduce $y(z)$, $z \in \mathbb{C}$, as the analytic continuation of $y(\mu)$ into the complex plane. Since $y(z)$ is analytic inside the ring domain $R = \{z \in \mathbb{C} \mid 0 < |z| < 1\}$, it can be expanded into a Laurent series:

$$y(z) = \sum_{n=-\infty}^{\infty} c_n (1 - z)^n. \tag{2.32}$$

Recasting equation (2.32) back to a real-valued function, we obtain

$$y(\mu) = \sum_{n=1}^{\infty} \frac{a_n}{(1 - \mu)^n} + \sum_{n=0}^{\infty} b_n \mu^n, \tag{2.33}$$

with new coefficients a_n, $b_n \in \mathbb{R}$. For $\mu \ll 1$, the above expression yields to second order:

$$y(\mu) \approx \left(b_0 + \sum_{n=1}^{\infty} a_n \right) + \left(b_1 + \sum_{n=1}^{\infty} a_n n \right) \mu + \left(b_2 + \sum_{n=1}^{\infty} a_n \frac{n(n+1)}{2} \right) \mu^2. \tag{2.34}$$

In order to keep the features responsible for the Newtonian and MONDian limits, we must have the following relations for the coefficients a_n, b_n:

$$b_0 + \sum_{n=1}^{\infty} a_n = 0, \tag{2.35}$$

$$b_1 + \sum_{n=1}^{\infty} a_n n = 0, \tag{2.36}$$

$$b_2 + \sum_{n=1}^{\infty} a_n \frac{n(n+1)}{2} \neq 0. \tag{2.37}$$

As a simple example, we take the function $y(\mu) = \mu^2/(1-\mu)$ and find that the non-zero coefficients are given by

$$a_1 = 1, \quad b_0 = -1, \quad b_1 = -1.$$

Setting the coefficients a_n and b_n, we are able to directly control the specific transition behavior from MONDian to Newtonian dynamics, which will be quite helpful when studying the effects of a varying free function $y(\mu)$ on the deflection angle within numerical analysis.

2.4 Analytical Models of Spherical Lenses

One crucial point in examining the properties of TeVeS lens systems is to determine the gradient of the scalar field ϕ in a quasistatic background, which, in general, means to find a corresponding solution of equation (1.42). However, if we consider spherically symmetric systems, for certain choices of the free function $y(\mu)$ and the matter density profile $\tilde{\rho}$, there exist some problems that can be treated analytically. On the one hand, analytical lens models are suitable to investigate general properties of lensing in TeVeS while, on the other hand, they will be useful as a reference when compared to numerical solutions.

2.4.1 Choice of the Free Function

Following Zhao et al. (2006), we switch to a slightly different notation which turns out to be more suitable for analytical studies. Instead of the inverse free function μ, we shall consider the function $\bar{\mu}$ which is given by

$$\frac{\bar{\mu}}{1-\bar{\mu}} = \frac{4\pi}{k}\left(1 - \frac{K}{2}\right)^{-1} \mu, \tag{2.38}$$

where k, K are the coupling constants of the scalar field ϕ and the vector field U_μ, respectively. Similarly, we can relate the free function y to a new function δ_ϕ in the following way:

$$\delta_\phi^2 = \left(\frac{4\pi}{k}\left(1 - \frac{K}{2}\right)\right)^2 \frac{y}{b}, \tag{2.39}$$

where b is the real-valued parameter of the free function $y(\mu)$ from section 1.2.3. Keeping the former choice of $y(\mu)$, a bit of algebra reveals the corresponding equation for $\bar{\mu}$ and δ_ϕ:

$$\delta_\phi^2 = \frac{\bar{\mu}^2}{(1-\bar{\mu})^2}\left[\frac{\left(1 - \frac{k}{8\pi}\left(1 - \frac{K}{2}\right)\frac{\bar{\mu}}{1-\bar{\mu}}\right)^2}{\left(1 - \frac{k}{4\pi}\left(1 - \frac{K}{2}\right)\frac{\bar{\mu}}{1-\bar{\mu}}\right)}\right]. \tag{2.40}$$

Since we have k, $K \ll 1$, this leads to

$$\delta_\phi^2 \approx \frac{\bar{\mu}^2}{(1-\bar{\mu})^2}, \quad \bar{\mu}^2 \approx \frac{\delta_\phi^2}{(1+\delta_\phi)^2}. \tag{2.41}$$

As we shall see, the simple form (2.41) of the free function which is actually pretty close to our original choice enables us to derive analytical expressions for the deflection angle assuming certain spherical mass density profiles like, for instance, that of a point mass.

2.4.2 Acceleration and Deflection Angle

According to equation (1.49), we can express the gradient of the scalar field ϕ in terms of the gradient of the Newtonian potential Φ_N if we restrict ourselves to spherically symmetric systems. Substituting μ by $\bar{\mu}$, we directly see that

$$\vec{\nabla}\phi = \frac{1-\bar{\mu}}{\bar{\mu}}\vec{\nabla}\Phi_N. \tag{2.42}$$

Recalling that $y = kl^2 h^{\mu\nu}\phi_{,\mu}\phi_{,\nu}$ and $l = \sqrt{bk}/(4\pi\Xi a_0)$ (see equation (1.53)), we find that in the nonrelativistic approximation equation (2.39) can be reduced to

$$\delta_\phi^2 = \frac{|\vec{\nabla}\phi|^2}{a_0^2}. \tag{2.43}$$

Since the gradient of the total gravitational potential Φ is

$$\vec{\nabla}\Phi = \vec{\nabla}\Phi_N + \vec{\nabla}\phi, \tag{2.44}$$

it can be shown from equations (2.41) and (2.43) that

$$|\vec{\nabla}\Phi| = |\vec{\nabla}\Phi_N| + \sqrt{a_0|\vec{\nabla}\Phi_N|}. \tag{2.45}$$

Now that we have obtained the gradient of the total potential in terms of the Newtonian potential Φ_N, we are interested in the resulting deflection angle $\hat{\alpha}$. Because of our spherically symmetric situation, it is helpful to express quantities in terms of the radial coordinate r. Using

$$\vec{\nabla}_\perp\Phi(r) = \frac{d\Phi(r)}{dr}\frac{\xi}{r}, \quad r = \sqrt{z^2+\xi^2}, \tag{2.46}$$

where ξ is the impact parameter of a light ray propagating along the z-direction, we may replace equation (2.30) by

$$\hat{\alpha}(\xi) = 4\xi\int_\xi^\infty \left(\frac{d\Phi}{dr}\right)\frac{dr}{\sqrt{r^2-\xi^2}}. \tag{2.47}$$

Thus, choosing (2.41) for the free function, the TeVeS deflection angle for any given Newtonian potential Φ_N reads

$$\hat{\alpha}(\xi) = 4\xi\int_\xi^\infty \left(|\vec{\nabla}\Phi_N| + \sqrt{a_0|\vec{\nabla}\Phi_N|}\right)\frac{dr}{\sqrt{r^2-\xi^2}}. \tag{2.48}$$

2.4.3 The Point Lens

The Newtonian potential of a point mass is given by

$$\Phi_N = -\frac{GM}{r}, \tag{2.49}$$

and therefore we have

$$|\vec{\nabla}\Phi_N| = \frac{GM}{r^2}. \tag{2.50}$$

Inserting the above into equation (2.48) yields

$$\hat{\alpha}(\xi) = 4\xi\int_\xi^\infty \left(\frac{GM}{r^2} + \frac{\sqrt{GMa_0}}{r}\right)\frac{dr}{\sqrt{r^2-\xi^2}}. \tag{2.51}$$

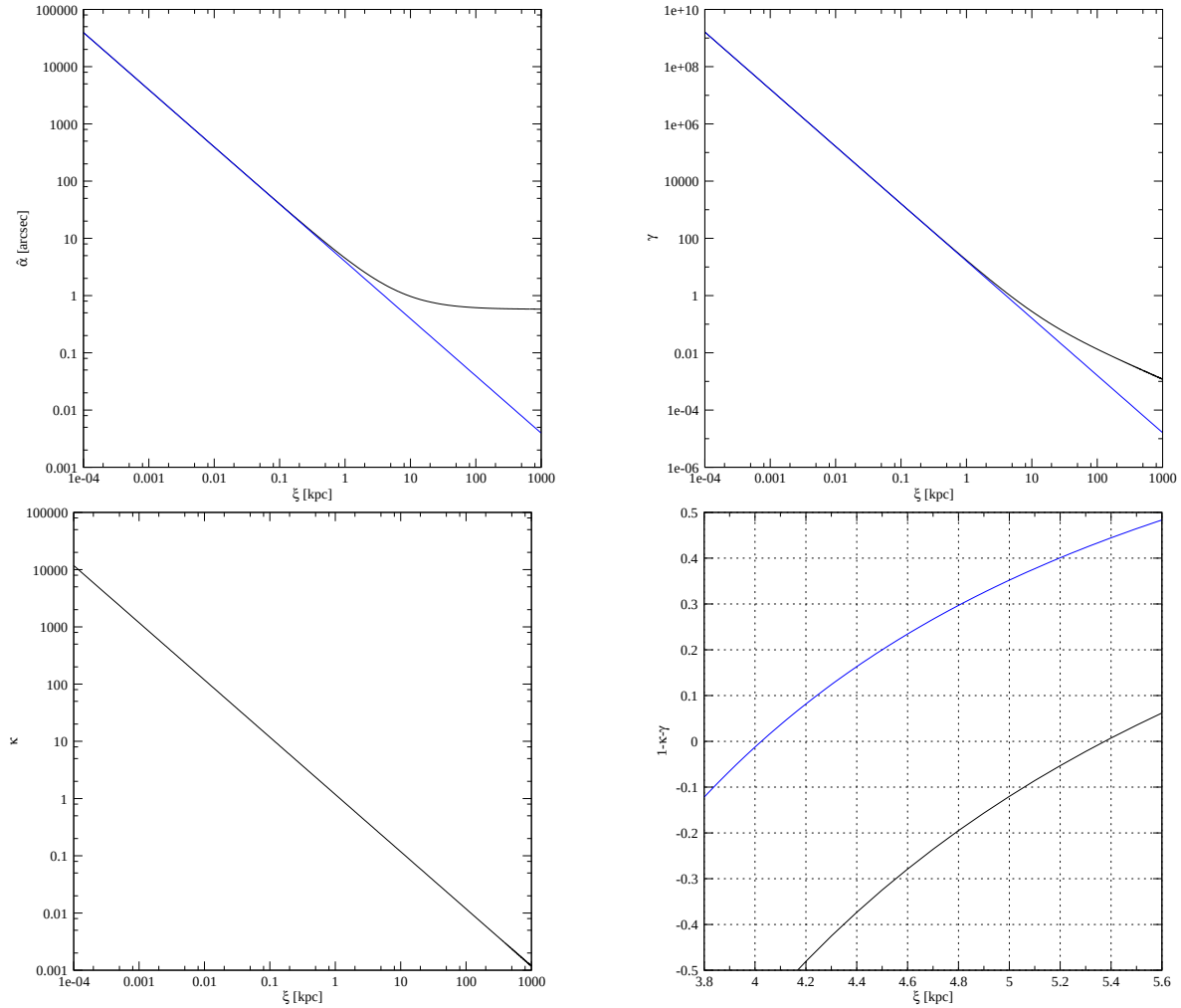

Figure 2.4: The TeVeS point lens (black line) compared to a GR point lens (blue line) with respect to $\hat{\alpha}$ (upper-left), κ (lower-left) and γ (upper-right) for $M = 10^{11} M_{\odot}$, $a_0 = 1 \times 10^{-8} cms^{-2}$ and $D = 850 Mpc$. Far away from the lens, $\hat{\alpha}$ asymptotically approaches the constant angle $\hat{\alpha}_{\infty} = 2\pi\sqrt{GMa_0} \approx 0.58''$. The transition to the MONDian regime can be characterized by the critical radius $r_0 = \sqrt{GM/a_0} \approx 10 kpc$. Lower-right: Since the TeVeS point lens mimics the behavior of a GR isothermal sphere, the tangential critical line is driven outwards, i.e. its radius is larger than the one of a GR point lens.

This integral can be evaluated in closed form and we obtain:

$$\hat{\alpha}(\xi) = \frac{4GM}{\xi} + 2\pi\sqrt{GMa_0}. \tag{2.52}$$

Apart from the well-known Newtonian contribution, there is a constant contribution to the deflection angle due to the scalar field ϕ, i.e. the deflection angle becomes a non-zero constant far away from the lens, $\hat{\alpha}_{\infty} = 2\pi\sqrt{GMa_0}$. In section 2.2.1 F, we also obtained a constant deflection angle when considering the lensing properties of an isothermal sphere. Obviously, the scalar part of TeVeS gravity of a point mass seems to mimic the presence of such a density profile. Therefore, both GR including DM and TeVeS will basically make the same lensing predictions for ξ being much larger than the extension of the lens, but the highly nonlinear coupling of the scalar field strongly suggests that there may be significant differences when moving to the strong acceleration regime.

Using equation (2.52), we can calculate convergence κ and shear γ:

$$\kappa = \pi D \left(4GM\delta_D(\xi) + \frac{\sqrt{GMa_0}}{\xi} \right), \tag{2.53}$$

$$\gamma = D \left(\frac{4GM}{\xi^2} + \frac{\pi\sqrt{GMa_0}}{\xi} \right), \tag{2.54}$$

where δ_D denotes the Dirac delta distribution and $D = D_{ds}D_d/D_s$. According to equation (2.24), critical lines satisfy the relation $1 - \kappa \pm \gamma = 0$. Using the expressions from above, we obtain

$$1 - \kappa - \gamma = 1 - 2D \left(\frac{2GM}{\xi^2} + \frac{\pi\sqrt{GMa_0}}{\xi} \right) \tag{2.55}$$

and

$$1 - \kappa + \gamma = 1 + D\frac{4GM}{\xi^2}. \tag{2.56}$$

Equation (2.56) is just the same as for the GR point lens. As we can see, it is not possible to have $1 - \kappa + \gamma = 0$ for $\xi > 0$, the inner critical curve degenerates to a critical point. But from equation (2.55), we can conclude that there is a tangential critical line with radius

$$\xi_{cr} = \pi\sqrt{GMa_0}D + \sqrt{(\pi D)^2 GMa_0 + 4DGM} > \theta_E D_d, \tag{2.57}$$

where θ_E is the Einstein radius, i.e. $\theta_E D_d$ is the radius of the tangential critical line of a GR point lens, which is given by

$$\theta_E = \left(4GM\frac{D_{ds}}{D_d D_s} \right)^{\frac{1}{2}}. \tag{2.58}$$

Compared to the GR point lens, we notice that the tangential critical line is pushed outwards due to the additional contributions of the scalar field. Of course, this behavior is expected as the TeVeS point lens additionally mimics the GR properties of an isothermal sphere. Figure 2.4 shows the lensing properties of both the TeVeS and the GR point lens where we have set $M = 10^{11}M_\odot$, $a_0 = 1 \times 10^{-8} cms^{-2}$ and $D = 850Mpc$, henceforth using $G = 6.6742 \times 10^{-5} cm^3 kg^{-1} s^{-2}$ for the gravitational constant and $c_{light} = 9.7145 \times 10^{-12} kpcs^{-1}$ for the speed of light.

Furthermore, we can introduce the critical TeVeS radius r_0 as

$$r_0 = \left(\frac{GM}{a_0} \right)^{\frac{1}{2}}. \tag{2.59}$$

Keeping the settings from Figure (2.4), it follows that $r_0 \approx 10kpc$. Referring to the deflection angle, we observe that the critical radius r_0 is a length scale characterizing the transition zone from Newtonian to MONDian dynamics. This quantity will be helpful when estimating scales of significant MONDian influence.

2.4.4 The Hernquist Lens

Having dealt with a point lens, we shall now investigate an extended lens characterized by a Hernquist profile (Hernquist, 1990):

$$\rho(r) = \frac{Mr_H}{2\pi r(r + r_H)^3}, \tag{2.60}$$

the Hernquist radius r_H being the core scale length and M the total mass. The Hernquist profile closely approximates the de Vaucouleurs $R^{1/4}$-law for elliptical galaxies, and its lensing properties should be more accurate than those of a simple point mass when modeling such galaxies.

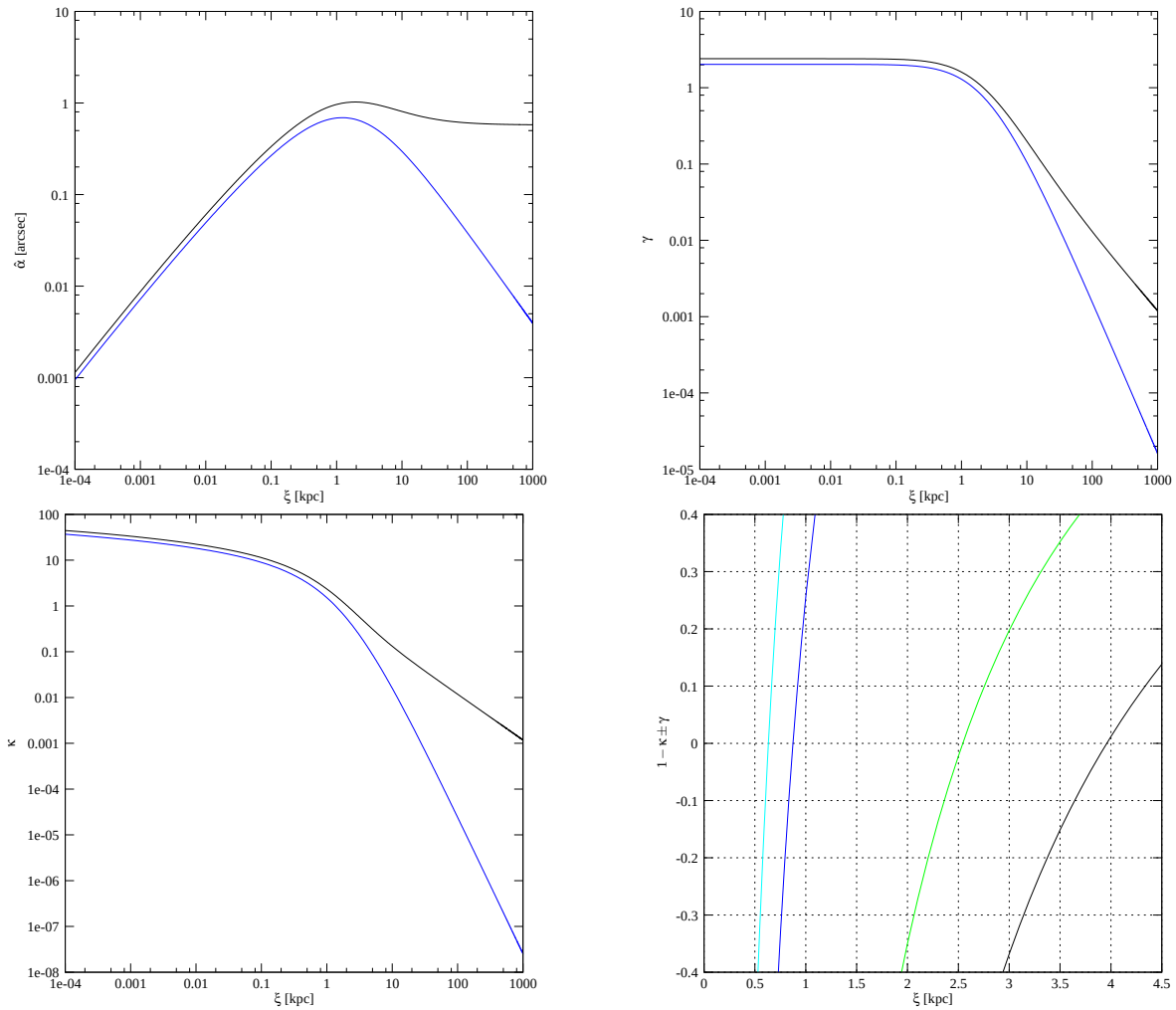

Figure 2.5: The lens properties of a Hernquist lens both in TeVeS (black) and GR (blue): $\hat{\alpha}$ (upper-left), κ (lower-left) and γ (upper-right) are shown for a galaxy with $M = 10^{11} M_\odot$ and $r_H = 2kpc$ ($a_0 = 1 \times 10^{-8} cms^{-2}$, $D = 850Mpc$). The transition to the MONDian regime becomes visible around the critical radius $r_0 \approx 10kpc$. Lower-right: Due to its finite extent, the Hernquist lens has *two* critical curves, a tangential one (TeVeS: black, GR: green) at $\xi_{cr,t} \approx 3.95kpc$ and a radial one (TeVeS: blue, GR: cyan) at $\xi_{cr,r} \approx 0.9kpc$. Since the scalar field contributes additional energy density similar to the situation of a TeVeS point lens, the critical lines are driven outwards compared to the GR case.

Integrating the above matter density over a sphere with radius R, we get the following:

$$M(R) = \frac{R^2}{(R + r_H)^2} M. \tag{2.61}$$

In this situation, the gradient of the Newtonian potential Φ_N reads

$$|\vec{\nabla}\Phi_N| = \frac{GM(r)}{r^2} = \frac{GM}{(r + r_H)^2}, \tag{2.62}$$

which leads to the gradient of the total gravitational potential Φ,

$$|\vec{\nabla}\Phi| = \frac{GM}{(r + r_H)^2} + \frac{\sqrt{GMa_0}}{(r + r_H)}. \tag{2.63}$$

In analogy to the case of the point lens, we therefore obtain the deflection angle $\hat{\alpha}$ as

$$\hat{\alpha}(\xi) = 4\xi \int_\xi^\infty \left(\frac{GM}{(r + r_H)^2} + \frac{\sqrt{GMa_0}}{(r + r_H)} \right) \frac{dr}{\sqrt{r^2 - \xi^2}}. \tag{2.64}$$

Again, it is possible to evaluate this integral analytically and we finally come up with

$$\hat{\alpha}(\xi) = \begin{cases} \dfrac{r_H \operatorname{arsinh}\sqrt{\left|1-(r_H/\xi)^2\right|}}{\sqrt{|\xi^2 - r_H^2|}} \left(4\xi\sqrt{GMa_0} + \dfrac{4GM\xi}{|\xi^2 - r_H^2|}\right) - \dfrac{4GM\xi}{|\xi^2 - r_H^2|} & \xi < r_H \\ \dfrac{r_H \arcsin\sqrt{1-(r_H/\xi)^2}}{\sqrt{\xi^2 - r_H^2}} \left(4\xi\sqrt{GMa_0} - \dfrac{4GM\xi}{\xi^2 - r_H^2}\right) + \dfrac{4GM\xi}{\xi^2 - r_H^2} & \xi > r_H \end{cases} . \quad (2.65)$$

Of course, we are able to derive the equations for κ and γ using our result for the deflection angle $\hat{\alpha}(\xi)$ and the formalism from section 2.2.1 C. Nevertheless, we drop the corresponding expressions at this point because they are simply too long. Figure 2.5 illustrates the lensing properties of both a TeVeS and a GR Hernquist lens assuming a galaxy mass of $M = 10^{11} M_\odot$ and a core radius $r_H = 2kpc$, keeping the parameters $a_0 = 1 \times 10^{-8} cms^{-2}$ and $D = 850Mpc$. Starting in the center of the TeVeS lens, the deflection angle increases from zero reaching a maximum at $\xi \approx 1.9kpc$ and decreasing again converging to a constant angle at infinity which is given by $\hat{\alpha}_\infty = 2\pi\sqrt{GMa_0} \approx 0.58''$. As we have already pointed out in the context of the TeVeS point lens, the transition to MONDian dynamics becomes noticeable around the critical radius $r_0 \approx 10kpc$.

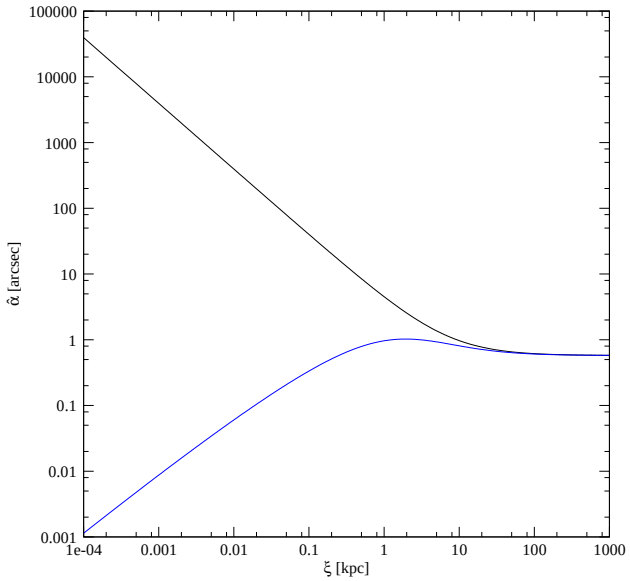

Figure 2.6: Comparison of the TeVeS deflection angle caused by a point mass (black line) and a Hernquist profile (blue line) using the parameters of sections 2.4.3 and 2.4.4. The two lines approximately merge for $\xi \gtrsim 30kpc$.

Since we are dealing with an extended lens, i.e. the corresponding plot of the GR convergence is broadened and not given by a Delta distribution anymore, the same transition characteristic can now also be observed for κ. Compared to the point lens from section 2.4.3, we notice the occurrence of a *second* critical curve, the radial one, which is another feature of the lens's extent. From the lower-right panel of Figure 2.5, we can read off the radii of the tangential and the radial critical curves as $\xi_{cr,t} \approx 3.95kpc$ and $\xi_{cr,r} \approx 0.9kpc$, respectively. Again, the critical lines are shifted outwards compared to those of a GR Hernquist lens without involving any DM. In general, this can be understood by returning to equation (1.69). Solving for the Laplace term, we may now interpret (1.69) as Poisson's equation. In this point of view, the scalar field itself acts as an additional energy density contribution to the original baryonic source that, as we have seen, eventually coincides with the contribution of an isothermal density profile to the Newtonian source in GR far away from the lens. Thus, the effective quantities for convergence and shear as well as the position of the critical lines are changed to what we find in Figure 2.5. Let us define ξ_p as the radius where a TeVeS lens starts to behave point-like. As we can see from Figure 2.6 showing both the point and the Hernquist lens, we have $\xi_p \approx 30kpc$ for our choice of parameters. This radius will play an important role when applying the point lens approximation within the numerical treatment of nonspherical lens systems. Since its deflection angle can be expressed analytically, the Hernquist lens is a perfectly suitable candidate for testing an algorithm for nonspherical problems.

2.5 Moving Lenses

So far we have just considered lens systems whose peculiar velocity v can virtually be neglected, i.e. $v \ll 1$. Within this section, we shall have a look at the lensing properties of a TeVeS lens moving with arbitrary velocity v, and draw a comparison to the results we already know from GR. Following Wucknitz & Sperhake (2004), we keep the assumptions from section 2.1.1, but now we allow for velocities $0 \leq v < 1$.

2.5.1 Radial Motion

Starting in the rest frame of the lens (denoted by a prime), we will transform the necessary quantities to the observer's frame using a Lorentz transform and derive the corresponding deflection angle. According to the weak-field approximation, the line element in the rest frame of the lens is of the following form ($\Xi \approx 1$):

$$ds^2 = g'_{tt}dt'^2 + g'_{ss}(dy'^2 + dz'^2), \tag{2.66}$$

where y' combines the coordinates perpendicular to z' and

$$g'_{tt} = -1 - 2\Phi_N, \quad g'_{ss} = 1 - 2\Phi_N. \tag{2.67}$$

Additionally, we have the scalar field ϕ' and the vector field U'_μ which is given by

$$U'_\mu = \sqrt{-g'_{00}}\delta^\mu_t. \tag{2.68}$$

This is due to the fact that U'_μ has no spatial components for quasistatic systems (see section 1.2.2 E),

$$U'_\mu = N\delta^\mu_t,$$

and that it is normalized with respect to $g'_{\mu\nu}$ according to equation (1.6). Applying the Lorentz transform

$$\begin{aligned} dt' &= \gamma(dt - vdz), \\ dy' &= dy, \\ dz' &= \gamma(dz - vdt), \\ \gamma &= \frac{1}{\sqrt{1-v^2}}, \end{aligned} \tag{2.69}$$

the non-zero components of the Einstein metric $g_{\mu\nu}$ in the observer's frame read

$$\begin{aligned} g_{tt} &= \gamma^2 g'_{tt} + \gamma^2 v^2 g'_{ss}, \\ g_{yy} &= g'_{ss}, \\ g_{zz} &= \gamma^2 g'_{ss} + \gamma^2 v^2 g'_{tt}, \\ g_{tz} &= g_{zt} = -\gamma^2 v g'_{tt} - \gamma^2 v g'_{ss}. \end{aligned} \tag{2.70}$$

While we have $\phi' = \phi$ for the scalar field, the transformation of the vector field U'_μ leads to

$$U_\mu = \sqrt{-g'_{00}}(\gamma\delta^\mu_t - \gamma v\delta^\mu_z). \tag{2.71}$$

Thus, making use of equation (1.7), we are able to calculate the physical metric $\tilde{g}_{\mu\nu}$ which is given by

$$\begin{aligned} \tilde{g}_{tt} &= e^{-2\phi}\gamma^2 v^2 g'_{ss} + e^{2\phi}\gamma^2 g'_{tt}, \\ \tilde{g}_{yy} &= e^{-2\phi} g'_{yy}, \\ \tilde{g}_{zz} &= e^{-2\phi}\gamma^2 g'_{ss} + e^{2\phi}\gamma^2 v^2 g'_{tt}, \\ \tilde{g}_{tz} &= \tilde{g}_{zt} = -e^{-2\phi}\gamma^2 v g'_{ss} - e^{2\phi}\gamma^2 v g'_{tt}, \end{aligned} \tag{2.72}$$

where all other components are equal to zero. Since $\phi, \Phi_N \ll 1$, we obtain the following first-order expression for the physical line element in the observer's frame as

$$\begin{aligned} d\tilde{s}^2 = &- \left[1 + 2\gamma^2(1+v^2)\Phi\right] dt^2 + (1 - 2\Phi)dy^2 \\ &+ \left[1 - 2\gamma^2(1+v^2)\Phi\right] dz^2 + 8\gamma^2 v\Phi dt dz, \end{aligned} \tag{2.73}$$

where $\Phi = \Phi_N + \phi$. Assuming small angles and light propagation close to the z-axis, the deflection angle can be written as

$$\hat{\alpha} = \int_{-\infty}^{+\infty} \frac{d^2y}{dz^2} dz = \gamma^{-1} \int_{-\infty}^{+\infty} \left(1 - v\frac{dt}{dz}\right)^{-1} \frac{d^2y}{dz^2} dz', \tag{2.74}$$

where we have used (2.69). As the geodesic equation is equivalent to an Euler-Lagrange system with Lagrange function

$$L = \left(\frac{ds}{d\lambda}\right)^2, \tag{2.75}$$

the equation of motion for y becomes

$$\frac{d}{d\lambda}\frac{\partial L}{\partial \dot{y}} - \frac{\partial L}{\partial y} = 0, \tag{2.76}$$

where the derivative with respect to the parameter λ is denoted by a dot, i.e. $dA/d\lambda = \dot{A}$. Setting $\lambda = z$ and neglecting higher-order deflection terms like $\Phi\ddot{y}$, $\dot{\Phi}\dot{y}$ and $\dot{y}^2$, we find

$$\frac{d^2y}{dz^2} = -\gamma^2 \left[(1+v^2)\left(\left(\frac{dt}{dz}\right)^2 + 1\right) - 4v\frac{dt}{dz}\right] \Phi_{,y}. \tag{2.77}$$

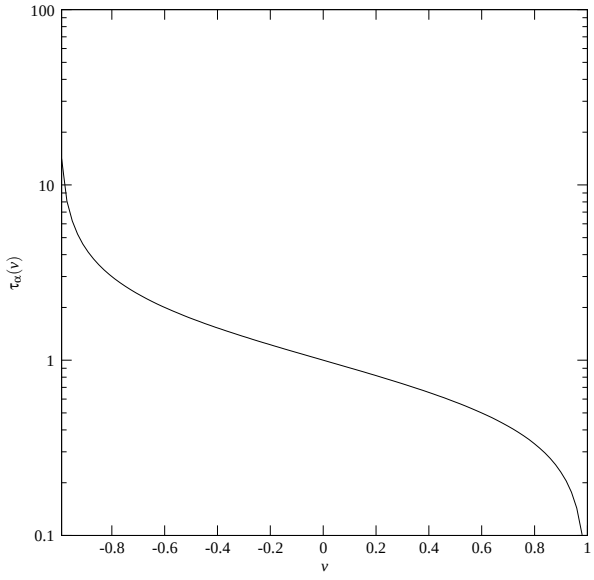

Figure 2.7: The scaling factor $\tau_\alpha(v)$ of a radially moving lens: If the lens is moving towards an observer ($v > 0$), $\tau_\alpha(v)$ decreases and eventually becomes zero for $v \to +1$. If the lens is moving away from an observer ($v < 0$), $\tau_\alpha(v)$ increases and diverges as $v \to -1$.

Integrating along the unperturbed light path, we may set $dt \approx dz$, and since $\Phi_{,y} = \Phi_{,y'}$, we finally obtain

$$\hat{\alpha}(v) = \tau_\alpha(v)\hat{\alpha}(0), \tag{2.78}$$

$$\tau_\alpha(v) = \sqrt{\frac{1-v}{1+v}}, \tag{2.79}$$

$\hat{\alpha}(0)$ being the deflection angle in the static case, i.e. $v = 0$, which is given by

$$\begin{aligned} \hat{\alpha}(0) &= -2\int_{-\infty}^{+\infty} (\Phi_{N,y'} + \phi_{,y'}) dz' \\ &= \hat{\alpha}_{gr}(0) + \hat{\alpha}_s(0). \end{aligned} \tag{2.80}$$

The deflection angle of a radially moving lens is given by the static deflection angle rescaled by an overall scaling factor $\tau_\alpha(v)$, which is identical to the result found in GR. Starting from $\tau_\alpha(0) = 1$, the scale factor decreases if the lens is moving towards an observer ($v > 0$), and eventually becomes zero for $v \to +1$. If the lens is moving away from an observer ($v < 0$), the scale factor increases and diverges as $v \to -1$. For example, choosing $v = -0.1$, we approximately find that the scale factor is given by $\tau_\alpha = 1.1$. Since the total deflection angle is enlarged in that case, differences between the deflection angles of TeVeS and GR including DM might become more accessible to observations considering such moving lens systems.

2.5.2 Tangential Motion

A. Deflection Angle

Analog to the case of radial motion, we can investigate the properties of a TeVeS lens moving perpendicular to the line of sight. For this purpose, let us substitute the Lorentz transform (2.69) by the following one:

$$\begin{aligned} dt^{'} &= \gamma(dt - vdz), \\ dy^{'} &= \gamma(dy - vdt), \\ dz^{'} &= dz. \end{aligned} \tag{2.81}$$

Thus, the physical line element in the observer's frame becomes

$$\begin{aligned} d\tilde{s}^2 = &- \left[1 + 2\gamma^2(1+v^2)\Phi\right] dt^2 + (1 - 2\Phi)dz^2 \\ &+ \left[1 - 2\gamma^2(1+v^2)\Phi\right] dy^2 + 8\gamma^2 v\Phi dtdy, \end{aligned} \tag{2.82}$$

where we have used the total gravitational potential Φ from equation (2.73). Calculating the corresponding Lagrange function (2.75) and inserting it into (2.76), we are able to derive the following equations of motion:

$$\begin{aligned} &\frac{d^2y}{dz^2} + 4\gamma^2 v\left(\Phi\frac{d^2t}{dz^2} - \gamma v\Phi_{,y'}\left(\frac{dt}{dz}\right)^2 + \Phi_{,z'}\frac{dt}{dz}\right) \\ &\quad = -\gamma\Phi_{,y'}\left((1+v^2)\gamma^2\left(\frac{dt}{dz}\right)^2 + 1\right), \\ &\frac{d^2t}{dz^2} + 2(1+v^2)\gamma^2\left(\Phi\frac{d^2t}{dz^2} - \gamma v\Phi_{,y'}\left(\frac{dt}{dz}\right)^2 + \Phi_{,z'}\frac{dt}{dz}\right) \\ &\quad = -\gamma v\Phi_{,y'}\left((1+v^2)\gamma^2\left(\frac{dt}{dz}\right)^2 + 1\right), \end{aligned} \tag{2.83}$$

where we have again neglected higher-order deflection terms and incorporated the relations

$$\Phi_{,y} = \gamma\Phi_{,y'}, \quad \Phi_{,t} = -\gamma v\Phi_{,y'}. \tag{2.84}$$

Substituting $\Phi \to \Phi_N$, (2.83) also coincides with the outcome in GR. The geodesic equations (2.83) are coupled to each other and contain additional terms involving the radial derivate $\Phi_{,z'}$ because aberration causes the direction of light propagation in the lens's rest frame to depend on the velocity v. As $\Phi_{,z'} = \Phi_{N,z'} + \phi_{,z'}$, any changes to the deflection angle resulting from $\Phi_{,z'}$ could be helpful to distinguish between laws of gravity since $\phi_{,z'}$ is nonlinearly coupled to baryonic matter in TeVeS . However, this effect turns out to be extremely small, thus becoming completely negligible referring to today's observational methods. Assuming $v \ll 1$ and integrating along the unperturbed light path, we obtain the deflection angle as

$$\hat{\alpha}(v) = \hat{\alpha}(0) + \mathcal{O}(v^2), \tag{2.85}$$

where $\hat{\alpha}(0)$ is given by equation (2.80). Apparently, there is no modification of the deflection angle at all to first order in velocity. Therefore, it is basically impossible to measure deviations in the deflection angle of a tangentially moving lens, being merely of theoretical interest.

B. Redshift

Considering a tangentially moving lens, there is another effect to be taken into account. Due to the lens's motion, a photon passing the lens will experience a change in energy. According to Wucknitz & Sperhake, the photon's relative change in momentum is given by

$$\frac{\Delta p}{p} = \alpha v_\perp, \tag{2.86}$$

where $v_\perp$ denotes the lens's transversal velocity and $\alpha \approx \alpha(0)$ is the deflection angle. Since the photon's change in momentum corresponds to a frequency shift, equation (2.86) can be expressed in terms of an additional redshift Δz:

$$\Delta z = -\alpha v_\perp. \tag{2.87}$$

If the lens has an additional radial velocity component $v_\parallel$, it can be shown that equation (2.87) has to be replaced by

$$\Delta z = -\alpha \frac{v_\perp}{1 - v_\parallel}. \tag{2.88}$$

From a theoretical point of view, this relation implies different redshifts due to different angles in TeVeS or GR with DM:

$$\delta(\Delta z) = \left| (\alpha_{gr,dm} - \alpha_s) \frac{v_\perp}{1 - v_\parallel} \right|. \tag{2.89}$$

Unfortunately, we have $\alpha,\ v_\perp,\ v_\parallel \ll 1$, and thus the resulting effects will again become completely negligible for any measurements.

In summary, we see that the effects of moving lenses in TeVeS are identical to those in GR substituting $\Phi = \Phi_N + \phi \to \Phi_N$. Although theory predicts differences between the deflection angles in TeVeS and GR, it will basically be impossible to find them applying today's observational methods because the peculiar velocity v and the angle $\hat{\alpha}$ are generally small quantities. Therefore, we shall restrict any further investigation to the static case, i.e. $v = 0$.

3 Numerical Lens Models in TeVeS

In the following sections, we will examine the properties of more general lens systems using numerical methods. Starting with an analysis of different choices for the free function for spherically symmetric systems, we move on by presenting an algorithm for the treatment of nonspherical lenses in TeVeS. After a detailed discussion including limitations and problems related to this method, we continue investigating lensing for a set of different matter distributions ending the chapter with a toy model of the cluster merger 1E0657 − 558 ("bullet cluster").

3.1 Spherical Lenses

3.1.1 Comparison to the Analytical Solution

Assuming spherically symmetric systems, the gradient of the scalar field ϕ is connected to the Newtonian potential Φ_N according to equation (1.49) (see section 1.3.2). If we choose a suitable free function $y(\mu)$ and limit ourselves to the Newtonian potentials of a point and a Hernquist lens given by equation (2.49) and

$$\Phi_{N,Hern} = -\frac{GM}{r + r_H}, \tag{3.1}$$

respectively, we simply need to numerically invert the free function $y(\mu)$, calculate $\vec{\nabla}\phi$ and make use of equation (2.30) to obtain the TeVeS deflection angle. Starting with the simple choice

$$\begin{aligned} y(\mu) = \frac{\mu^2}{1-\mu}, \quad a_1 = 1, \\ b_0 = -1, \quad b_1 = -1, \end{aligned} \tag{3.2}$$

from section 2.3.2, we can compare the obtained numerical result to our analytical solution derived in section 2.4.1 which involves a free function $y(\mu)$ that is quite close to Bekenstein's choice. Figure 3.1 shows the absolute difference between the TeVeS deflection angles of the analytical and the numerical Hernquist lens using the parameters from section 2.4.4, where we have set $k = 0.01$ for the numerical calculation. Although we have considered two different free functions $y(\mu)$, the actual difference in the deflection angle is fairly small, $\Delta\hat{\alpha} \sim (10^{-5})''$, and thus negligible with respect to the observational resolution limit. In spite of its rather unrealistic mass distribution, we can analogously draw a similar conclusion for the point lens, which is illustrated in Figure 3.2. We find that $\Delta\hat{\alpha} \lesssim (10^{-4})''$ for $\xi \gtrsim 1kpc$ while the absolute difference increases for smaller values of the impact parameter. At first glance, this may actually seem

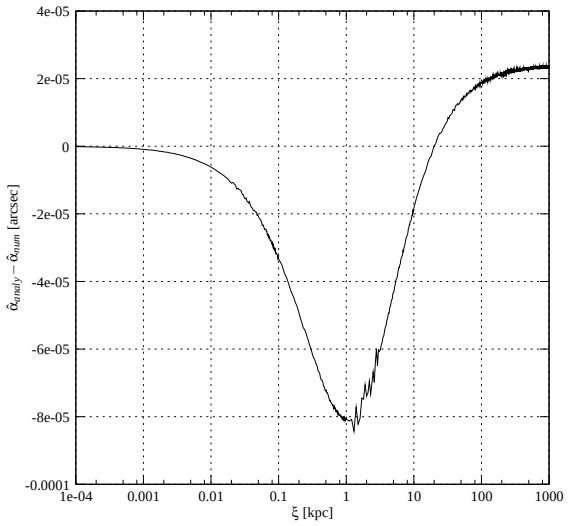

Figure 3.1: Difference between the TeVeS deflection angles of the analytical and the numerical Hernquist lens choosing the parameters from section 2.4.4: Clearly, the deviations are beyond observational resolution, $\Delta\hat{\alpha} \sim (10^{-5})''$. For the numerical calculation, we have assumed $k = 0.01$ and $y(\mu) = \mu^2/(1-\mu)$.

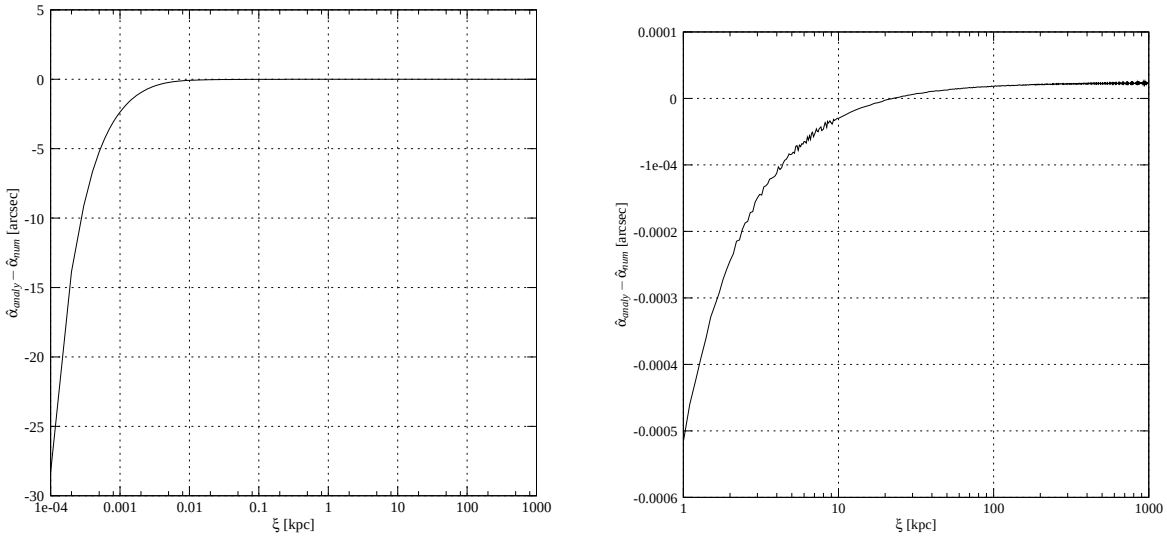

Figure 3.2: Difference between the TeVeS deflection angles of the analytical and the numerical point lens choosing the parameters from section 2.4.3: The right plot shows part of the left one, starting at $\xi = 1kpc$. As we can see, the deviations are beyond observational resolution for $\xi \gtrsim 1kpc$, $\Delta\hat{\alpha} \sim (10^{-4})''$, while diverging for $\xi \to 0$. For the numerical calculation, we have assumed $k = 0.01$ and $y(\mu) = \mu^2/(1-\mu)$.

baffling, but having a look at Figure 2.4, we find that the relative difference in this area is approximately a constant given by $\Delta\hat{\alpha}/\hat{\alpha}_{analy} \sim 10^{-4}$. If we recall that the Newtonian limit in TeVeS implies a renormalized gravitational constant, it is no surprise to encounter this behavior in the strong acceleration regime of the point lens. Returning to equation (1.58), we realize that the observed relative difference is a result of comparing deflection angles which depend on two different free functions *including different couplings of the scalar field* ϕ. From this point of view, the deviation between the deflection angles of the point lens may still be regarded as small.

Considering the above, it appears that we could be able to determine classes of free functions $y(\mu)$ that produce almost the same deflection angle. However, we do expect a large number of such classes causing different lensing properties for identical mass distributions. To gain a better insight, we shall use a more systematic approach to investigating the effects of a varying free function and different choices of k within the next section.

3.1.2 Influence of the Free Function

In the following, we shall consider lensing by a point source only, focusing on a varying form of the free function $y(\mu)$ and the coupling constant k. If not specified in any other way, we will keep the choice of the parameter set from section 2.4.3 using (3.2) and $k = 0.01$ as a reference for the comparison of deflection angles throughout this section.

A. Varying the Parameters a_n and k

Using the notation introduced in section 2.3.2, we take the free function (3.2) and begin with a variation of the constants a_n where we have to adjust b_0, b_1 and b_2 according to equations (2.35), (2.36) and (2.37), setting k to a fixed value, $k = 0.01$. Interestingly, numerical analysis has shown that there are no significant changes to the deflection angle for a wide set of parameters, i.e. the relative changes are comparable to those we found in the last section, $\Delta\hat{\alpha}_{rel} \lesssim 10^{-5} - 10^{-4}$. For instance, if we choose

$$\begin{aligned} a_{18} = 1, \quad a_{19} = -2, \quad a_{20} = 1, \\ b_0 = 0, \quad b_1 = 0, \quad b_2 = 0, \end{aligned} \tag{3.3}$$

which is the expansion of

$$y(\mu) = \frac{\mu^2}{(1-\mu)^{20}}, \tag{3.4}$$

the relative deviation is of $\mathcal{O}(10^{-5})$. As we have seen, the singularity at $\mu = 1$ recovers the Newtonian limit in quasistatic situations, but remarkably, the transition behavior which is directly connected to the deflection angle seems almost insensitive to the particular choice of the realization. Similarly, we can also examine the effect of a changing coupling constant k taking the coefficients a_n, b_n as constants. Again, the relative differences turn out to be very small, $\Delta\hat{\alpha}_{rel} \lesssim 10^{-5} - 10^{-4}$, varying k within the range of $10^{-4} - 10^{-2}$ for different sets of a_n, b_n. Obviously, as long as it is small, $k \lesssim 0.01$, the calculation of the deflection angle does not really depend on the exact value of k, which is in accordance with the results of section 3.1.1.

Apart from any representation of $y(\mu)$ including an infinite amount of coefficients, we strongly emphasize that we cannot exclude the existence of any set of a_n and k leading to a significant change in the deflection angle, which is due to the huge variety of possible choices.

B. Steep Transition

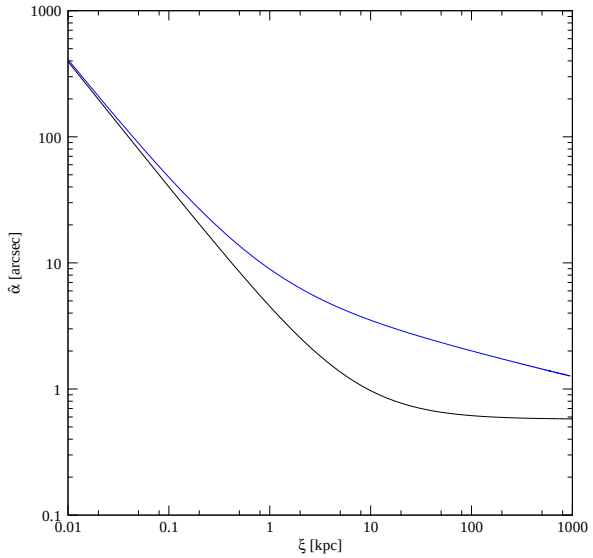

Figure 3.3: Comparison between the point lens's deflection angle for the standard ($y = \mu^2/(1-\mu)$, black) and the steep ($y = \mu^2 + x\mu^3 + y\mu^4/(1-\mu)$, blue) choice of the free function, setting $k = 0.01$, $x = 10^7$ and $y = 10^9$. The steep function stretches the intermediate regime causing the MONDian limit to be approached further away from the center of the lens.

Up to this point, we still lack an investigation of the coefficients b_n. While b_0, b_1 and b_2 are bound to the a_n, there is great freedom for the remaining b_n. Choosing the values of the b_n ($n > 2$) up to an order of $10^2 - 10^3$, we basically obtain the same result as found for the variation of the a_n. Since we have $0 < \mu < 1$, higher-order coefficients will negligibly contribute to the effective transition described by $y(\mu)$. Therefore, it may be interesting to artificially create a steep transition by setting the corresponding coefficients to very high values. For example, let us consider a free function given by

$$\begin{aligned} a_1 &= 1 + x + y, \\ b_0 &= -(1 + x + y), \\ b_1 &= -(1 + x + y), \\ b_2 &= -(x + y), \quad b_3 = -y, \end{aligned} \tag{3.5}$$

which corresponds to the following form of $y(\mu)$:

$$y(\mu) = \frac{\mu^2 + x\mu^3 + y\mu^4}{1-\mu}, \tag{3.6}$$

where $x, y \in \mathbb{R}$. If we set $x = 10^7$ and $y = 10^9$, the transition's "steepness" becomes visible in terms of the deflection angle. Figure 3.3 shows the lens's deflection angles for both the standard choice (3.2) and (3.6). The steep function has the effect of spatially stretching the intermediate section by increasing the deflection angle there, which causes the MONDian regime to be driven away from the center of the lens. Since the relative deviations are of $\mathcal{O}(1)$, they have to be considered as significant, attesting a possibly strong influence of the choice of $y(\mu)$ on the physical results.

C. Physical Gap and Flat Rotation Curves

Let us return to Bekenstein's choice of the free function (see section 1.2.3). As we have previously mentioned, quasistatic situations are described by $0 \leq \mu < 1$ while cosmology needs $2 < \mu < \infty$. For $1 < \mu < 2$, there is apparently some sort of gap separating the two sectors from each other. Because of this detachment implying the lack of a smooth transition between galaxies and cosmology, one might actually consider a free function like this to be rather unphysical. Additionally, recent analysis has shown that this specific free function leads to poor fits of measured rotation curves and does not reproduce the successes of empirical MOND interpolating functions $\tilde{\mu}(x)$ (see section 1.1) like, for example, the standard form

$$\tilde{\mu}(x) = \frac{x}{\sqrt{1+x^2}} \tag{3.7}$$

or the form

$$\tilde{\mu}(x) = \frac{x}{1+x} \tag{3.8}$$

(Famaey & Binney, 2005). For this reason, Zhao & Famaey (2006) have proposed a new free function which is given by

$$s \equiv \frac{g_s}{a_0} = \sqrt{\frac{|y|}{bk'^2}} = \frac{\mu}{(k'+\mu)(1-\mu)}, \tag{3.9}$$

where b is the real parameter from section 1.2.3, $k' = k/4\pi$ and g_s denotes the acceleration due to the scalar field. For quasistatic systems, equation (3.9) can be expressed as follows ($y > 0$):

$$y(\mu) = \frac{b\mu^2}{\left(1+\frac{4\pi}{k}\mu\right)^2 (1-\mu)^2}, \tag{3.10}$$

with the condition $0 \leq \mu < 1$. If $\mu \ll 1$ ($\mu \sim k$), equation (3.10) reduces to

$$s \approx \frac{\mu_s}{1+\mu_s}, \tag{3.11}$$

where we have introduced $\mu_s = \mu/k'$. Since the point lens is a spherically symmetric system, we can derive the following relation:

$$\mu_s = \frac{\tilde{\mu}}{1-\tilde{\mu}}. \tag{3.12}$$

Thus, the choice (3.9) is consistent with rotation curves since it reduces to the simple interpolating function (3.8).

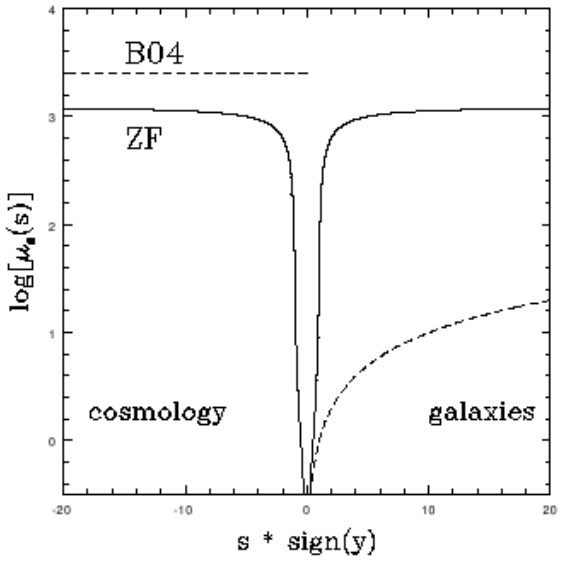

Figure 3.4: The newly proposed function $\mu_s(s)$ (ZF) compared to Bekenstein's choice (B04) for $b = 3$: The cosmological regime $y < 0$ is obtained by mirror-imaging (Zhao & Famaey, 2006).

As already implied by equation (3.9), the cosmological branch of the free function is obtained by a simple mirror-imaging of the quasistatic regime into the $y < 0$ regime at $y = 0$, thus closing the gap between the two sectors. Figure 3.4 illustrates the function $\mu_s(s)$ for both Bekenstein's choice of the free function and (3.9) which connects the cosmological regime to galaxies. Zhao & Famaey also point out that any positive continuous function $\mu(y)$ satisfying

$$\mu(-0) = \mu(+0) \sim 0 \tag{3.13}$$

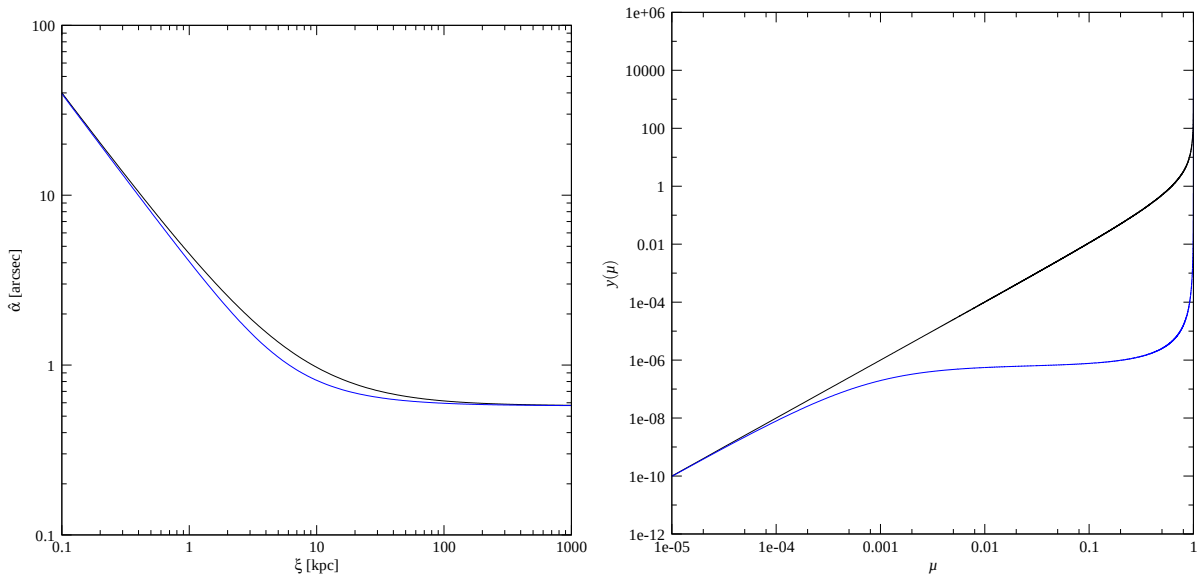

Figure 3.5: Comparison between the standard choice $y(\mu) = \mu^2/(1-\mu)$ (black) and the newly proposed function $y(\mu) = \mu^2/((1-\mu)^2(1+\mu/k^{'})^2)$ (blue): The left panel presents the corresponding deflection angles of the point lens assuming the parameter set from section 2.4.3 and $k = 0.01$. The right panel shows a direct comparison of both the free functions, with $y(\mu) = \mu^2/((1-\mu)^2(1+\mu/k^{'})^2)$ increasing more slowly from the MONDian to the Newtonian limit.

is worth exploring because galaxies and cosmology are connected in the same way in this case. Of course, these choices are required to produce a consistent and realistic cosmology, which is actually possible as recent work has shown (Zhao, 2006). Anyhow, as previously stated, we will make use of our simple cosmological model introduced in section 1.4.5 for all numerical calculations. Therefore, we shall drop the cosmological branch of (3.9) and concentrate on the quasistatic one, i.e. equation (3.10). From Figure 3.5, we see that the function (3.9) increases more slowly with respect to μ when compared to the standard choice (3.2), which results in a slight difference between the corresponding deflection angles of the point lens. In the intermediate regime, we find the relative difference to be of $\mathcal{O}(10^{-1})$. Although the calculated deviation may become significant for quantitative measurement, we remark that the overall qualitative behavior is pretty much the same.

Of course, it is possible to apply the same examination (subsections A,B,C) to a Hernquist lens. However, we will not include the corresponding results at this point since they basically coincide with those of the point lens. Summarizing the above results, we conclude that the choice of the free function $y(\mu)$ (more precisely, the choice of the b_n) can significantly influence the resulting TeVeS deflection angle. On the contrary, as long as it is small, the coupling constant k appears to have an almost negligible effect. In spite of the free function's overall impact, we notice that small variations of $y(\mu)$ only seem to cause small changes in the deflection angle when considering spherically symmetric systems. In general, $y(\mu)$ has to be constrained by observations referring to the rotation curves of galaxies or lensing maps that are independent of the particular law of gravity. Concerning its $y < 0$ regime, one has to consider measurements of cosmologically related quantities like, for instance, the Hubble constant.

D. Choice of $y(\mu)$ for Nonspherical Problems

So far, we have only considered the influence of the free function $y(\mu)$ and k on a spherically symmetric system, i.e. the point lens. Moving to nonspherical lenses, we must not assume the results of the last sections to be true there. Such systems allow for the gradients of the

Newtonian potential Φ_N and the scalar field ϕ to point in different directions, thus complicating the situation enormously. From a physical point of view, however, we expect the situation to be quite similar to that of a spherically symmetric system, but strictly spoken, equation (1.69) represents a different partial differential equation for each specific choice of the function $y(\mu)$ and k, and we emphasize that it is completely unclear how small variations of those quantities might affect a possible solution for ϕ. Nevertheless, we have to start at some point, and therefore we shall limit our investigations of nonspherical lenses to a single choice of the free function $y(\mu)$ and k which will be presented in the following section.

3.2 Nonspherical Lenses

Within the next section, we will successively develop an algorithm for solving equation (1.69). Beginning with the simple Poisson's equation, we shall set up a first version of the scalar field solver. After commenting on problems and possible improvements, we discuss the concept of the point lens approximation and the accuracy of our final and ready-to-use algorithm. Subsequently, we shall apply the algorithm to different matter density distributions.

3.2.1 Choice of the Free Function

According to section 3.1.2 D, we shall restrict all further analysis to one particular choice of $y(\mu)$. Instead of picking a free function like (3.10) which is in good agreement with the observed rotation curves (see section 3.1.2 C), we set $k = 0.01$ and choose the following form of $y(\mu)$:

$$y(\mu) = \frac{\mu^2}{(1-\mu)^2}. \tag{3.14}$$

We will make use of this specific $y(\mu)$ for two reasons: First of all, the choice (3.14) is easily inverted, i.e.

$$\mu(y) = \frac{\sqrt{y}}{1+\sqrt{y}}, \tag{3.15}$$

and therefore it is possible to express the derivative with respect to y analytically:

$$\frac{\partial \mu}{\partial y} = \frac{1}{2\sqrt{y}(1+\sqrt{y})^2}. \tag{3.16}$$

Having a look at equation (1.69), we notice that both $\mu(y)$ and $\partial\mu/\partial y$ are part of the differential equation. Since $\partial\mu/\partial y \to \infty$ for $y \to 0$ (MONDian limit), a possible solver of (1.69) might be extremely sensitive to the corresponding run of $\partial\mu/\partial y$ in that regime. By choosing the analytical expressions (3.15) and (3.16), respectively, we are able to avoid numerical inversion and differentiation of the free function, which may prevent a destabilizing influence on the algorithm. Secondly, our choice allows us to use the analytical Hernquist lens (see section 2.4.4) for comparison in order to test the accuracy and the acceptability of any nonspherical solver for this specific matter density profile. According to section 3.2.1 A, (3.14) is close to the choice of section 2.4.1 and produces nearly the same deflection angle, thus justifying such a comparison.

3.2.2 Solving Poisson's Equation

A. General Approach

Let us consider Poisson's equation in three dimensions which is given by

$$\Delta\Phi(\vec{x}) = \rho(\vec{x}), \tag{3.17}$$

where $\Phi(\vec{x})$ is some scalar field and $\rho(\vec{x})$ the corresponding density field. As a prearrangement for the next section, we want to solve equation (3.17) directly by means of a Fourier transform which is defined as

$$\tilde{\Phi}(\vec{k}) = (2\pi)^{-\frac{3}{2}} \int_{-\infty}^{+\infty} e^{-i\vec{k}\vec{x}} \Phi(\vec{x}) d^3x. \tag{3.18}$$

Thus, applying the above to equation (3.17), we obtain Poisson's equation in Fourier space:

$$-k^2 \tilde{\Phi}(\vec{k}) = \tilde{\rho}(\vec{k}), \tag{3.19}$$

where $k := |\vec{k}|$ is not to be mistaken for the coupling constant of the TeVeS scalar field. Substituting $\tilde{\Phi}$ by use of equation (3.19), a simple inverse Fourier transform leads to the solution of Φ,

$$\Phi(\vec{x}) = -(2\pi)^{-\frac{3}{2}} \int_{-\infty}^{+\infty} e^{+i\vec{k}\vec{x}} \frac{\tilde{\rho}(\vec{k})}{k^2} d^3k. \tag{3.20}$$

For numerical calculation, it is clear that we have to map the respective fields to a three-dimensional grid and switch to a discrete Fourier transform to obtain the according solution, which requires the fields Φ and ρ to be periodic on that grid. As this condition will be violated to some extent in our simulations, we expect the numerical results to show artifacts close to the grid's boundaries. Additionally, we have to take care of the case $k = 0$ because k^2 happens to appear in the denominator of equation (3.20). Therefore, we will simply ignore the zero mode when applying the inverse transform (3.20) and denote the resulting field as Φ'. Since this mode corresponds to a constant contribution c to the density field in real space, it is possible to obtain the proper solution Φ as follows: Applying the Laplacian to the field Φ', we may express the constant c by

$$c = \Delta\Phi' - \rho. \tag{3.21}$$

Introducing the correction field χ,

$$\chi(\vec{x}) = \frac{c}{6} \sum_{i=1}^{3} x_i^2, \tag{3.22}$$

we find the solution Φ to be given by

$$\Phi = \Phi' - \chi, \tag{3.23}$$

which is due to the fact that

$$\Delta(\Phi' - \chi) = \Delta\Phi' - \Delta\chi = \rho + c - c = \rho. \tag{3.24}$$

As is known, a unique solution to (3.17) involves a specific assumption of boundary conditions on the surface of the considered volume. Using the above Fourier method, these conditions are set to be periodic in each dimension.

B. Boundary Conditions

As a matter of fact, we are interested in a solver of (3.17) that can be adapted to arbitrary choices of boundary conditions. This can be accomplished by adding a new field ψ to Φ such that the sum satisfies the designated boundary conditions. Because Φ is already a solution of Poisson's equation, ψ must obey Laplace's equation,

$$\Delta\psi = 0. \tag{3.25}$$

For numerical implementation, we shall again take a fast Fourier-based method. If we consider a three-dimensional box limited by $0 < x, y, z < L$ and set the boundary conditions in two directions to zero, for example

$$\begin{aligned} \psi(x, 0, z) &= 0, \quad \psi(x, L, z) = 0, \\ \psi(x, y, 0) &= 0, \quad \psi(x, y, L) = 0, \end{aligned} \tag{3.26}$$

we may express $\psi(\vec{x})$ by the following Fourier series:

$$\psi(\vec{x}) = \sum_{m,n} q_{mn}(x) \sin\left(\frac{m\pi y}{L}\right) \sin\left(\frac{n\pi z}{L}\right). \tag{3.27}$$

Specifying the boundary conditions in the remaining x-direction and applying the Laplacian to (3.27), we can discretize the appearing differential terms on a grid with N points per dimension, finally arriving at a tridiagonal matrix system for q_{mn} which can be solved with $\mathcal{O}(N)$ arithmetic operations. Inserting the values of q_{mn}, (3.27) yields the corresponding solution of Laplace's equation.

For any given boundary conditions on the whole surface of the box, the above calculation has to be performed analogously for each direction. Since all resulting fields satisfy (3.25), the sought solution is simply given by their sum.

3.2.3 Calculating the Scalar Potential

Having finished the setup for Poisson's equation, we can direct our full attention to equation (1.69). In the following, we will consider an iterative approach to obtain a solution for the scalar field ϕ. Let us define an effective matter density $\bar{\rho}$ which is given as follows:

$$\mu\bar{\rho} = kG\tilde{\rho} - 2\frac{\partial\mu}{\partial y} kl^2 \left((\partial_i\phi)(\partial_j\phi)(\partial_i\partial_j\phi)\right), \tag{3.28}$$

with $k = 0.01$, μ and $\partial\mu/\partial y$ corresponding to (3.15) and (3.16), respectively. This allows us to cast equation (1.69) into the form

$$\Delta\phi = \bar{\rho}. \tag{3.29}$$

As we can see, equation (3.29) resembles Poisson's equation. If we choose $\phi^{(0)}$ as a first guess of the scalar field, e.g. $\phi^{(0)} = (k/4\pi)\Phi_N$, we can calculate an initial density $\bar{\rho}^{(0)}$ by using equation (3.28). Solving Poisson's equation, i.e. equation (3.29) with the r.h.s. being fixed ($\bar{\rho} = \bar{\rho}^{(0)}$), we obtain $\phi^{(1)}$, which can be used in the next iteration step. In summary, the iterative scheme reads as

$$\Delta\phi^{(n+1)} = \bar{\rho}^{(n)}, \tag{3.30}$$

where

$$\begin{aligned} \bar{\rho}^{(n)} &= \frac{kG}{\mu^{(n)}}\tilde{\rho} - 2\left(\frac{\partial\mu}{\partial y}\right)^{(n)} \frac{kl^2}{\mu^{(n)}} \left((\partial_i\phi^{(n)})(\partial_j\phi^{(n)})(\partial_i\partial_j\phi^{(n)})\right), \\ \mu^{(n)} &= \mu(y^{(n)}), \quad \left(\frac{\partial\mu}{\partial y}\right)^{(n)} = \frac{\partial\mu}{\partial y}(y^{(n)}), \qquad y^{(n)} = kl^2|\vec{\nabla}\phi^{(n)}|. \end{aligned} \tag{3.31}$$

Unfortunately, there is no *a priori* way of knowing about the convergence properties of this iterative method. And even if the method happens to converge, it is unclear whether the resulting field ϕ coincides with the sought solution of (1.69). Additionally, we have not yet specified the choice of boundary conditions, which is necessary when solving (3.30). As will become clear in section 3.2.5, we shall always, i.e. for all numerical calculations, assume the boundary values of the fields $\phi^{(n)}$ to match those of the scalar field of our analytical TeVeS point lens (see section 2.4.3) at the boundaries, choosing the point lens's mass M according to the integrated density $\tilde{\rho}$. Within the following sections, we will discuss these and other problems concluding with some improvements of the naive scheme from above.

3.2.4 Convergence and Other Problems

A. Monitoring the Iteration

When applying the iteration introduced in the last section, it would be desirable to somehow track the behavior of the iteration process and gain knowledge about the evolution of $\phi^{(n)}$ and its departure from the actual solution of (1.69). Independently of convergence, we may define a "χ^2-like" quantity $\tilde{\chi}^2$ on a three-dimensional grid which is given as

$$\begin{aligned}(\tilde{\chi}^2)^{(n)} &= \sum_{i,j,k=0}^{N-1} \frac{(\Delta\phi^{(n)} - \bar{\rho}^{(n)})^2_{ijk}}{\eta^{(n)}}, \\ \eta^{(n)} &= kG \int \frac{\tilde{\rho}}{\mu^{(n)}} d^3x,\end{aligned} \tag{3.32}$$

where the indices ijk denote the position (i, j, k) of a grid point and N is the maximum number of points in each dimension. Because both $\Delta\phi^{(n)}$ and $\bar{\rho}^{(n)}$ can become zero within the iteration, we have introduced $\eta^{(n)}$ to make $\tilde{\chi}^2$ a normalized quantity. Our $\tilde{\chi}^2$ is suitable for exploring the principle iteration properties of a single problem, but without any further reference, it does not reveal any information about the quality of a reached limit ϕ,

$$\phi \equiv \lim_{n\to\infty} \phi_n, \tag{3.33}$$

supposing the iteration has converged. However, in cases where we are able to estimate the accuracy of such a limit (see section 3.2.6), we can define its corresponding $\tilde{\chi}^2$ as a standard value which we will refer to as $\tilde{\chi}^2_{ref}$. To assign a certain $\tilde{\chi}^2$ to a reached limit ϕ, we additionally have to introduce an stopping criterion for the iteration. If not specified in any other way, we will use the following one for all convergent cases:

$$\frac{\left|(\tilde{\chi}^2)^{(n+1)} - (\tilde{\chi}^2)^{(n)}\right|}{(\tilde{\chi}^2)^{(n)}} < 10^{-4}. \tag{3.34}$$

Then, using our iteration-based solver for other mass density distributions, any $\tilde{\chi}^2$ satisfying

$$\frac{\tilde{\chi}^2}{\tilde{\chi}^2_{ref}} \lesssim 1 \tag{3.35}$$

will imply an accuracy equal to or even better than the one of the reference case, thus allowing control of the actual quality of the obtained solution ϕ.

B. First Guess

Concerning our proposed method for solving (1.69), we may assume that the choice of the initial field $\phi^{(0)}$ will have quite a significant influence on the iteration's convergence properties. To establish the best possible conditions for the solver, we shall try to find an initial guess that is somewhat close to the sought solution. Since the scalar field recovers both Newtonian and MONDian features in the corresponding regimes, we will take the following expression for the first guess $\phi^{(0)}$ ($r = 0$ corresponds to the grid's center):

$$\phi^{(0)} = \exp\left(-\frac{r}{\lambda}\right) \Phi_N + \left(1 - \exp\left(-\frac{r}{\lambda}\right)\right) \phi_p, \tag{3.36}$$

where λ is a suitable length scale and ϕ_p the three-dimensional scalar potential of the TeVeS point lens introduced in section 2.4.3 which depends on the volume's total mass M,

$$\phi_p = \sqrt{GMa_0}\log(r). \tag{3.37}$$

Because most of the baryonic matter content will be concentrated closely around the grid's center in basically all considered cases, (3.36) has been constructed such that $\phi^{(0)}$ approaches the field of a corresponding point mass for large values of r. Setting

$$\lambda \approx \frac{N\Delta x}{4}, \tag{3.38}$$

where N again denotes the total number of grid points per dimension and Δx the distance between neighboring grid points, for our calculations, it is possible to build a convergent solver for ϕ, which will be the subject of the following sections. When applying the point lens approximation introduced in section 3.2.5, however, it turns out that it is already sufficient to take

$$\phi^{(0)} = \phi_p. \tag{3.39}$$

As this approximation turns out to be a core part of our solver, we shall make use of (3.39) for all simulations whose results are presented below.

C. Structure of the PDE and Oscillations

Let us have a closer look at equation (3.28): Solving for $\bar{\rho}$, we can identify two terms depending on the free function. While the first term contains only a factor μ^{-1}, the second one involves the product $(\partial\mu/\partial y)\mu^{-1}$. From equations (3.15) and (3.16), respectively, we know that both the derivative and μ^{-1} diverge in the MONDian limit, i.e. for $y \to 0$. Therefore, small values of $|\vec{\nabla}\phi|$ that could be approached during the iteration would lead to an explosion of the effective density $\bar{\rho}$, which might actually hint on the possible appearance of oscillations, causing a deterioration of the iterative method's convergence properties. Indeed, numerical analysis has shown that such oscillations occur, being especially strong where there is a significant contribution of the baryonic matter density $\tilde{\rho}$. Of course, it is unclear whether the above considerations are connected to these oscillations at all. And even if they were, one would have to take into account that there could be other hidden features of (3.28) that might be as well responsible for this behavior. Anyway, as we have no information about such features, we shall not further care about this issue. For some choices of the matter distribution and the grid volume, we have found the iteration to approach a limit close to the boundaries, but when moving to the center of the grid, i.e. the region where we have actually placed most of the baryonic matter content, our method fails to converge, with the $\phi^{(n)}$ oscillating heavily. For example, considering a grid with N points per dimension that covers a volume of $V = (50kpc)^3$ (the choice of this specific volume will become clear in section 3.2.6), we have applied our method to a Hernquist profile with the parameters from section 2.4.4, setting $N = 128, 256, 384$ and using the scalar field of a point lens as the first guess (see section 3.2.4 B). While the iteration converges within $10-15$ steps near the boundary of the box, the inner part shows an oscillatory behavior with strongly varying amplitude for all our choices of N. In general, however, there is no convergence at all including cases where the $\phi^{(n)}$ more and more depart from the actual solution. Clearly, we have to find a convergence mechanism for our iteration scheme, two of them being presented within the following sections.

D. Forcing Convergence I

If we assume the MONDian limit of the free function to be the main cause of the just mentioned oscillations, a possibility to overcome our problems might be to directly consider the first derivatives of the scalar field ϕ. Since both μ and its derivative $\partial\mu/\partial y$ depend on the modulus of $\vec{\nabla}\phi$, it could be helpful to modify these fields within each iteration step in order to soften fluctuations of the source term $\bar{\rho}$. Therefore, let us define a correction function $S(r)$ which is given as follows:

$$S(r) = \left(\frac{r}{r_0} + 1\right)^{-1} \left(\frac{r}{r_0} + a\right), \tag{3.40}$$

where $r = 0$ corresponds to the center of our grid and a, $r_0 \in \mathbb{R}^+$. To simplify matters, we have chosen a spherically symmetric form of the correction function, which will be sufficient to discuss the motivation behind this method. While a is the limit of $S(r)$ for $r \to 0$,

$$\begin{aligned} S(r) &= a, \quad r \to 0 \\ S(r) &= 1, \quad r \to \infty, \end{aligned} \tag{3.41}$$

the scale radius r_0 controls the change of the function $S(r)$ for increasing r. The corresponding corrected fields are obtained by multiplying the first derivatives of the scalar field with $S(r)$ during each iteration step, yielding a modified expression for $\bar{\rho}^{(n)}$. The main idea of (3.40) is to scale up the fields $\phi_{,i}$ in order to enlarge the value of $|\vec{\nabla}\phi|$, choosing an appropriate $a > 1$. Thus, it could be possible to avoid values of the free function μ and $(\partial\mu/\partial y)^{-1}$, respectively, that are very close to zero. As we have pointed out, the observed oscillations are especially strong where there is a significant amount of matter density. Because most of the matter content is located around the very center of the grid for all our choices of $\tilde{\rho}$, (3.40) has been designed such that the correction factor S is largest in the center and decreases towards the limit $S = 1$ when moving outwards. Moreover, the radial gradient of the correction function can be controlled by setting the scale radius r_0, which allows to adjust the values of $S(r)$ on the boundaries of the grid. Considering a particular choice of $\tilde{\rho}$, it is, of course, possible to customize the method by incorporating these properties into a more generic correction function S.

Embedding the above into the iteration we have introduced in section 3.2.3, we can apply the resulting scheme to a set of different matter density distributions. Unfortunately, the outcome is rather disappointing: While it is actually possible to achieve convergence for the Hernquist profile and few other problems, the proposed scheme generally seems to fail when considering more arbitrarily shaped lenses being of both spherical and nonspherical symmetry. For instance, our method already runs into serious trouble when assuming a flat spherical or a weakly elliptical density profile. Even if we adapt (3.40) to the form of the particular density $\tilde{\rho}$ or apply several other modifications, there seems to be no way to induce convergence to the iteration for those cases. Surprisingly, considering our successfully treated problems, one has to allow for $a < 1$ to make our method work. Clearly, such choices of a are contradictory to the above motivation as the values of $|\vec{\nabla}\phi|$ are decreased at each grid point, which strongly suggests that the reasons for the observed oscillations, i.e. the intrinsic properties of (1.69), are far more complicated than first supposed in our approach. In cases where (3.40) or similar schemes are successful, the convergence properties can be improved by coupling the particular value of a to the $\phi_{,i}$ for each iteration step, thus lowering the amount of necessary iterations. Despite this enhancement, however, the total amount of needed steps (and time) stays quite high ($\gtrsim 250$), and therefore, referring to a grid with $N = 384$, we may consider the method to be quite slow if working at all. In section 3.2.6, we will briefly comment on the method's accuracy for the Hernquist lens introduced in section 2.4.4.

In summary, we conclude that this approach does not satisfy our purposes, mainly because it allows for the treatment of few matter distributions only. As we are interested in investigating many different types of lenses, we desire a mechanism that is rather independent of the particular form of the lens or other given input. Within the next section, we shall see that there is a technique which will mostly satisfy our requirements.

E. Forcing Convergence II

In the following, we shall consider a completely different approach to ensure convergence of our iterative method. Instead of modifying any fields according to some complicated scheme which possibly involves many different unknown parameters, one might simply think of including a relaxation into the iteration. Therefore, we substitute equation (3.30) by the following

Total grid points per dimension N	128	256	384
Optimal parameter ω_0	0.68	0.70	0.75

Table 3.1: Dependence of the optimal parameter ω_0 on the chosen grid size

expressions:

$$\begin{aligned} \Delta\tilde{\phi}^{(n)} &= \bar{\rho}^{(n)}, \\ \phi^{(n+1)} &= \omega\tilde{\phi}^{(n)} + (1-\omega)\phi^{(n)}, \end{aligned} \tag{3.42}$$

where we have introduced the relaxation parameter $\omega \in \mathbb{R}$ and an additional iteration field $\tilde{\phi}^{(n)}$. For suitable values of ω, this modification turns out to work very well as it is capable of enforcing fast convergence for a variety of problems. However, our investigation has shown that the relaxation's success is very sensitive to the particular choice of ω, i.e. the iteration does only converge if ω is chosen from a very narrow range around some optimal parameter ω_0 which actually appears to depend on the considered grid. Setting N to 128, 256 and 384, respectively, Table 3.1 shows the different empirically found values for ω_0. Fortunately, these values seem to be almost independent of the particular density profile, and thus, as long as N is not changed, it will not be necessary to adjust ω. Therefore, choosing a certain N and its corresponding value of ω, we have finally gained a complete and working solver for the scalar field ϕ that does not depend on any additional input related to the considered density profile $\tilde{\rho}$. To achieve a reasonable level of resolution, we shall set $N = 384$ and $\omega \approx 0.75$ for further analysis. Applying our new method to a Hernquist profile with the parameters from section 2.4.4, we notice fast convergence compared to our first approach since the amount of necessary iteration steps drops below a value of 40. Using our analytical model of the Hernquist lens, we shall discuss the solver's accuracy in section 3.2.6.

Despite its great success, (3.42) has also some problems that we briefly want to mention here: Concerning more complicated density distributions, we have found the relaxation to be less efficient, i.e. the iteration generally takes more time to converge. As it turns out, this cannot be avoided by changing the relaxation parameter ω, which would actually lead to even worse convergence properties or a complete failure of the method. Still, the additional amount of time that has to be employed is acceptable in most cases. Far more concerning is another issue: Independently of the corresponding value of ω, we encounter the relaxation to generally fail for certain choices of $\tilde{\rho}$, which can mostly be resolved by slightly modifying the original density. Probably, this second problem is of purely numerical origin, but although it seems very unlikely, we point out that it might also hint on a class of density distributions with exceptional solutions of the scalar field ϕ that are not accessible to our solver. When applying the solver together with the point lens approximation (see section 3.2.5), we will return to these issues giving a detailed description of particular situations.

F. Limited Box Size

Considering the calculation of the deflection angle according to equation (2.31), another problem has to be taken into account. Due to the limited amount of computer capacity, the numerical calculation can only be performed with respect to a finite grid volume, which means truncating the integral in (2.31) at some point. As previously mentioned, the scalar field's gradient decreases much more slowly compared to the Newtonian one far away from the lens, and since we have $\phi \propto \log(r)$ there, one would actually be obliged to move to very large volumes in order to neglect contributions from outside the box and obtain correct results for the deflection angle. Thus, assuming a fixed value of N, this would excessively degrade the resolution of the corresponding two-dimensional lensing maps. For instance, setting $N = 384$, we would have to choose the

volume such that virtually all information on the lens's inner structure, which is exactly what we are interested in, would be lost. Obviously, assuming sufficient resources, this problem could be solved by increasing the value of N. In that case, however, the actual part of our interest would make up but a fraction of the considered grid volume, making an approach like that very inefficient, especially with respect to the required amount of time. Therefore, we shall follow a different approach, the so-called point lens approximation, which will be introduced within the next section.

3.2.5 Point Lens Approximation

Considering a finite grid with N points per dimension (N is chosen as an even number), we may rewrite the scalar part of equation (2.31) as the sum of contributions coming from both inside and outside the grid's volume:

$$\vec{\tilde{\alpha}}_s = 2\int_{-\frac{N}{2}\Delta x}^{\frac{N}{2}\Delta x} \vec{\nabla}_\perp \phi^{(in)} dz + 4\int_{\frac{N}{2}\Delta x}^{\infty} \vec{\nabla}_\perp \phi^{(out)} dz, \tag{3.43}$$

with the quantity Δx again denoting the distance between neighboring grid points. Assuming that the scalar field at the boundaries is approximately given by that of a point lens, i.e.

$$\phi^{(out)} \approx \sqrt{GMa_0}\log(r), \tag{3.44}$$

we obtain the following expression (M denotes the total mass inside the volume):

$$\vec{\tilde{\alpha}}_s = 2\vec{I} + 4\vec{A}, \tag{3.45}$$

where

$$\vec{I} = \int_{-\frac{N}{2}\Delta x}^{\frac{N}{2}\Delta x} \vec{\nabla}_\perp \phi^{(in)} dz \tag{3.46}$$

and

$$\vec{A} = \frac{\sqrt{GMa_0}}{q}\left[\frac{\pi}{2} - \arctan\left(\frac{N\Delta x}{2q}\right)\right]\begin{pmatrix} x \\ y \end{pmatrix}, \tag{3.47}$$

with $q^2 = x^2 + y^2$.

If applicable, the point lens approximation is able to resolve the problem addressed in section 3.2.4 F, thus enabling the correct calculation of the deflection angle $\vec{\tilde{\alpha}}$. According to equations (3.45) – (3.47), we need to perform the integration only over our finite grid since all contributions from outside the box can be expressed analytically. In this case, the full deflection angle is simply given by the sum of $4\vec{A}$ and twice the numerical result of the truncated integration. In order to apply the point lens approximation, one has to choose the grid's volume such that it is possible to inscribe a sphere with radius R satisfying

$$R \approx \xi_p, \tag{3.48}$$

where ξ_p is the *point lens radius* we have introduced at the end of section 2.4.4. Within this approximation, we shall always use the corresponding analytical point lens as an initial guess of the scalar field,

$$\phi^{(0)} = \sqrt{GMa_0}\log(r),$$

where M is the total mass of the particular lens (see sections 3.2.1 A and 3.2.4 B). Concerning our solver for Poisson's equation introduced in section 3.2.2, we may additionally assume the boundary conditions of the fields $\phi^{(n)}$ to be of spherical symmetry, matching the values of (3.37) at the boundaries. Combining the solver introduced in section 3.2.4 D with the above approximation, we eventually do have a tool which allows the numerical treatment of generic lens systems in TeVeS. Before applying our tool to nonspherical lenses, however, we shall examine its accuracy in the following section.

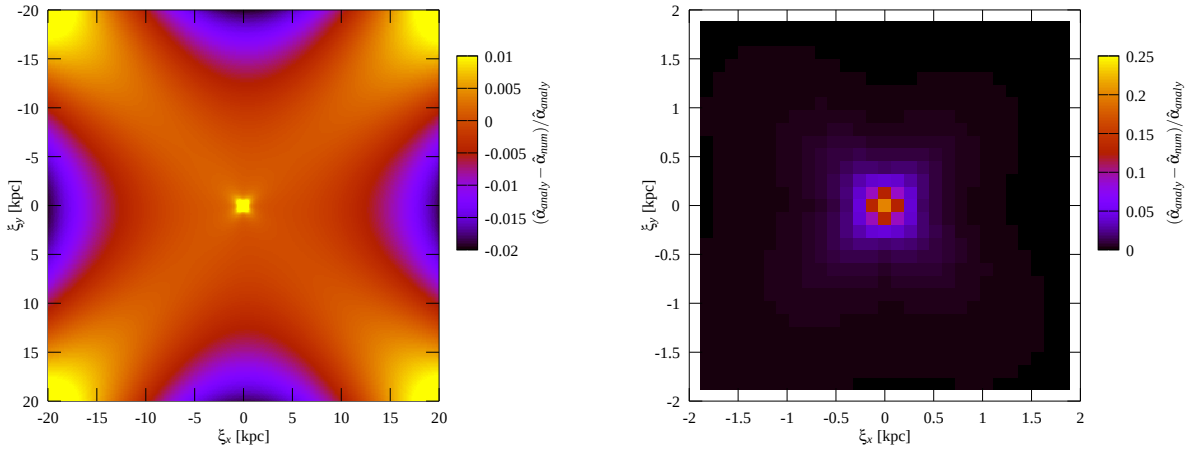

Figure 3.7: Accuracy test of the numerical method: Assuming a Hernquist lens with the parameters from section 2.4.4, we compare the numerical result for the deflection angle $\hat{\alpha}(\vec{\xi})$ to the analytical one. The left panel shows the relative difference $\Delta\hat{\alpha}_{rel} = (\hat{\alpha}_{analy} - \hat{\alpha}_{num})/\hat{\alpha}_{analy}$. Please note that the quantity $\Delta\hat{\alpha}_{rel}$ is limited by $-0.02 \leq \Delta\hat{\alpha}_{rel} \leq 0.01$ for reasons of presentation, values outside this range are truncated. The right panel illustrates the relative deviation for the central part where $\Delta\hat{\alpha}_{rel}$ reaches a maximum of approximately 20%.

3.2.6 Accuracy

A. Comparison to the Analytical TeVeS Hernquist Lens

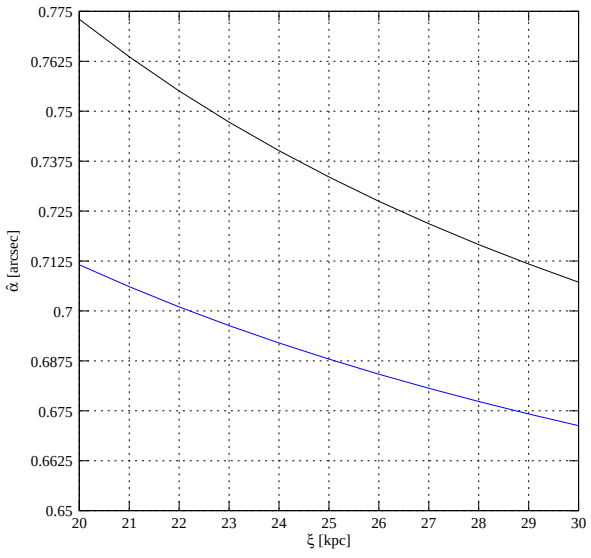

Figure 3.6: The point lens approximation for the Hernquist lens: Presented are the TeVeS deflection angles caused by a point mass (black line) and a Hernquist profile (blue line) using our analytical models and the parameters from sections 2.4.3 and 2.4.4. At $\xi \approx 25kpc$ there is a relative difference of roughly 6%.

In this section, we will determine the accuracy of our developed tool by comparing the numerically obtained deflection angle of a Hernquist lens to the corresponding analytical result assuming the parameters from section 2.4.4. As previously mentioned, such a comparison is justified according to our analysis in sections 3.1.1 and 3.1.2 A. Concerning the numerical setup, we choose a grid volume of $V = (50kpc)^3$ (the lens is placed in the grid's center) and set the redshifts of source and lens to $z_{source} = 3$ and $z_{lens} = 0.63$, respectively. If not explicitly noted, we shall keep this choice of redshifts throughout the following sections. Let us check if the point lens approximation is applicable with these settings. From Figure 3.6, we notice that the relative deviation $\Delta\hat{\alpha}_{rel,analy}$ between the analytical Hernquist and its corresponding point lens is approximately 6% at $\xi \approx 25kpc$. Obviously, this difference is still quite large and therefore, (3.48) is poorly satisfied. On the other hand, however, moving to a larger volume would lead to a loss in resolution. Thus, in order to balance accuracy and resolution ($N = 384$), we assume the validity of (3.48) for our grid, i.e. $\Delta\hat{\alpha}_{rel,analy} \approx 0$ at the boundaries, and apply the point lens approximation keeping the volume from above. In this case, we are able to resolve structures up to a minimum extent of $\Delta x \approx 130pc$. The left panel of Figure 3.7 shows the relative difference $\Delta\hat{\alpha}_{rel} = (\hat{\alpha}_{analy} - \hat{\alpha}_{num})/\hat{\alpha}_{analy}$ between

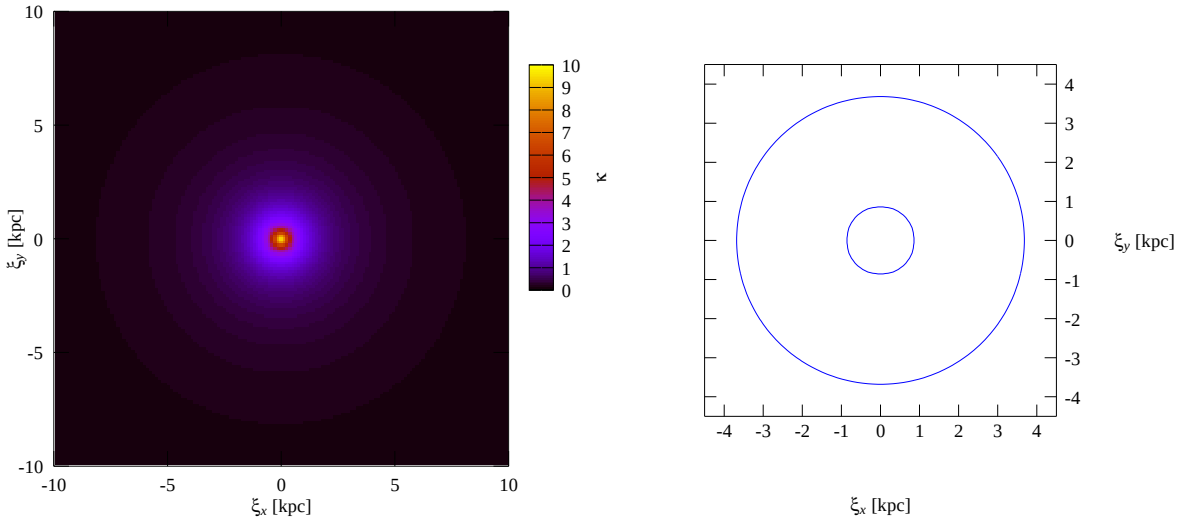

Figure 3.8: Numerically calculated convergence map (left) and critical lines (right) for the Hernquist lens using the parameters from section 2.4.4. The critical lines are calculated by interpolation between the grid points.

the numerical and the analytical deflection angle of the Hernquist lens. For reasons of presentation, we have limited the range of $\Delta\hat{\alpha}_{rel}$ to $-0.02 \leq \Delta\hat{\alpha}_{rel} \leq 0.01$. Ignoring the very center of the map (right panel), we find the relative deviations in the interior to be of $\mathcal{O}(10^{-3})$. Moving outwards, i.e. to larger $\xi = |\vec{\xi}|$, these deviations increase and reach values up to $5 - 6\%$ at the grid's boundaries ($\xi \gtrsim 25kpc$). However, as long as $\xi \lesssim 15kpc$, we still have $\Delta\hat{\alpha}_{rel} \lesssim 1\%$, again neglecting the central part. The large differences close to the boundaries are likely to be a mixture of artifacts caused by the Fourier transform of actual nonperiodic fields and contributions due to (3.47) which become more significant with increasing ξ. Having a look at the right panel of Figure 3.7, we see that $\Delta\hat{\alpha}_{rel}$ strongly increases in the central region reaching a maximum value of roughly 20%. The reasons for these large deviations are probably related to both the limited (and finite) resolution of our grid and the small values of $\hat{\alpha}$ in the center. According to section 2.4.4, the TeVeS deflection angle of the analytical Hernquist lens decreases to zero for $\xi \rightarrow 0$. Since this transition happens on a rather small scale and our resolution is limited by $\Delta x \approx 130pc$, the distance between neighboring grid points, our numerical model cannot fully recover the deflection angle in the central region. Moreover, concerning the Hernquist lens, another problem has to be considered: Because of (2.60), the projected mass density as well as the convergence become infinite at $\xi = 0$, which, of course, cannot be accomplished in a numerical calculation. The left panel of Figure 3.8 illustrates the convergence map we have obtained in our simulation. Clearly, the convergence has a strong peak at $\xi \approx 0$ ($\kappa \approx 10$), corresponding to the singularity of the Hernquist lens at this point. Due to the limited resolution of our grid, this singularity is smoothed out, resulting in the observed finite peak, which actually causes an effective loss of mass in our numerical model. This loss of total mass has an overall influence on the deflection angle and may significantly contribute to the errors we have discussed above. As, in our case, the matter density is changed in the very center, this effect is very likely to be the main reason for the large deviations found there. In the following, however, we shall only consider smooth matter density distributions and therefore, any further discussion about this issue becomes redundant. The right panel of Figure 3.8 shows the critical lines of our numerical model which are determined by interpolation between the according grid points. Within our resolution limit, we find the radii of these lines to perfectly agree with those of the analytical model.

As we are mainly interested in the strong lensing regime, we shall restrict ourselves to the grid's interior where we can assume an accuracy of $\mathcal{O}(10^{-3})$. Due to finite resolution, how-

ever, we expect the accuracy to degrade to some extent in regions where the deflection angle $\hat{\alpha}$ approaches values close to zero when moving to more generic lens systems. Although smooth density profiles will probably not produce deviations as large as we have found around $\xi \approx 0$ for the Hernquist lens, we cannot make any specific statements on the quality of our simulations in such areas. Still, this should affect but a fraction of the overall result, thus being acceptable for the upcoming analysis. Using our numerical result for the Hernquist lens, we now additionally have a standard value for the quantity $\tilde{\chi}^2$ which has been introduced in section 3.2.4 A. Interestingly, compared to other simulations involving smooth fields $\tilde{\rho}$, we notice that the value of $\tilde{\chi}^2$ corresponding to the Hernquist lens is by several orders of magnitude larger than in all other cases, therefore implying a better accuracy of the numerical solution of the scalar field ϕ. Unfortunately, there is no way to benefit from this situation, simply because we have no idea how $\tilde{\chi}^2$ translates into an accuracy and what the actual influence of the scalar field on the overall error is. Thus, if not specified in any other way, we shall assume an accuracy equal to that of the Hernquist lens for all numerical simulations that satisfy (3.35) and similarly allow using the point lens approximation. In the following, all presented results will comply with these requirements.

Concerning the appearance of Fourier artifacts close to the boundaries, one might actually think of further modifying our numerical solver for the scalar field: According to equation (3.31), the iteration density $\bar{\rho}^{(n)}$ may have significant contributions violating the periodicity condition of the density field which is necessary when applying the Fourier transform (see section 3.2.2). Thus, it could be expedient to smoothly cut $\bar{\rho}^{(n)}$ near the boundaries within each iteration step in order to avoid such problems. However, while this modification turns out to slightly improve the method's accuracy for the Hernquist lens, it causes strange artifacts in the numerical results when switching to other lens systems. Therefore, we shall keep to the present form of our solver, just as introduced in section 3.2.4 E.

B. Comparison to the Method from Section 3.2.4 D

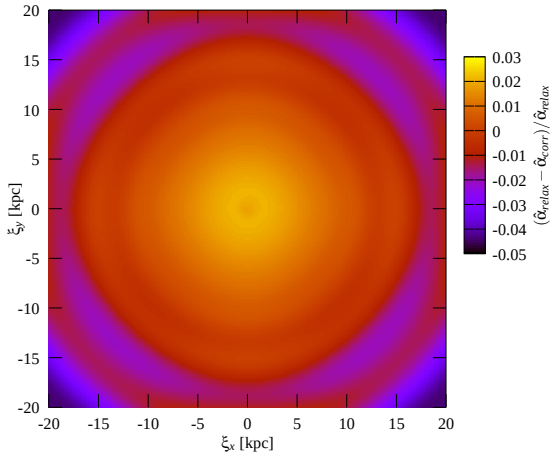

Figure 3.9: Assuming a Hernquist lens with the parameters from section 2.4.4, we compare the numerical results for the deflection angle $\hat{\alpha}(\vec{\xi})$ using the methods from 3.2.4 D and E, respectively. Obviously, the deviation $\Delta\hat{\alpha}_{rel} = (\hat{\alpha}_{relax} - \hat{\alpha}_{corr})/\hat{\alpha}_{relax}$ shows a radially oscillating pattern and reaches absolute values up to $3 - 5\%$.

As mentioned before, a numerical treatment of the Hernquist lens is also possible using the method proposed in section 3.2.4 D. Figure 3.9 illustrates the relative difference $\Delta\hat{\alpha}_{rel} = (\hat{\alpha}_{relax} - \hat{\alpha}_{corr})/\hat{\alpha}_{relax}$ between the numerical deflection angles obtained for our two convergence mechanisms, with the indices *relax* and *corr* denoting the methods from 3.2.4 E (relaxation) and D (field correction), respectively. As we can see, $\Delta\hat{\alpha}_{rel}$ shows an oscillatory behavior and the deviation reaches absolute values up to $3 - 5\%$. According to our analysis in section 3.2.6 A, these oscillations are due to $\hat{\alpha}_{corr}$ and must be an intrinsic property of the applied convergence scheme as all other conditions including the point lens approximation are exactly the same. Therefore, we may conclude the following: Even if it is possible to achieve convergence, the scheme introduced in section 3.2.4 D is less accurate than our relaxation method, assuming the iteration's stopping criterion (3.34) in both cases. Since the relaxation is also much faster, i.e. it needs

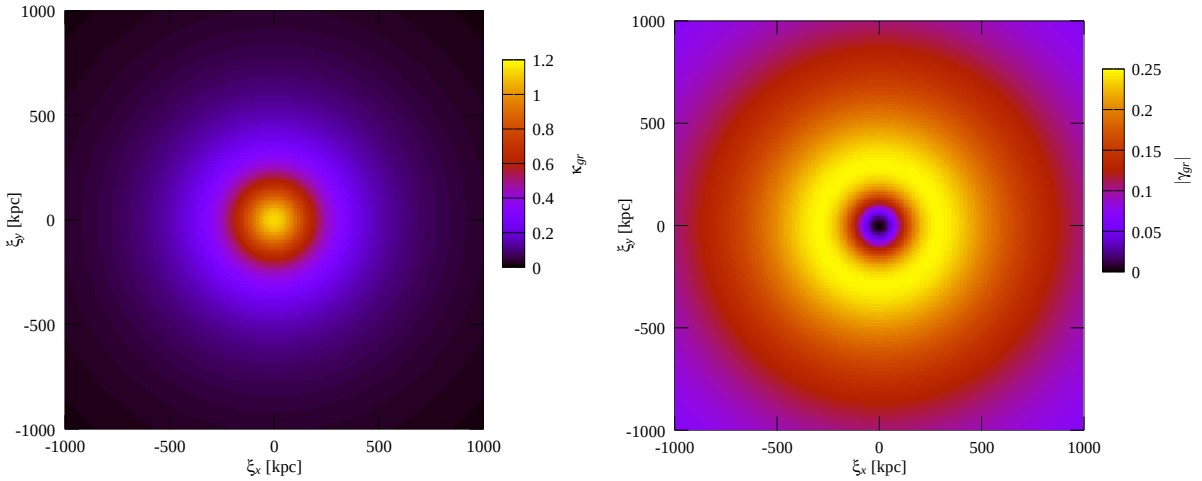

Figure 3.10: Numerically calculated GR convergence (left) and GR shear (right) map for the King-like profile (3.50) introduced in section 3.2.7. Please note that the presented results are completely independent of the particular choice of z_0, which is in accordance with our simulations.

much fewer iteration steps, there is no need to consider this insufficient approach concerning our further investigations.

3.2.7 Thin Lens Approximation

As our first task, we want to investigate the validity of the thin lens approximation in TeVeS. According to former work considering lensing in classical MOND (Mortlock & Turner, 2001), we expect a break-down of the approximation due to the nonlinear coupling of the scalar field to the three-dimensional matter density. In the following, however, we are rather interested in quantifying this break-down by exploring the lensing properties of a mass distribution being contracted or stretched along the line of sight, i.e. the z-direction, making use of our new numerical tool. For this purpose, let us consider a three-dimensional density distribution $\tilde{\rho}$ following a King profile (King, 1962) which is given by

$$\tilde{\rho}(r) = \tilde{\rho}_0 \left(1 + \left(\frac{r}{r_c}\right)^2\right)^{-\frac{3}{2}}, \tag{3.49}$$

where r_c is the core radius and $\tilde{\rho}_0$ the physical matter density at $r = 0$. Equation (3.49) is an empirical law that fairly describes the distribution of both galaxies and gas inside a galaxy cluster and will also be used for the toy model of the cluster merger 1E0657 − 558 in section 3.2.11. However, in order to analyze TeVeS effects which are only due to the lens's extent along the line of sight, we have to parameterize the lens's "thickness" and additionally ensure a constant projected mass density. Thus, we introduce a slightly modified profile which is given as follows:

$$\tilde{\rho}(q, z) = \tilde{\rho}_0 \mathcal{Q}(q) \mathcal{Z}(z), \tag{3.50}$$

where

$$\mathcal{Q}(q) = \left(1 + \left(\frac{q}{q_0}\right)^2\right)^{-1} \tag{3.51}$$

and

$$\mathcal{Z}(z) = \left(1 + \left(\frac{z}{z_0}\right)^2\right)^{-\frac{1}{2}}, \tag{3.52}$$

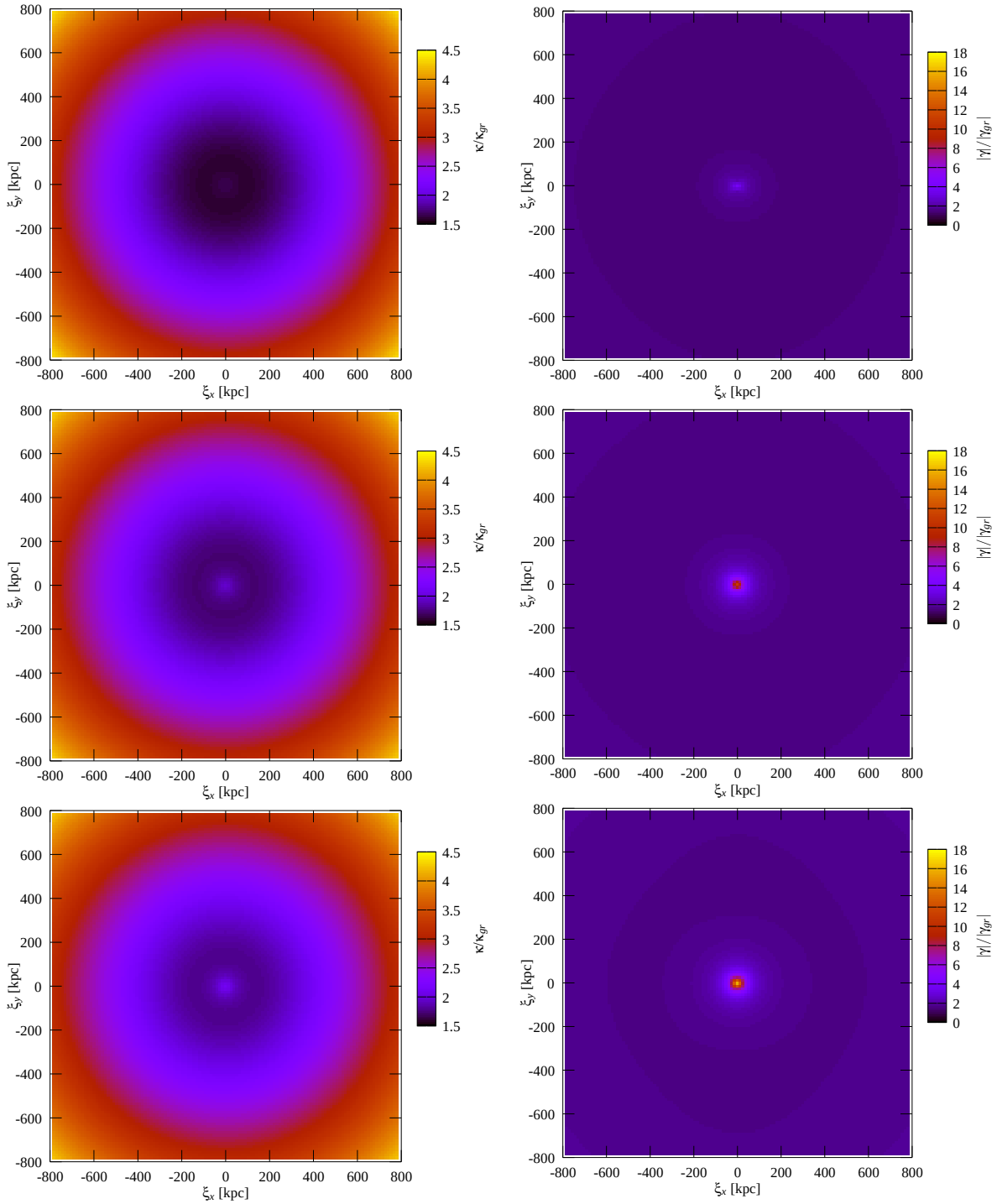

Figure 3.11: Numerically calculated TeVeS convergence and TeVeS shear map for the King-like profile (3.50) expressed in terms of the GR convergence κ_{gr} and the GR shear $|\gamma_{gr}|$, respectively. Choosing $z_0 = 50kpc$ (top panel), $z_0 = 200kpc$ (middle panel) and $z_0 = 400kpc$ (bottom panel), we see that both the effective TeVeS convergence and the corresponding shear are significantly amplified in the central region when moving to higher values of z_0.

with q_0, $z_0 > 0$ being the corresponding core lengths and $q^2 = x^2 + y^2$. Since the expressions (3.52) and (3.51) are obtained by integrating (3.49) over one and two dimensions, respectively, our new choice (3.50) is actually kept close to the original King profile. Varying the parameter z_0, we are now able to directly control the lens's extent in the z-direction, and, assuming that

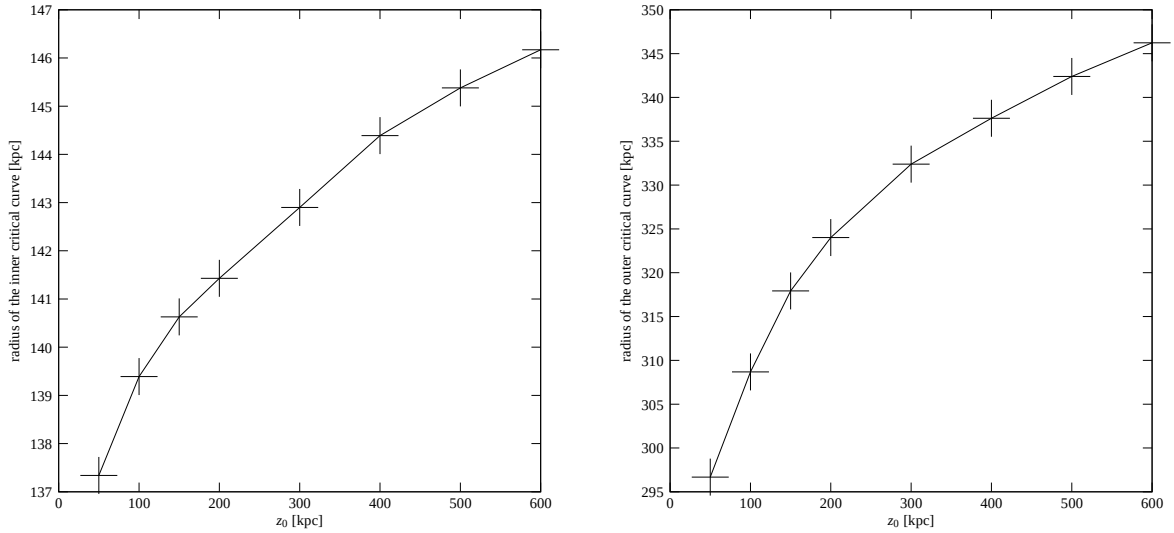

Figure 3.12: Radii of the inner (left) and outer (right) critical curve for different choices of z_0: Increasing the lens's extent along the line of sight, the radius of the inner (outer) critical curve is driven outwards showing relative changes of up to roughly 6% (16%). The critical lines are calculated by interpolation between the grid points.

the profile (3.50) can be cut off at some point, we find

$$\int_{-\infty}^{\infty} dz\tilde{\rho}(q,z) \propto \mathcal{Q}(q) \tag{3.53}$$

for any choice of z_0, which perfectly satisfies our needs. Concerning the numerical setup, we take the point of origin, i.e. $x = y = z = 0$, to coincide with the grid's center and assume the density profile (3.50) to be smoothly cut at a radius of $R = 1.5Mpc$, which is necessary as, otherwise, our King-like profile would contribute an infinite amount of mass. In accordance with the point lens approximation, we set the grid's volume to $V = (5Mpc)^3$, thus having a spatial resolution of $\Delta x \approx 13kpc$ ($N = 384$). Furthermore, we take $q_0 = 200kpc$ and choose $\tilde{\rho}_0$ such that the lens's total mass,

$$M = \int_V dV\tilde{\rho}(q,z), \tag{3.54}$$

is given by $M = 10^{15}M_\odot$. Regarding the remaining parameters, we keep the settings introduced in section 2.4.4 and remind the reader that the redshifts of source and lens are fixed to $z_{source} = 3$ and $z_{lens} = 0.63$, respectively. Henceforth, if not explicitly noted, all presented numerical results are based upon these settings, including the spherical cut-off of the particular density profile $\tilde{\rho}$ at $R = 1.5Mpc$.

As we have to meet condition (3.48) in order to apply the point lens approximation, we are obliged to satisfy $z_0 \lesssim 600kpc$ in our numerical simulations. According to equation (2.59), we expect the MONDian influence to become significant around the critical radius $r_0 \approx 1.1Mpc$ (see section 2.4.3), but there should still be noticeable effects when varying z_0 on our limited range. Figure 3.11 shows both the TeVeS convergence and the TeVeS shear map of our King-like profile (3.50) expressed in terms of the corresponding GR quantities which are additionally presented in Figure 3.10. Please note that the GR maps are independent of the particular choice of z_0. Increasing z_0 from $50kpc$ to $400kpc$, we observe a significant amplification of the TeVeS convergence around the center while there is basically no change moving to the outer region. Furthermore, we notice that the variation of z_0 seems to have no visible effect on the symmetry properties of the convergence map. Concerning the TeVeS shear map, we find a similar behavior: While there is a strong increase of $|\gamma|$ in the very center, we find only small changes in the outer parts.

Interestingly, the TeVeS shear $|\gamma|$ is not circularly symmetric in that region any longer, with the exact form depending on the particular extent of the lens. Rather than being intrinsic to TeVeS, this is probably due to purely numerical problems like, for instance, possible artifacts caused by the scalar field solver or basic assumptions, e.g. the point lens approximation, an influence of the latter being actually expected as the choice of z_0 has an impact on (3.48). However, since this effect does not produce any visible distortion in the overall result, we shall pay no further attention to it. Instead, let us continue our analysis considering the effects on the critical lines due to the changes of κ and $|\gamma|$: Since (3.50) is axially symmetric, the corresponding lines turn into circles. In Figure 3.12, the radii of both the inner and outer critical curve are presented for different values of the parameter z_0. Obviously, these radii are increased when stretching the lens along the line of sight, showing relative deviations of up to roughly 6% and 16% for the inner and outer radius, respectively. Please note that the critical lines are calculated by interpolation between the grid points, thus allowing to determine positions which are actually below the grid's resolution. Although our investigation is limited to a small range of z_0, we find appreciable differences between the lensing maps which are assumed to considerably grow when stretching the lens further.

Summarizing the above, we may conclude that the lens's extent along the line of sight significantly affects the strong lensing properties. Therefore, the mass distribution along the z-axis can be regarded as an additional degree of freedom in TeVeS. Concerning the numerical solver for the scalar field, we notice an increase of iteration steps moving away from spherical symmetry. For $z_0 = 600kpc$, we encounter a maximum of about 250 steps, but referring to the spherical case, the amount of needed steps drops below 50.

3.2.8 Elliptical Lens Models

In this section, we shall consider lens systems whose projected mass density follows an elliptic profile. Therefore, introducing the scale lengths $x_0, y_0, z_0 > 0$, let us consider a matter density distribution of the form

$$\tilde{\rho}(r) = \tilde{\rho}_0 \left(1 + \left(\frac{x}{x_0}\right)^2 + \left(\frac{y}{y_0}\right)^2 + \left(\frac{z}{z_0}\right)^2\right)^{-\frac{3}{2}}, \tag{3.55}$$

which obviously coincides with the original King profile for $x_0 = y_0 = z_0 = r_c$. Keeping y_0 and z_0 fixed, $y_0 = z_0 = 200kpc$, we may investigate the lensing properties for different choices of the parameter x_0, again setting the total mass to $M = 10^{15} M_\odot$. Figure 3.13 illustrates both the TeVeS convergence κ and the corresponding ratio κ/κ_{gr}, with x_0 set to values of $150kpc$, $250kpc$, and $350kpc$, respectively. Although the symmetry properties of the GR convergence map are virtually sustained in TeVeS, we can observe an interesting feature located in the central part: Compared to its neighborhood, there is a slightly increased amplification close to the semi-major axis which, if being larger, could actually account for loosing track of the baryonic matter distribution, thus yielding a qualitatively different looking TeVeS convergence κ. As this is not the case, however, the elliptical TeVeS lens can essentially be regarded as a GR lens of almost the same symmetry, but with increased convergence and changed scale lengths. In Figure 3.14, we compare the critical lines in TeVeS to those obtained in GR assuming different elliptical profiles, i.e. choices of x_0. Please note that some of these curves are not represented due to the grid's finite resolution. In accordance with our considerations above, the critical curves calculated in TeVeS do not show any unfamiliar shapes. In fact, one can basically obtain the same results using elliptic density distributions in GR. As the TeVeS convergence κ is calculated by a weighted amplification of κ_{gr}, the critical curves appear at a larger distance from the origin compared to GR. Additionally, due to the effective change of scale lengths, we observe the forms of those curves to be varied to some extent.

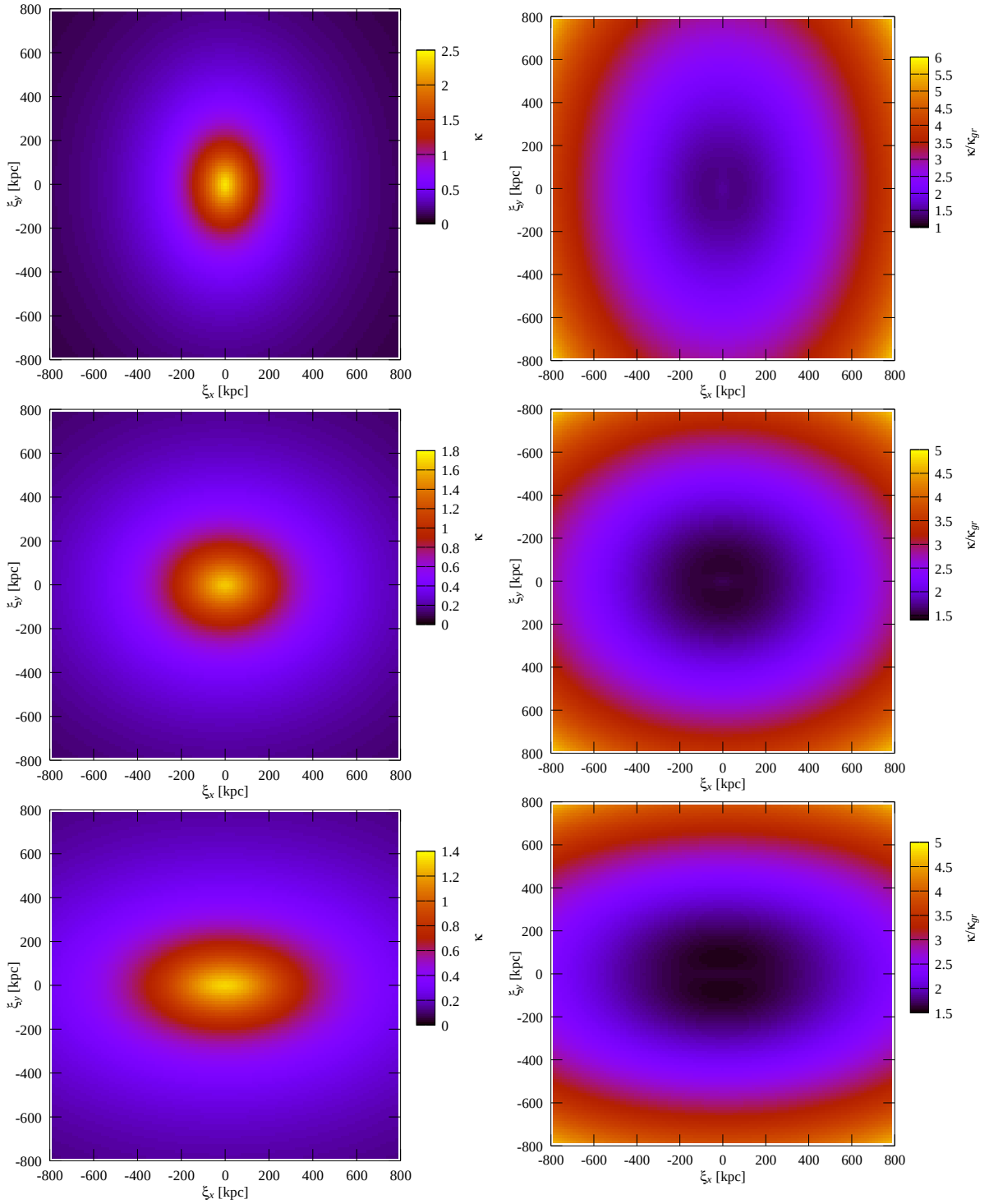

Figure 3.13: Numerically calculated TeVeS convergence κ and the corresponding ratio κ/κ_{gr} for different elliptical profiles of type (3.55): Choosing $y_0 = z_0 = 200kpc$, we present the results for $x_0 = 150$ (top panel), $x_0 = 250kpc$ (middle panel) and $x_0 = 350kpc$ (bottom panel). Compared to GR, the TeVeS convergence κ is amplified such that there are virtually no changes concerning the symmetry properties.

In summary, we find the properties of the elliptic TeVeS lens to resemble those of an elliptic GR lens. Concerning the TeVeS convergence map, there is a strong tracking of the baryonic matter density. Similar to section 3.2.7, we also notice an increase of iteration steps needed for solving equation (1.69) when moving to higher ellipticities.

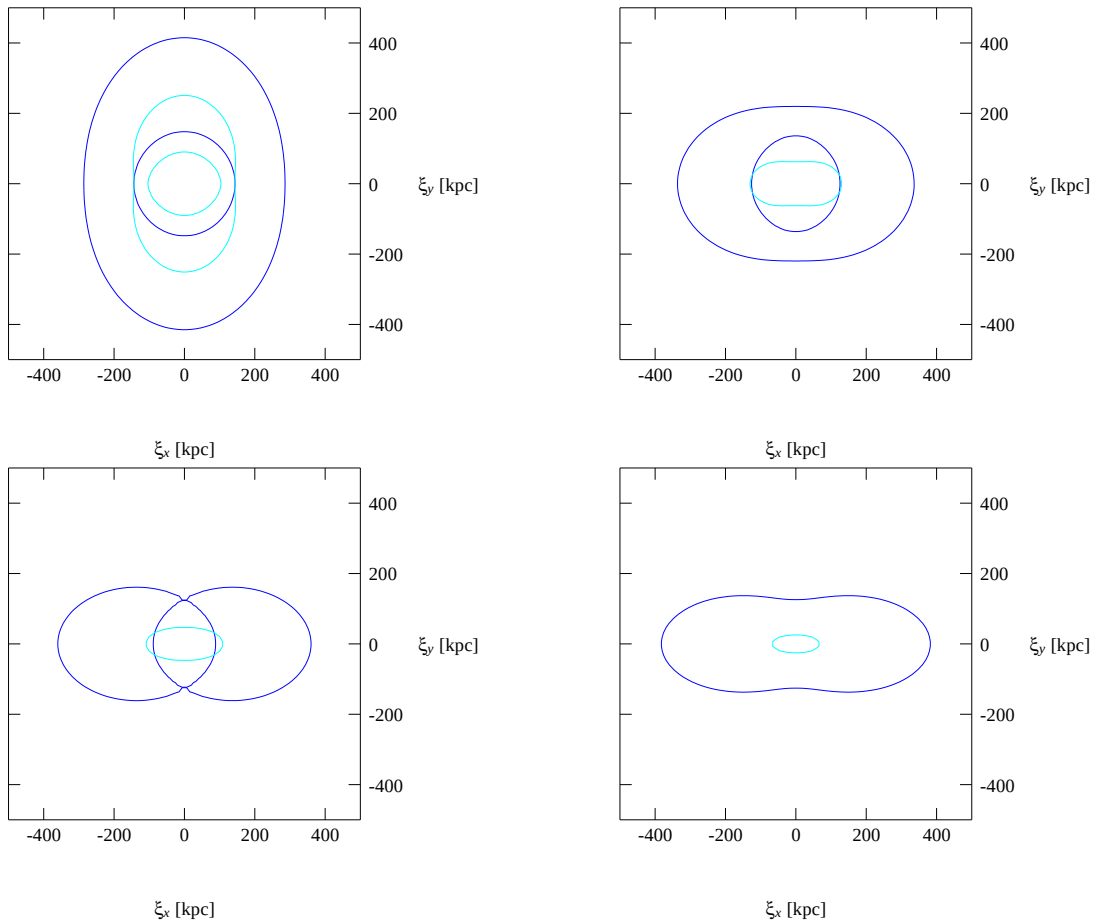

Figure 3.14: Critical curves for both TeVeS (blue) and GR (light blue) assuming different elliptical profiles of type (3.55): Choosing $x_0 = 150kpc$ (top left), $x_0 = 250kpc$ (top right), $x_0 = 300kpc$ (bottom left) and $x_0 = 350kpc$ (bottom right), we find the critical lines to assume various shapes which are familiar from lenses in GR. Please note that some of these curves are not represented due to the grid's finite resolution.

3.2.9 Two-Bullet Systems

As our next task, we want to explore gravitational lensing by multiple objects. For this purpose, let us consider a rather simple case and start with two density distributions, $\tilde{\rho}_1$ and $\tilde{\rho}_2$, following the King profile (3.49). Choosing $r_c = 200kpc$ and $M_1 + M_2 = M = 10^{15} M_\odot$ (M_i denotes the total mass of the object located at $\vec{r}_i$ inside our volume), we shall place our densities at the following positions inside the grid volume ($r = |\vec{r}| = 0$ corresponds to the grid's origin):

$$\vec{r}_1 = \begin{pmatrix} x_2 \\ 0 \\ z_2 \end{pmatrix}, \quad \vec{r}_2 = \begin{pmatrix} -x_2 \\ 0 \\ -z_2 \end{pmatrix}. \tag{3.56}$$

Thus, varying the parameters x_2 and z_2, we are able to control the relative alignment of our objects along the line of sight, i.e. the z-direction, as well as perpendicular to it.

A. Equal Masses

As a first approach, we shall assume the total mass M to be evenly distributed on our two bullet-like objects, i.e. $M_1 = M_2$. Setting x_2 to values of $100kpc$ and $300kpc$, respectively, we calculate the convergence maps and critical lines for different alignments along the line of sight, with the results presented in Figures 3.15 and 3.16. Again, compared to the GR convergence

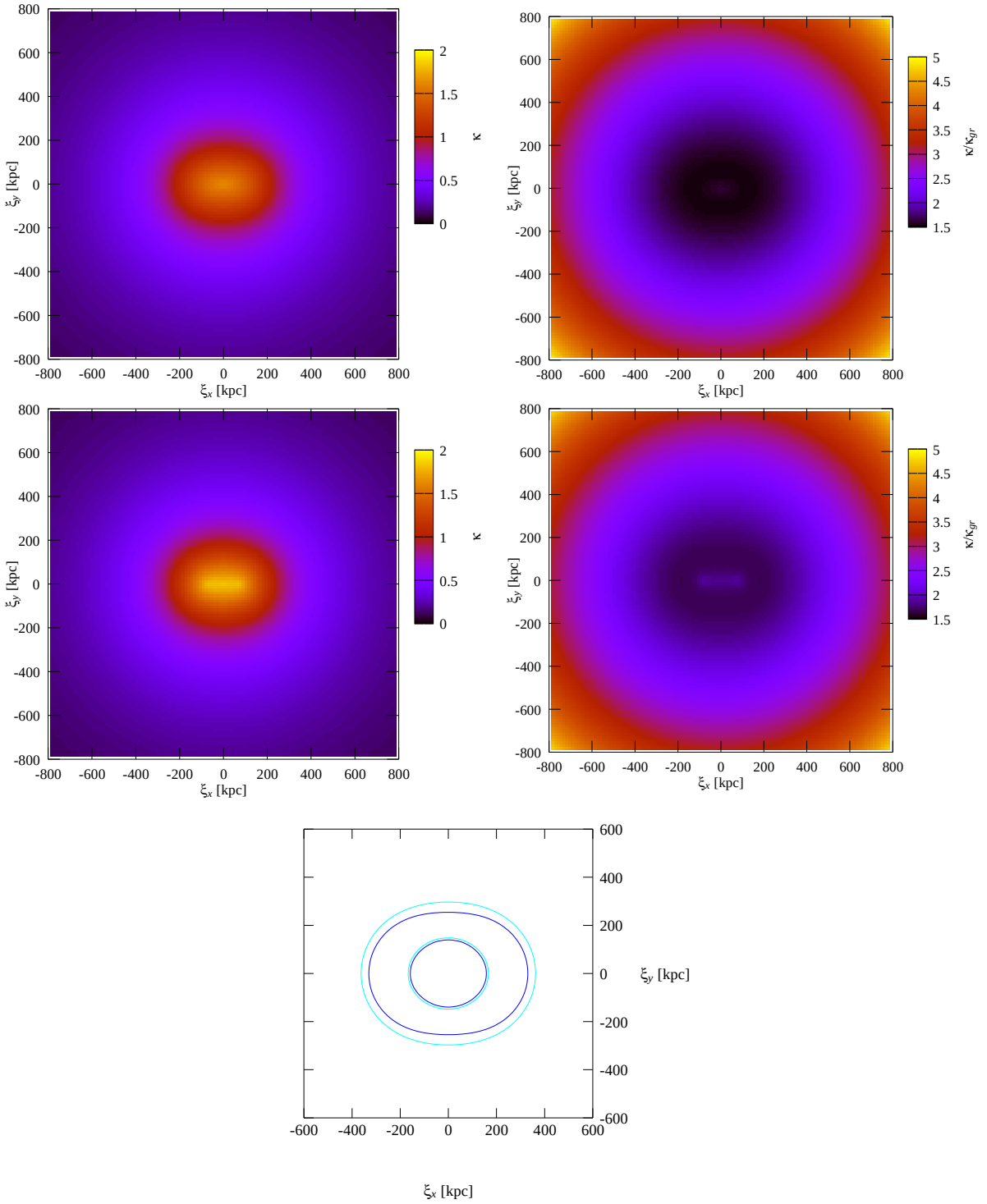

Figure 3.15: Lensing properties of our two-bullet system assuming $x_2 = 100kpc$ and $M_1 = M_2$: We present the numerical results for both the TeVeS convergence κ and the corresponding ratio κ/κ_{gr} setting $z_2 = 0$ (top panel) and $z_2 = 400kpc$ (middle panel), respectively. Bottom panel: The critical lines in TeVeS plotted for $z_2 = 0$ (blue) and $z_2 = 400kpc$ (light blue).

map, we notice κ to be amplified such that the symmetry properties of the surface density, i.e. the projection of the particular density field $\tilde{\rho}$, are more or less conserved, which is similar to the result found in the last section. Having a look at the central region, we additionally observe that κ is increased between the object's positions, which is actually expected since the Newtonian gradient $\vec{\nabla}\Phi_N$ becomes small there. Altogether, as the TeVeS convergence map strongly tracks

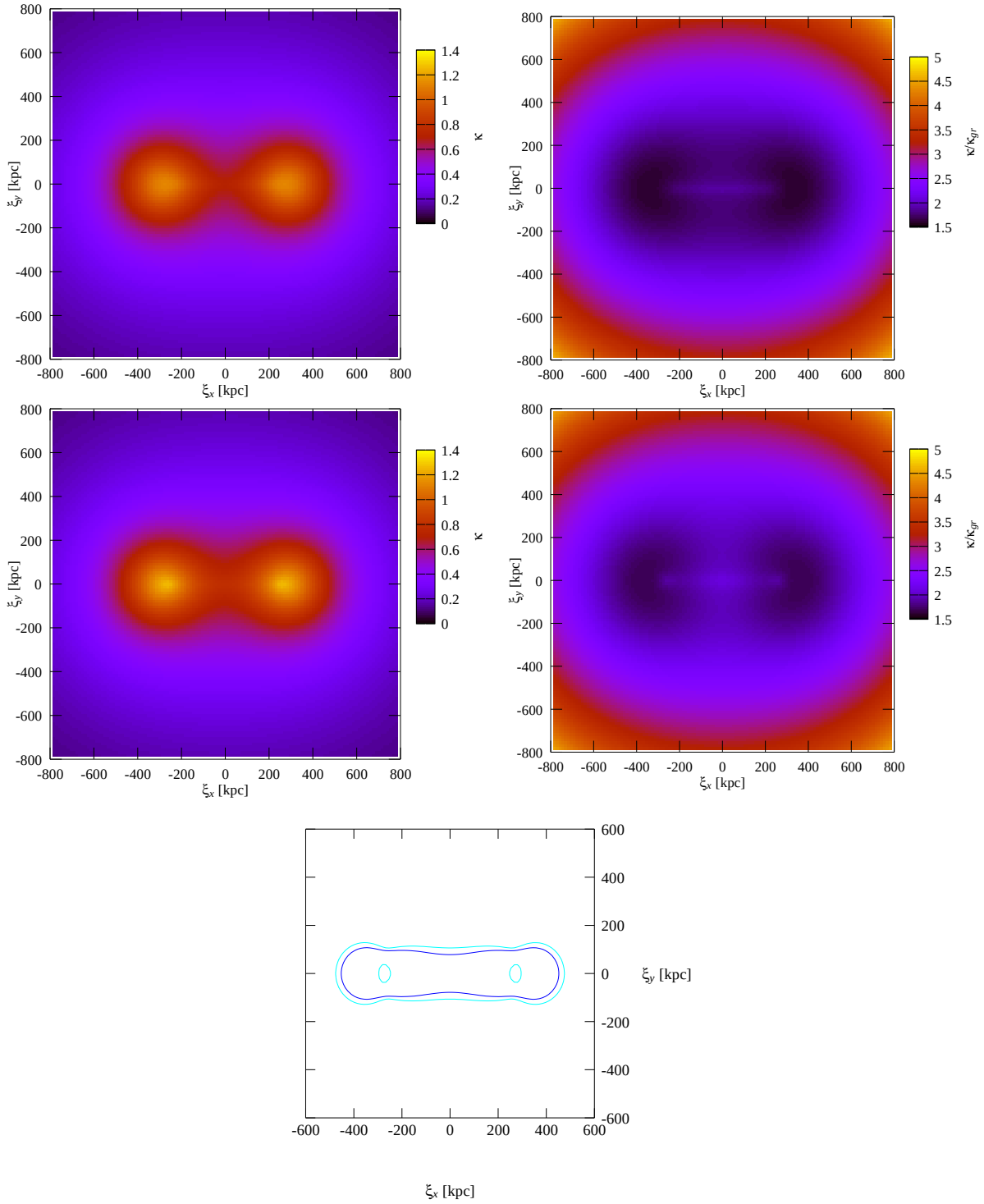

Figure 3.16: Lensing properties of our two-bullet system assuming $x_2 = 300kpc$ and $M_1 = M_2$: We present the numerical results for both the TeVeS convergence κ and the corresponding ratio κ/κ_{gr} setting $z_2 = 0$ (top panel) and $z_2 = 400kpc$ (middle panel), respectively. Bottom panel: The critical lines in TeVeS plotted for $z_2 = 0$ (blue) and $z_2 = 400kpc$ (light blue).

the baryonic matter distribution, we do not encounter any surprising TeVeS effects considering our two-bullet system. Concerning different alignments along the z-axis, however, there is an interesting effect: If we increase z_2 from 0 to $400kpc$ keeping the other parameters fixed, we discover a growth of the convergence around the center while there is basically no change of κ in the outer parts. Consequently, the corresponding critical lines are spatially driven outwards,

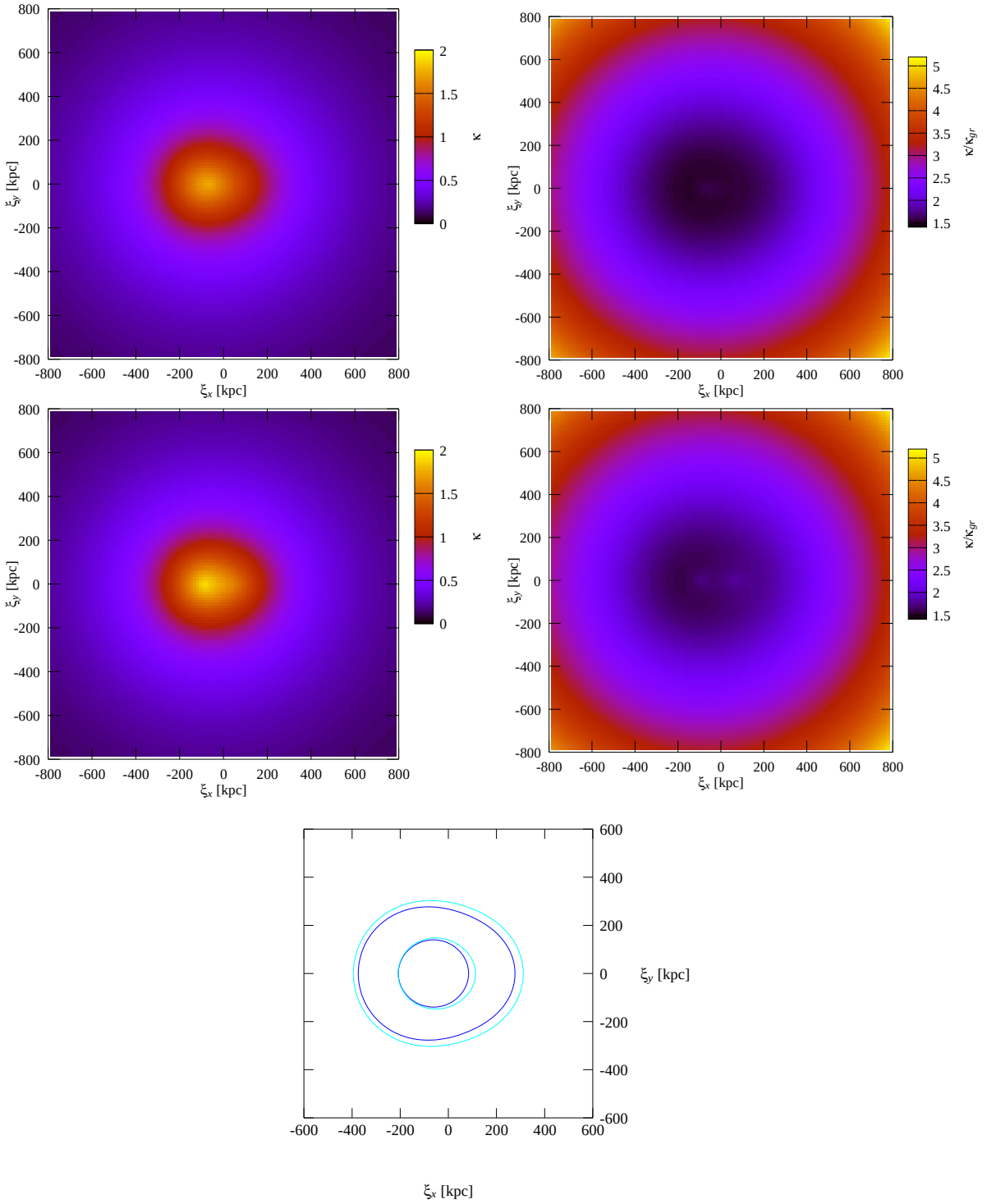

Figure 3.17: Lensing properties of our two-bullet system assuming $x_2 = 100kpc$ and $3M_1 = M_2$: We present the numerical results for both the TeVeS convergence κ and the corresponding ratio κ/κ_{gr} setting $z_2 = 0$ (top panel) and $z_2 = 400kpc$ (middle panel), respectively. Bottom panel: The critical lines in TeVeS plotted for $z_2 = 0$ (blue) and $z_2 = 400kpc$ (light blue).

which is shown in the bottom panel of Figure 3.15 and 3.16, respectively. Please also note that, due to the nonspherical symmetry of our problem, the shape of those curves is slightly changed when varying z_2. Recalling our analysis from section 3.2.7, it therefore appears that the relative alignment of two density profiles along the z-direction has the same qualitative effect as stretching those density profiles separately along this direction. Referring to the quantitative

results, we furthermore find the relative deviations of the critical curves' position in both cases to be of the same order. Considered to be true, the above possibly hints on a general limitation of the influence on the lensing properties due to the matter's distribution along the line of sight. At the moment, however, this is merely a wild guess and there is clearly more investigation needed.

B. Different Masses

Analog to section 3.2.9 A, we can perform the same numerical simulation choosing $3M_1 = M_2$. Assuming $x_2 = 100kpc$, both the calculated convergence map and the critical lines are presented in Figure 3.17 for $z_2 = 0$ and $z_2 = 400kpc$, respectively. As can be seen from the ratio κ/κ_{gr}, the convergence is more strongly amplified in the $\xi_x > 0$ regime, i.e. the region of smaller mass density, compared to the results based on the choice $M_1 = M_2$. Accordingly, the corresponding critical lines are drawn further outwards in that region. Comparing the results for $z_2 = 0$ and $z_2 = 400kpc$, we notice this effect to grow stronger when the lens's extent along the line of sight is enlarged. As the MONDian influence increases for smaller values of the Newtonian gradient's modulus $|\vec{\nabla}\Phi_N|$, however, the observed behavior is in accordance with our expectations. Choosing other bullet alignments or mass weightings, we basically obtain the same results.

C. Numerical Problems

Concerning the numerical simulations of our two-bullet systems, there occur some problems related to the iterative solver for the scalar field: Assuming the previously declared choice of parameters, the solver's convergence properties significantly impair for $150kpc \lesssim z_2 \lesssim 250kpc$. While the amount of necessary iteration steps heavily increases at the boundaries of this interval, we observe a complete failure of the method approaching $z_2 \sim 200kpc$, i.e. our solver does not converge anymore showing the oscillatory behavior discussed in section 3.2.4 C. Since a variation of the relaxation parameter ω does not improve the situation, we remark that (3.42) is not appropriate in every case. Although the reasons for this failure are very likely to be of purely numerical origin, we emphasize that these problems may also hint on the occurrence of exceptional solutions of the scalar field.

3.2.10 Three-Bullet Systems

A. Setup and Results

For further investigation, we may actually think of adding a third component to the bullet system introduced within the last section. Again, we shall make use of the King profile (3.49) to model these objects, but now setting $r_c = 150kpc$. Assuming $M_{1,3} := M_1 = M_3$ and $2M_{1,3} + M_2 = M = 10^{15}M_\odot$ (again, M_i denotes the total mass of the object located at $\vec{r}_i$ inside our volume), we shall place the three density distributions at the following positions inside the grid volume ($r = |\vec{r}| = 0$ corresponds to the grid's origin):

$$\vec{r}_1 = \begin{pmatrix} x_3 \\ y_3 \\ 0 \end{pmatrix}, \quad \vec{r}_2 = \begin{pmatrix} 0 \\ -y_3 \\ 0 \end{pmatrix}, \quad \vec{r}_3 = \begin{pmatrix} -x_3 \\ y_3 \\ 0 \end{pmatrix}, \tag{3.57}$$

with x_3 being fixed to a value of $250kpc$. Concerning the bullets' relative masses, we shall examine the cases $M_{1,3} = M_2$ and $2M_{1,3} = M_2$: Specifying to one particular choice of the mass relation, we feed our solver with the corresponding matter densities for $y_3 = 0$ and $y_3 = 150kpc$, respectively. From Figures 3.18 and 3.19, we observe the numerical results to essentially show the same TeVeS effects as found in the previous sections. Since there is nothing new to learn from these systems, we may actually end our discussion at this point.

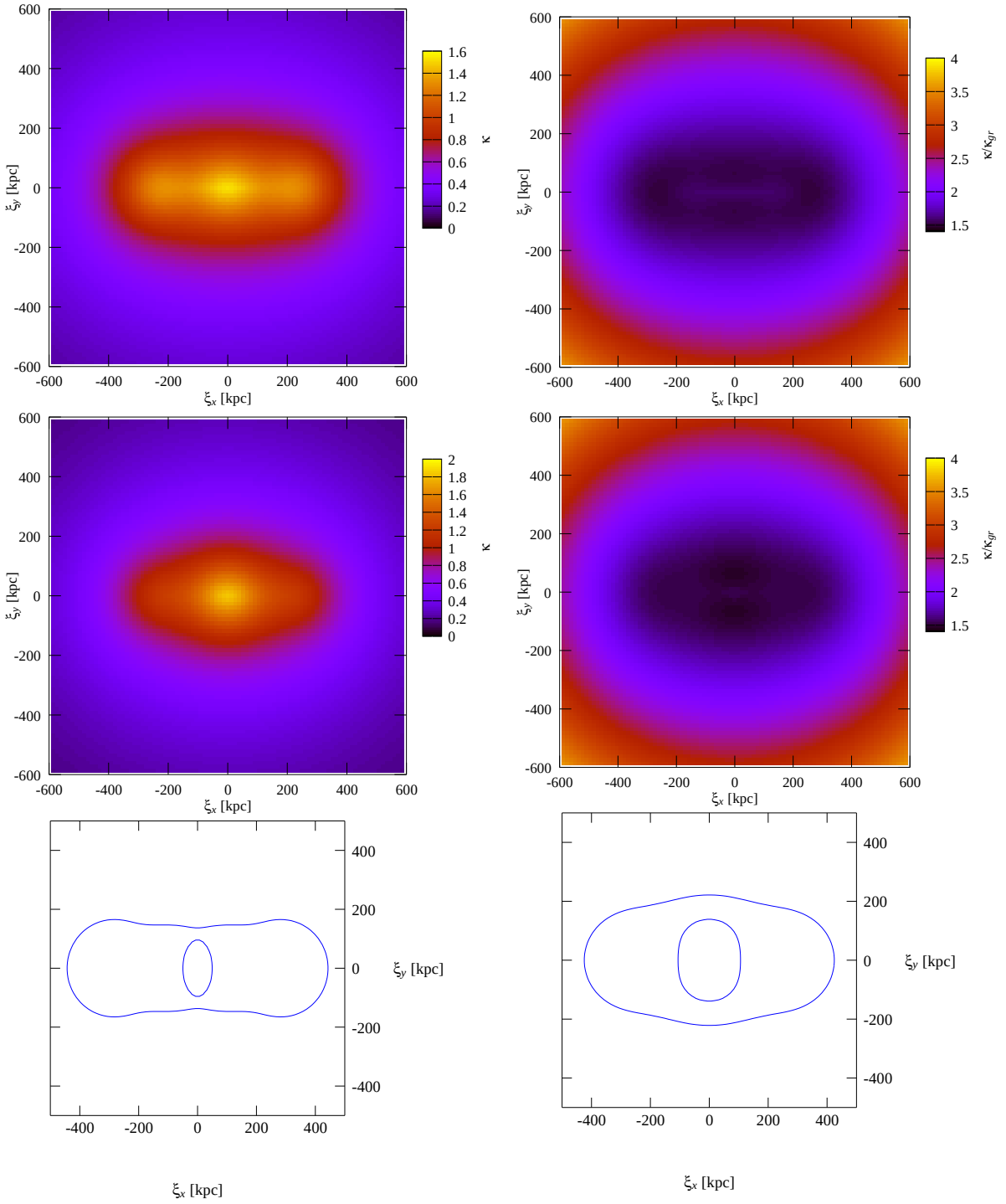

Figure 3.18: Lensing properties of our three-bullet system assuming $y_3 = 0$: We present the numerical results for both the TeVeS convergence κ and the corresponding ratio κ/κ_{gr} setting $M_{1,3} = M_2$ (top panel) and $2M_{1,3} = M_2$ (middle panel), respectively. Bottom panel: The critical lines in TeVeS plotted for $M_{1,3} = M_2$ (left) and $2M_{1,3} = M_2$ (right).

B. Numerical Problems

Similar to section 3.2.9 C, we also encounter convergence problems when considering the above three-bullet systems. For example, choosing the parameters of the last section, our iterative solver already fails if we introduce a small relative shift of the positions $\vec{r}_i$ along the z-direction. Compared to the two-bullet systems, the situation seems even worse as this problem does not

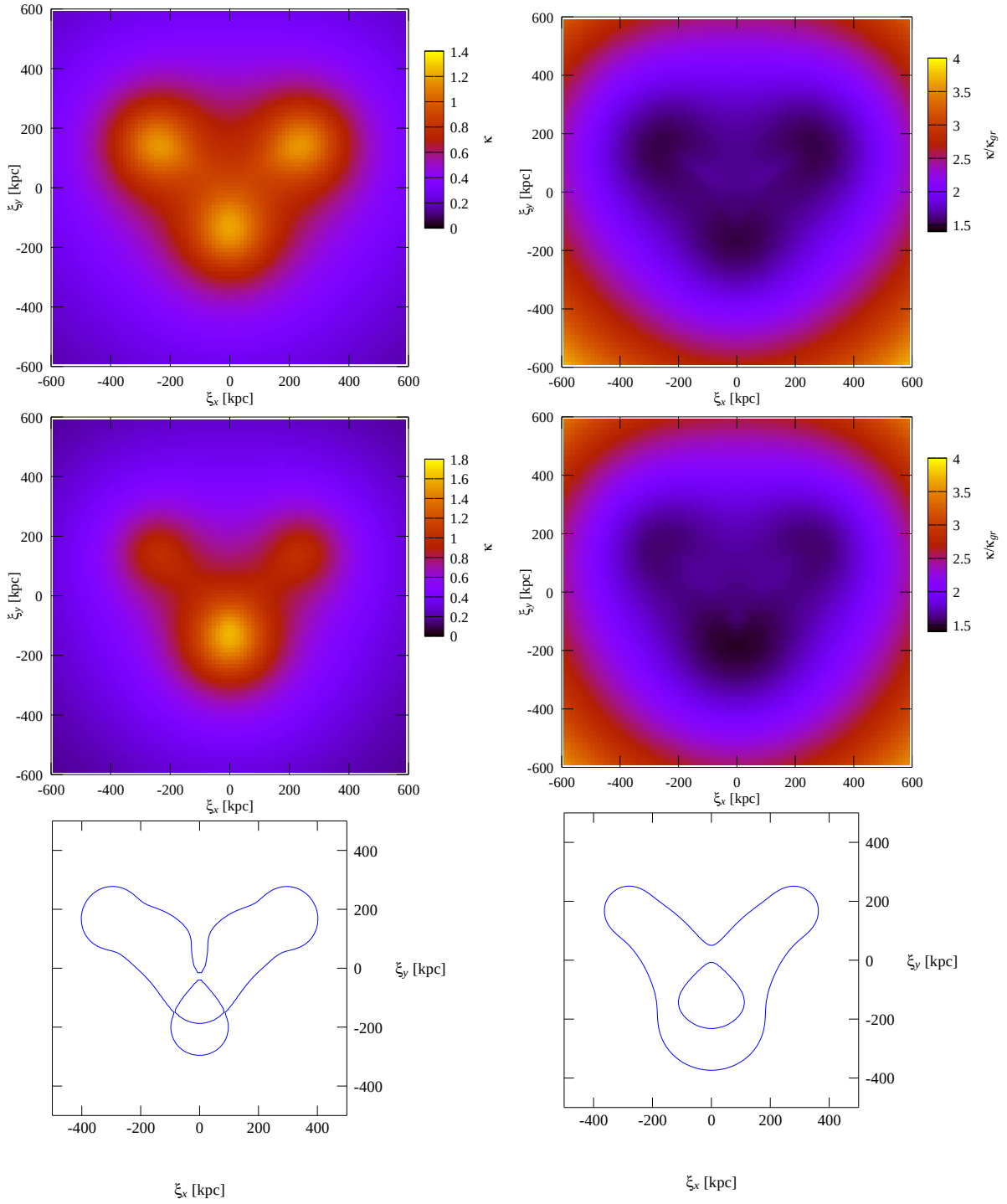

Figure 3.19: Lensing properties of our three-bullet system assuming $y_3 = 150kpc$: We present the numerical results for both the TeVeS convergence κ and the corresponding ratio κ/κ_{gr} setting $M_{1,3} = M_2$ (top panel) and $2M_{1,3} = M_2$ (middle panel), respectively. Bottom panel: The critical lines in TeVeS plotted for $M_{1,3} = M_2$ (left) and $2M_{1,3} = M_2$ (right).

appear to be limited to a certain range and is found to be almost independent of the particular choice of the parameter y_3 used in (3.57). Concerning a further discussion of this issue, we shall follow the argumentation presented in section 3.2.9 C.

Surprisingly, however, there are no such problems at all when moving to more complicated matter density distributions like, for instance, the toy model of the bullet cluster we will present

Component	Position (x, y, z) $[kpc]$	Plasma mass M_X $(10^{12} M_\odot)$	Stellar mass M_* $(10^{12} M_\odot)$	M_{total} $(10^{12} M_\odot)$
Main cluster	$(-350, -50, z_1)$	5.5	0.54	6.0
Main cluster plasma	$(-140, 50, z_2)$	6.6	0.23	6.8
Subcluster	$(350, -50, z_3)$	2.7	0.58	3.3
Subcluster plasma	$(200, -10, z_4)$	5.8	0.12	5.9

Table 3.2: Component masses and positions for our toy model of the cluster merger 1E0657 − 558: Concerning the particular masses of our toy model components, we shall make use of those derived by Clowe et al.. The plasma mass is reconstructed from a multicomponent three-dimensional cluster model fit to the Chandra X-ray image. Assuming a mass-to-light ratio of $M/L_I = 2$, stellar masses are calculated from the I-band luminosity of all galaxies equal in brightness or fainter than the component's brightest cluster galaxies (BCG). Please note that all masses are averaged over an aperture of $100kpc$ radius around the given position. For each component, the corresponding position perpendicular to the line of sight is approximately determined from the left image of Figure 3.20

in the next section. Obviously, a more detailed analysis of both the iteration and (3.42) is needed in order to get a better understanding of our method's intrinsic properties, which might enable us to resolve the found difficulties and should be subject to future work.

3.2.11 Toy Model of the Bullet Cluster

Only recently, the cluster merger 1E0657 − 558, which we will refer to as the bullet cluster, has been announced as a direct empirical proof of the existence of dark matter (Clowe et al., 2006; Bradač et al., 2006). As can be seen in Figure 3.20, the weak lensing reconstruction of the convergence map, being independent of the particular law of gravity, shows peaks that are clearly detached from the dominant baryonic components, i.e. the plasma clouds. Therefore, like any other theory of gravity that does not presume the existence of dark matter, TeVeS must be able to explain the observed lensing effects based upon the baryonic matter distribution alone. Using

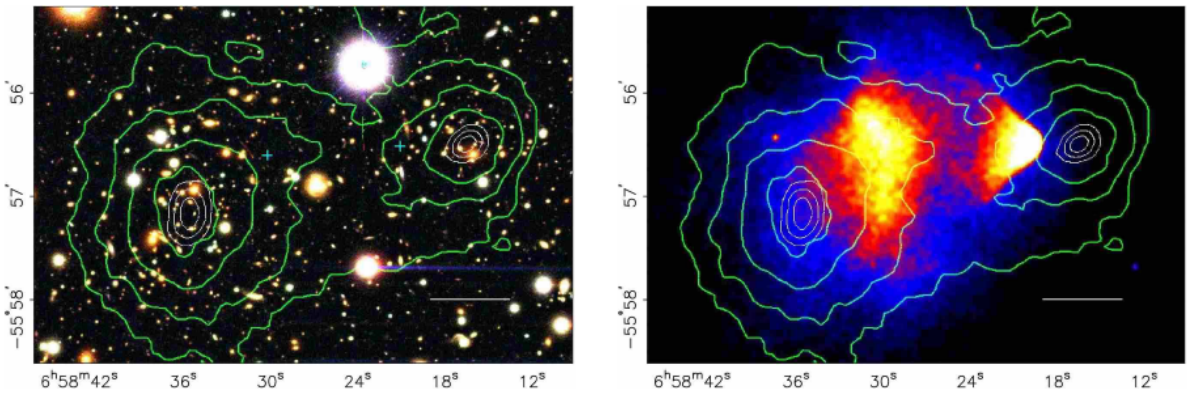

Figure 3.20: Shown on the left side is a color image from the Magellan images of the merging cluster 1E0657 − 558, with the white bar indicating $200kpc$ at the distance of the cluster. On the right there is a $500ks$ Chandra image of the cluster. Shown in green contours on both sides is the weak lensing κ reconstruction with the outer contour level at $\kappa = 0.16$ and increasing in steps of 0.07. The white contours show the errors on the positions of the κ peaks and correspond to 68.3%, 95.5% and 99.7% confidence levels. The blue +s show the location of the centers of the plasma clouds (Clowe et al., 2006).

an analytical model fit to the weak lensing reconstruction of κ illustrated in Figure 3.20, Angus et al. (2007) have derived the corresponding baryonic matter density in TeVeS concluding that it is not possible to model the bullet cluster's convergence map without assuming an additional invisible mass component located in the central parts of the two clusters. Concerning their work,

Parameter set	z_1	z_2	z_3	z_4
A	0	0	0	0
B	0	300	0	-300
C	0	500	0	-500
D	300	100	-300	-100

Table 3.3: Parameter sets used within the toy model of the cluster merger 1E0657 − 558: In our simulations, the above sets are used in order to specify the component's alignment along the line of sight, i.e. the z-direction.

however, there are some discontinuities we briefly want to mention here: First of all, there is made use of a convergence map being too weak to account for the observed strong lensing arcs within this system (Bradač et al., 2006). Secondly, the same convergence map appears to be incompatible with the values of plasma masses independently estimated from Chandra observations, which, as remarked by the authors, may be due to the smoothing scale of the weak lensing reconstruction. For these reasons, such a map may be regarded as an inappropriate starting point for an analysis of the bullet cluster within the framework of TeVeS gravity.

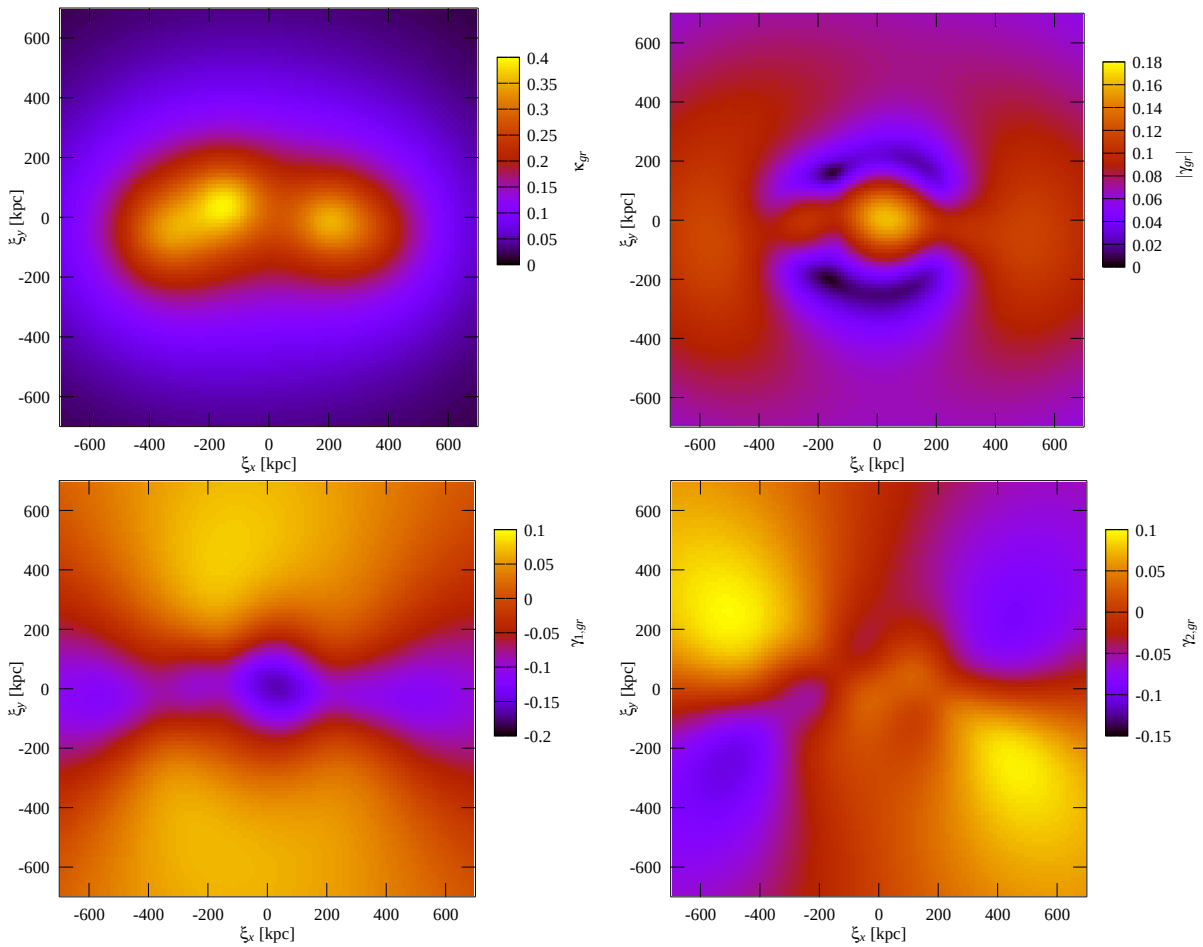

Figure 3.21: GR convergence and GR shear maps for our toy model of the bullet cluster: Assuming the framework of GR, we present the numerical maps for the convergence κ_{gr} (upper left), the modulus of the shear $|\gamma_{gr}|$ (upper right) as well as for the shear components $\gamma_{1,gr}$ (lower left) and $\gamma_{2,gr}$ (lower right). Please note that the results are independent of the particularly used parameter set controlling the component's alignment along the z-axis.

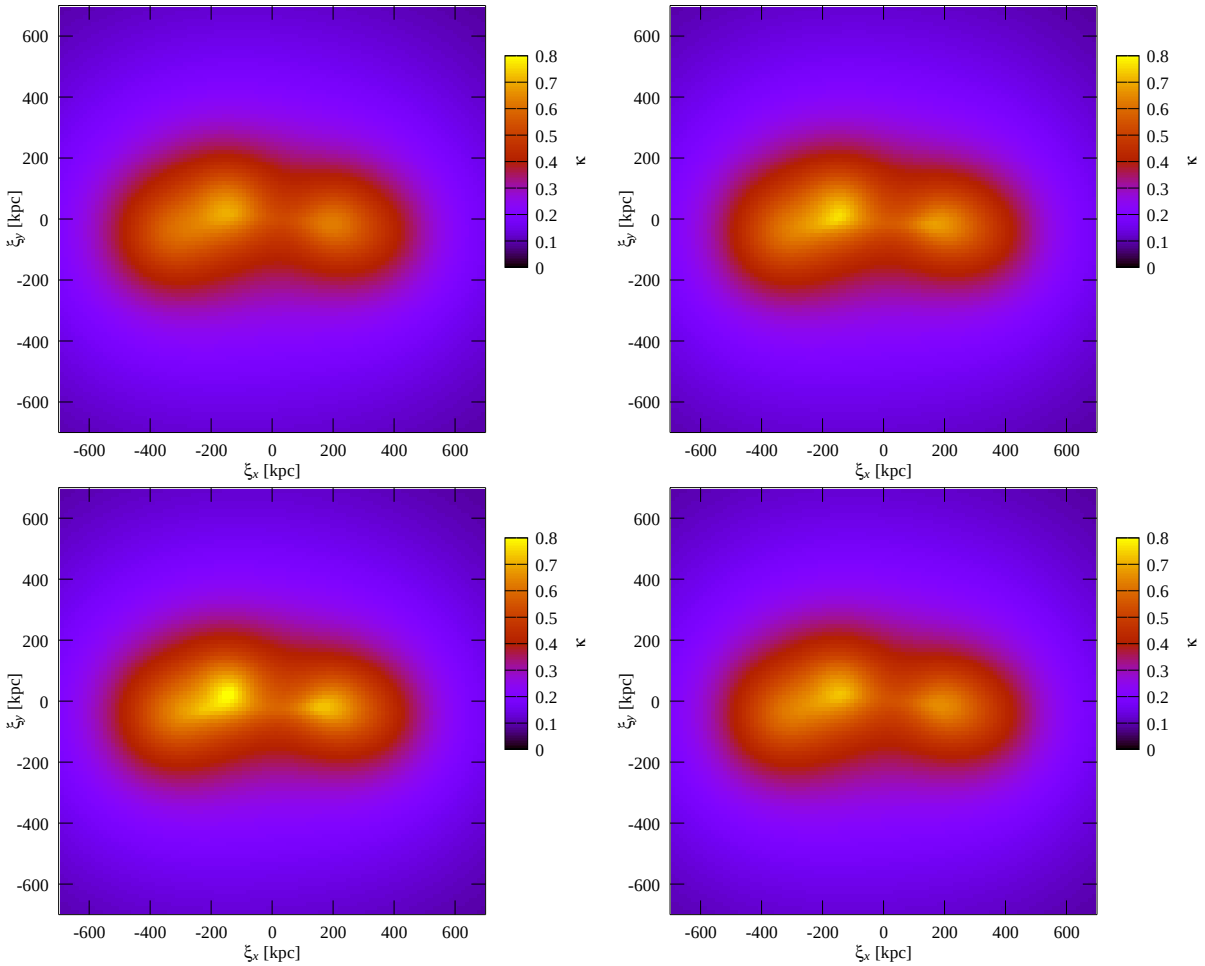

Figure 3.22: TeVeS convergence maps for our toy model of the bullet cluster: Assuming the framework of TeVeS, we present the numerically obtained convergence κ for the parameter sets A (upper left), B (upper right), C (lower left) and D (lower right).

In order to avoid such discontinuities, we shall follow a completely different approach for our investigations. As a first try, we will create a rather simple toy model of the bullet cluster's baryonic matter density that allows to be treated with our numerical method. From Figure 3.20, we can identify four objects: The main cluster, a slightly smaller subcluster and two plasma clouds appearing in between. For the three-dimensional matter density, we shall model these four components using the analytical King profile (3.49) introduced in section 3.2.7, choosing core radii r_c of $200kpc$ and $150kpc$ for the clusters and the plasma clouds, respectively. Furthermore, concerning the choice of masses, we will make use of the values from Clowe et al. which are derived independently of gravitational lensing: According to authors, the plasma mass is reconstructed from a multicomponent three-dimensional cluster model fit to the Chandra X-ray image while, assuming a mass-to-light ratio of $M/L_I = 2$, the stellar mass is calculated from the I-band luminosity of all galaxies equal in brightness or fainter than the component's brightest cluster galaxies (BCG). Together with the positions of the four components being roughly estimated from Figure 3.20, the corresponding mass values are presented in Table 3.2. Please note that all masses are averaged over an aperture of $100kpc$ radius around the given position. Thus, considering the King models of our components, the parameter $\tilde{\rho}_0$ in (3.49) has to be chosen such that the total mass inside a sphere of radius $R = 100kpc$ is in accordance with the values shown in Table 3.2. For the calculation of the lensing maps, we furthermore set the redshift of the bullet cluster, i.e. the lens, to $z_{lens} = 0.296$ (Clowe et al., 2006) and assume a source redshift of $z_{source} = 1$.

Since the position of the particular constituents can only be constrained perpendicular to the line of sight, we actually have great freedom in selecting their alignment along the z-direction. Returning to Table 3.2, we find the z-coordinates of all components to be parameterized by the constants z_i which, of course, have to be specified before applying our numerical tool to the simple baryonic density model of the bullet cluster. From sections 3.2.7 and 3.2.9, we know that the matter's extent along the line of sight may have a significant influence on the resulting TeVeS lensing properties. Thus, our examination should definitely include a variation of the z_i. Table 3.3 shows the sets of parameters we shall use in the upcoming analysis. Let us briefly discuss the meaning of these choices: Clearly, the parameter set A implies that all components are located in the same plane perpendicular to the line of sight. The choices B and C account for the plasma clouds to be displaced in opposite directions along the z-axis, which may be a reasonable assumption considering today's observation of the bullet cluster to be an after-collision snapshot. Finally, the parameter set D fairly describes the situation that the axis connecting the cluster centers is inclined towards the z-direction.

With the remaining parameters specified, we are now ready to apply our numerical method to the toy model. Although we do not encounter any serious problems related to the solver of the scalar field, we notice that the amount of needed iteration steps reaches values of up to 150. Figures 3.22 and 3.23 illustrate both the resulting TeVeS convergence map κ and the

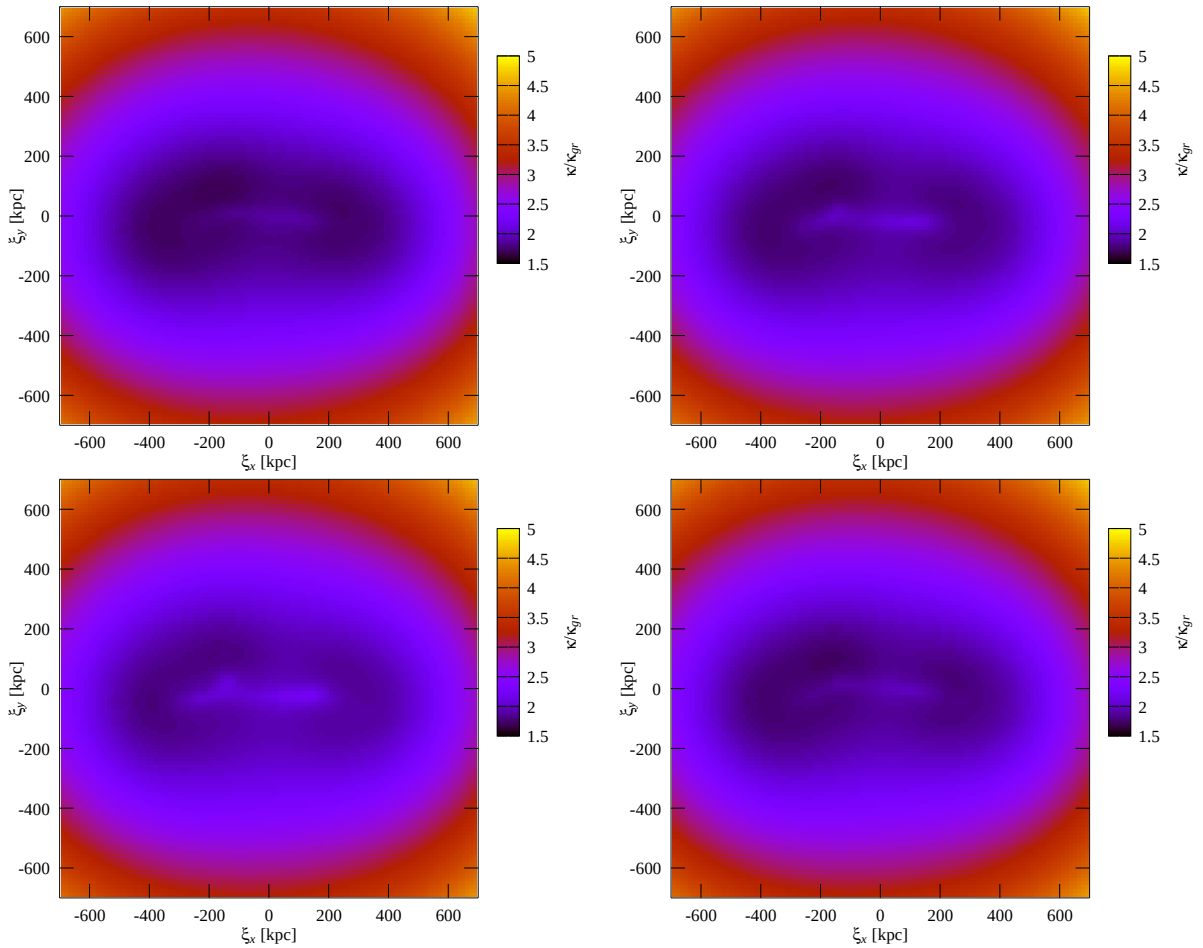

Figure 3.23: TeVeS convergence ratio κ/κ_{gr} for our toy model of the bullet cluster: Assuming the framework of TeVeS, we present the numerically obtained convergence ratio κ/κ_{gr} for the parameter sets A (upper left), B (upper right), C (lower left) and D (lower right).

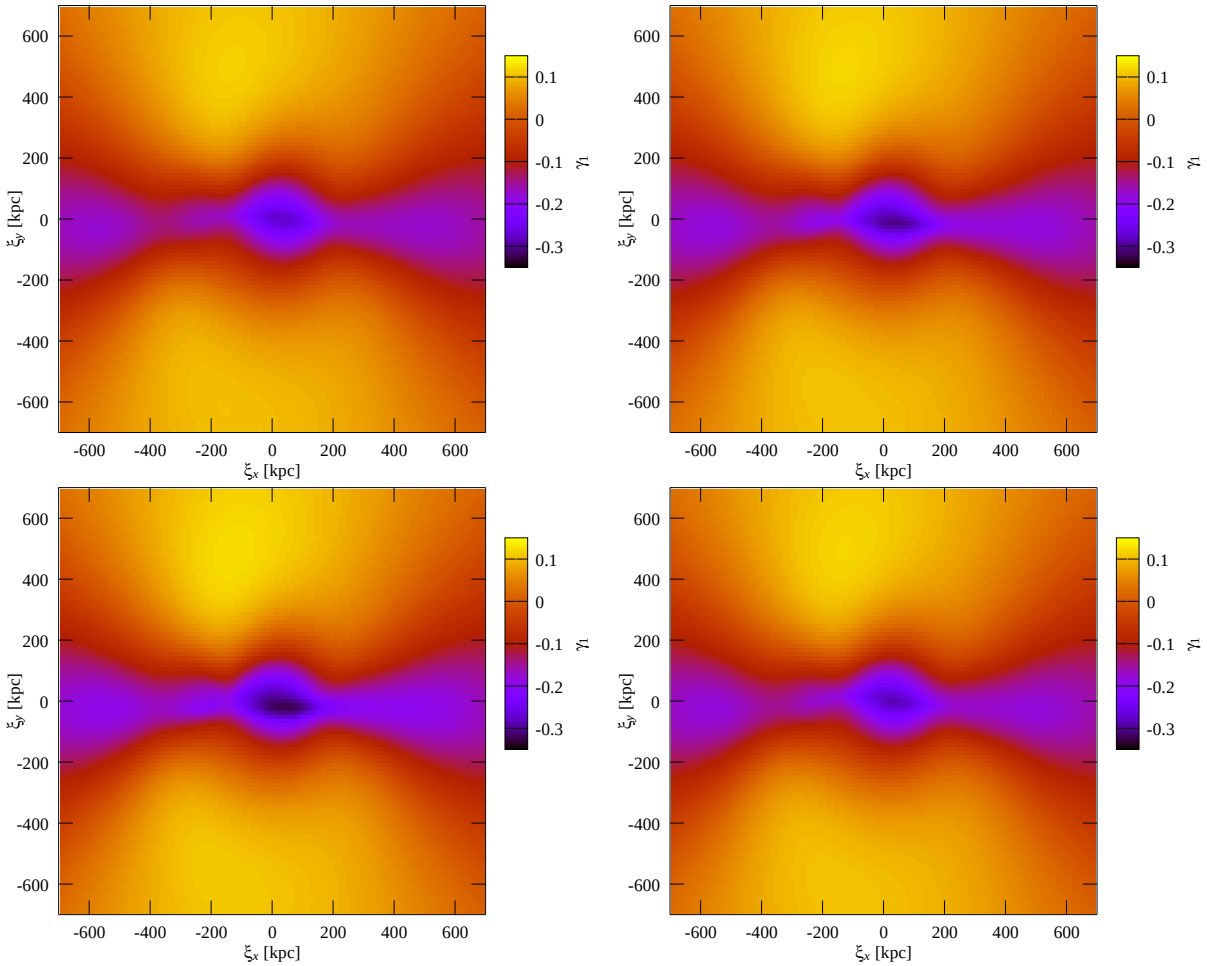

Figure 3.24: TeVeS maps of the shear component γ_1 for our toy model of the bullet cluster: Assuming the framework of TeVeS, we present the numerically obtained shear component γ_1 for the parameter sets A (upper left), B (upper right), C (lower left) and D (lower right).

corresponding ratio κ/κ_{gr} for the parameter sets listed in Table 3.3. As we can see from Figure 3.23, due to the different alignments along the z-axis, there are slight deviations of the particular amplification in the central part, which is similar to previously considered lens models. Although the dominant baryonic peaks are relatively suppressed, which is because of the growing MONDian effects when moving to the surroundings of those peaks, we observe the TeVeS convergence to show a strong tracking of the corresponding surface mass density which is equivalent to the GR convergence plotted in Figure 3.21. Thus, we find TeVeS to need more mass centered at the cluster positions to provide an acceptable explanation of the observations. Additionally, we present maps of the TeVeS shear components γ_1 and γ_2 which are shown in Figure 3.24 and 3.25, respectively. Again, compared to the corresponding GR maps from Figure 3.21, there is basically no qualitative difference. Comparing the TeVeS lensing maps for different parameters z_i, however, we point out that there are noticeable *quantitative* deviations which should become important for estimations of the actual missing mass.

Altogether, our numerical simulations clearly confirm the basic result of Angus et al.. In order to obtain a convergence map similar to the one shown in Figure 3.20, we need an additional mass component in both cluster centers since the TeVeS convergence map appears to strongly track the projected baryonic matter distribution. If this additional mass is due to hot neutrinos or other dark particles has yet to be decided.

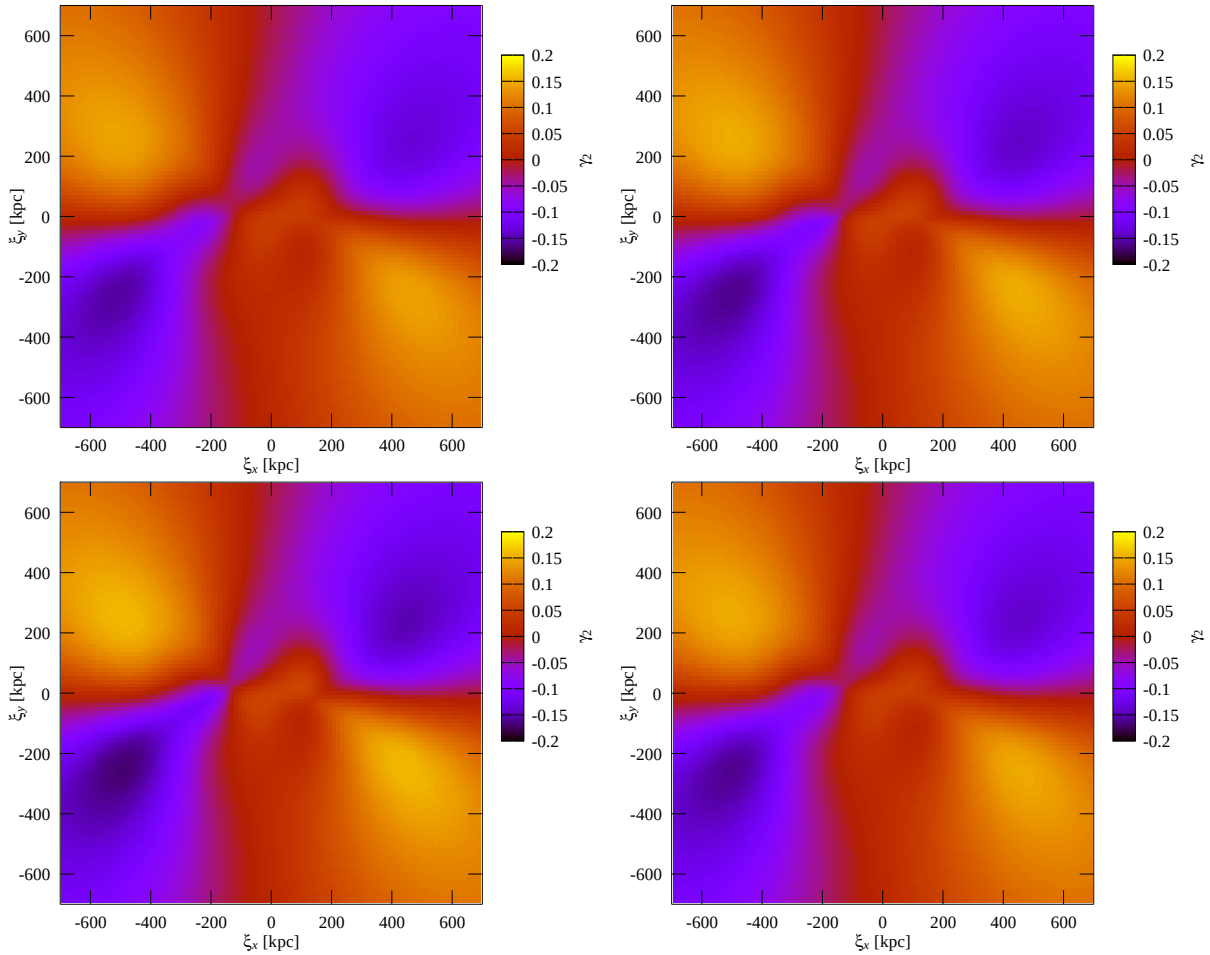

Figure 3.25: TeVeS maps of the shear component γ_2 for our toy model of the bullet cluster: Assuming the framework of TeVeS, we present the numerically obtained shear component γ_2 for the parameter sets A (upper left), B (upper right), C (lower left) and D (lower right).

Finally, some brief remarks: Concerning our toy model, one might actually regard our choice as being too simple. Although we agree on that and plan to apply the same examination to far more realistic three-dimensional matter distributions, it should be very unlikely to obtain results being qualitatively different from the above as our toy model recovers the basic features of the bullet cluster and we have encountered the TeVeS convergence map to strongly track matter density $\tilde{\rho}$ throughout our analysis. This tracking behavior actually appears to be intrinsic to TeVeS. Similarly, we may consider our limitation to a single choice of the free function. As we have pointed out in section 3.1.2, we expect small variations of the free function to have small effects on the physical results, thus preserving the qualitative lensing properties of a particular density distribution. Although we cannot provide any analytical proof, we are quite confident to empirically show this by incorporating other choices of the free function into our numerical method in the near future.

4 Conclusions

In this work, we have analyzed the effects of gravitational lensing within the framework of Tensor-Vector-Scalar gravity (TeVeS), especially focusing on the strong lensing regime.

Beginning with an analytical investigation of TeVeS lenses, we chose a smooth variant of the free function that was originally proposed by Zhao et al. (2006) and derived closed expressions for the deflection angles of both a point and a Hernquist lens, which allowed for a first insight in the corresponding lensing properties. Moving to lens systems with peculiar velocities $v \neq 0$, we were able to determine the resulting deflection angle in closed form, which was found to coincide with the expression known from GR

Concerning the numerical analysis, we introduced a parameterization of the free function by means of a Laurent expansion. This actually enabled us to systematically study the influence of a varying free function on the physical results, i.e. the particular lensing properties, assuming spherically symmetric systems. Within this examination, we concluded that variations of the coupling constant k leads to negligibly small effects as long as $k \lesssim 10^{-2}$. Furthermore, making use of the Laurent coefficients, we found classes of free functions producing nearly the same lensing maps.

Considering nonspherical lenses, we were unable to perform the same examination due to the occurrence of a highly nonlinear partial differential equation. From a physical point of view, however, we expect the free function's influence to be similar to that in a spherical system. Picking a single choice of the free function, we additionally succeeded in building a fast Fourier-based solver for scalar potential which could be used to calculate TeVeS lensing maps within certain limitations.

Applying our new method to a set of different, mostly nonspherical lens types, we noticed a strong dependence of the lensing properties on the lens's extent along the line of sight, which corresponds to a complete break-down of the thin lens approximation in TeVeS. Besides that, every simulated TeVeS convergence map showed a strong tracking of the dominant baryonic mass components, other effects, being capable of counteracting this trend, turned out to be very small.

Finally, we created a toy model of bullet cluster's baryonic matter density, again using our numerical method to obtain the corresponding lensing maps. The simulation's outcome clearly confirmed the results from Angus et al. (2007) as it is not possible to explain the observed weak lensing map without assuming an additional mass component in both cluster centers.

Thinking of future projects, it might be interesting to directly compare GR lenses embedded in a dark matter halo to their TeVeS counterparts. As lensing properties of both models have to coincide far away from the lens, there could be measurable differences in the strong lensing regime. Furthermore, we may ask ourselves if the additional TeVeS freedom along the line of sight generally allows to mimic the GR dark matter lens. Concerning our working solver, we have already planned to incorporate different choices of free functions and apply it to more realistic density profiles including snapshots of a three-dimensional cluster merger simulation. Finally, as previously mentioned, it may be useful to perform a more detailed analysis of our solving

scheme in order to resolve the problems we have encountered in some numerical calculations.

5 Acknowledgments

To cut this section short: Many, many, many thanks to all members of the ITA cosmology group. I really enjoyed my last year here, especially the time drinking coffee, playing table tennis, soccer, etc.

Special thanks go to Cosimo and Matthias. Without your useful comments most of this work would probably not have been possible. I really had fun working with you!!!
Thanks also to Emanuel for fixing my computer and all the other hardware that crashes once a while. Thanks to Peter M. for providing Linux and LaTex assistance. And thanks to Francesco for being there at night.

Bibliography

Angus, G. W., Shan, H. Y., Zhao, H. S., & Famaey, B. 2007, ApJ, 654, L13

Bartelmann, M. & Schneider, P. 2001, Phys. Rep., 340, 291

Bekenstein, J. D. 2004, Phys. Rev. D, 70, 083509

Brada, R. & Milgrom, M. 1995, MNRAS, 276, 453

Brada, R. & Milgrom, M. 1999, ApJ, 519, 590

Bradač, M., Clowe, D., Gonzalez, A. H., et al. 2006, ApJ, 652, 937

Broeils, A. H. 1992, A&A, 256, 19

Ciotti, L., Londrillo, P., & Nipoti, C. 2006, ApJ, 640, 741

Clowe, D., Bradač, M., Gonzalez, A. H., et al. 2006, ApJ, 648, L109

Famaey, B. & Binney, J. 2005, MNRAS, 363, 603

Hernquist, L. 1990, ApJ, 356, 359

King, I. 1962, AJ, 67, 471

Milgrom, M. 1983a, ApJ, 270, 371

Milgrom, M. 1983b, ApJ, 270, 384

Milgrom, M. 1983c, ApJ, 270, 365

Mortlock, D. J. & Turner, E. L. 2001, MNRAS, 327, 557

Narayan, R. & Bartelmann, M. 1999, in Formation of Structure in the Universe, ed. A. Dekel & J. P. Ostriker, 360–+

Sanders, R. H. 1999, ApJ, 512, L23

Sanders, R. H. & Verheijen, M. A. W. 1998, ApJ, 503, 97

Tully, R. B. & Fisher, J. R. 1977, A&A, 54, 661

Wucknitz, O. & Sperhake, U. 2004, Phys. Rev. D, 69, 063001

Zhao, H. 2006, ArXiv Astrophysics e-prints, astro-ph/0610056

Zhao, H., Bacon, D. J., Taylor, A. N., & Horne, K. 2006, MNRAS, 368, 171

Zhao, H. S. & Famaey, B. 2006, ApJ, 638, L9